UNIVERSITY OF CALIFORNIA SAN DIEGO

Spectral Decomposition in Large Scale Nuclear Computations:
Broken Symmetries of Chromium and Astrophysical PF-Shell Weak Transitions

A dissertation submitted in partial satisfaction of the
requirements for the degree
Doctor of Philosophy

in

Physics

by

Raul A. Herrera

Committee in charge:

Professor George Fuller, Chair
Professor Daniel Arovas
Professor Alison Coil
Professor Michael Holst
Professor Calvin Johnson
Professor William McEneaney

2020

The dissertation of Raul A. Herrera is approved, and it is
acceptable in quality and form for publication on microfilm
and electronically:

_____

_____

_____

_____

_____

Chair

University of California San Diego

2020

DEDICATION

To my abuelitos, Juanita and Sixto, and Maria and Pablo,

        from humble beginnings in Mexico with hard work and intrepidity

        in the USA they eventually get a grandson with a Ph.D. in

        computational quantum many body physics, whatever that means.

And to my parents, Carmen and Raul,

        for being intelligent, musical and creative.

        I'd like to think I take after them.

EPIGRAPH

Open your eyes,

Let it begin with me.

Brand new day,

Fresh new way to live,

The mornin' is callin',

Walk with me into the sun.

Everything's Coming Our Way,

—Carlos Santana

TABLE OF CONTENTS

times and the darkest of times when I had nothing but the need to get away for a bit from teaching, research, and dissertation writing. Besides all the frivolous good times, my friends and peers also helped me develop intellectually and become an active and productive servant of the larger student community.

In this miscellaneous paragraph, I first thank the reliable UCSD staff members, especially Sharmila Poddar as graduate coordinator, who was a great source of information, compassion and encouragement in times of trouble. I thank Catherine McConney for consistently giving me teaching jobs to help pay the bills, and Brad Hansen for keeping all the stuff working in our teaching labs. Thanks to counselor Hercilia Corona for listening and for sound advice, even when I didn't follow it. Thanks to my roommates and neighbors throughout the university years for tolerating any occasional, and usually unintended, nuisance. Thanks to my friends at the Sacramento State chapter of the Society of Physics Students from 2007-2010, Dr. D (DeGraffenreid) our mentor, and our cheerful administrative supporter Heidi Yamazaki. Thanks to my friends at San Joaquin Delta Community College, especially in the Alpha Gamma Sigma Honors Society going back to 2002, including my cousin Teresa Mercado-Gans former president and constant inspiration!

In continuance of a tradition, and not begrudgingly at all, I mention some of my colleagues from Cal State LA. I definitely would not have gotten seriously into research without the following peers, since my plan at that time was to get a Master's degree and teach community college. Some of them literally told me that I was too smart to stop there, and I tried really hard to believe them. Therefore, special appreciation in alphabetical order to good friends and motivators Clare Abreu, Jay Chiang, Nicholas Derimow, David Guzman, Velveth Klee, Min Lu, Jhen Lumbres, Madeline Monroy, and Stephanie Pham. But also thanks to all the Physics Activity Club (PAC) members and associates from 2010 to 2013. Continuing on, many fun and creative times were had with a short lived group known as Rock The Arts! Thanks to Marie Bruno in the physics department office. And thanks to Professors Aniol, Bernal, Jishi, Rodriguez, and Terebey, who all taught me

something useful about being a physicist.

Finally, I give awesome thanks and praise to all my family, including my sisters Claudia and Jaz, all my cousins, my aunts and uncles on both the Herrera and Galaviz side, for all their support through the struggle of college and grad school. My little sister Jazmin was my fellow traveler through much of college including my M.S. program, and I'm glad we had each other to reinforce the drive for pursuing higher education and achievement. I wish her well as she pursues her Master's degree. During grad school the two family members I relied on most were my mother Carmen Rosa Galaviz and my cousin Javier Galaviz. My mom stayed with me at times, and made me plenty of sopa to eat. She has always been very supportive and my biggest fan. My primo Javier was usually available, just a couple hours away in Los Angeles, whenever I needed a distraction. He knows the best venues to check out free live music, and is an ace at cutting through LA traffic. I thank my older cousin Steve Herrera, always a mentor and kindred spirit in art and philosophy. Whenever I headed back home to Stockton from this far away land of San Diego, I made sure to find him to jam on guitar and talk about life. I thank my grandmother Maria Herrera for buying me my first computer as a kid, and supporting me as I started community college. My grandmother Juana Galaviz was always a source of moral support and encouragement, and instilled in me appreciation for her home country Mexico and its culture. My father Raul Sr. passed in 2012 just as I was starting the Ph.D. program, but in his last few years we shared a love of playing guitar, including boleros, latin rock, and soul. Music was a helpful distraction from time to time and a powerful way to get the creative juices flowing, so special thanks to the god of music. Lastly, singular appreciation goes to the my uncle Paul Herrera, who inspired me to learn more about science and computers. If they make Apple Watches in heaven, he has one for sure.

Again, I acknowledge my doctoral advisers for assisting in the following work:

Chapter 2, in full, is a reprint of the material as it appears in Physical Review C, 2017. Herrera Raul; Johnson, Calvin. I was the primary investigator and author of this paper.

Chapter 3 is coauthored with Johnson, Calvin W. and Fuller, George M. I was the primary investigator and author of this chapter.

2007	A. A. in Computer & Information Science, San Joaquin Delta College
2010	B. A. in Physics, CSU Sacramento
2012	M. S. in Physics, CSU Los Angeles
2020	Ph. D. in Physics, UC San Diego

PUBLICATIONS

Tatiana A. Sergan, Vassili Sergan, Raul Herrera, Lu Lu , Phillip J. Bos, and Ekaterina V. Sergan, "In situ control of surface molecular order in liquid crystals using a localised polymer network and its application to electro-optical devices", Liquid Crystals, 40 (1), 72 (2012)

Raúl A. Herrera and Calvin W. Johnson, "Quasidynamical symmetries in the backbending of chromium isotopes", Phys. Rev. C. 95, 024303 (2017)

Vassili Sergan, Tatiana A. Sergan, Phillip J. Bos, Lu Lu, Raul Herrera, and Ekaterina V. Sergan, "Control of liquid crystal alignment using surface-localized low-density polymer network and its application to electro- optical devices", Journal of Molecular Liquids 267, 131 (2018)

ABSTRACT OF THE DISSERTATION

Spectral Decomposition in Large Scale Nuclear Computations:
Broken Symmetries of Chromium and Astrophysical PF-Shell Weak Transitions

by

Raul A. Herrera

Doctor of Philosophy in Physics

University of California San Diego, 2020

Professor George Fuller, Chair

Using a modified version of the Lanczos matrix diagonalization algorithm for spectral decompositions, properties beyond basic nuclear structure can be computed. In this dissertation, this method is applied to solutions of the nuclear Hamiltonian under symmetry group operators and weak nuclear force transition operators. In Chapter 2, I decompose state vectors for chromium isotopes decomposed into the basis of Casimir operators of symmetry groups relevant to nuclei. While these symmetries are broken under the nuclear interaction, the decompositions tend to hold their patterns for certain progressions of states identified to be crossing rotational bands in the energy spectrum, where the spectra are related to the phenomena of backbending. These

patterns are known as quasi-dynamical symmetries. In Chapter 3, I compute weak nuclear force transition strength functions, specifically Gamow-Teller transitions for certain pf-shell isotopes relevant to massive stellar collapse and nucleosynthesis. I examine these transitions in terms of the Brink-Axel hypothesis, which states that transition strength distributions from excited states are identical to the transition strength distribution from the ground state. I develop a method for computing weak transition rates in stellar environments based on a localized Brink-Axel statement. This allows for the access of highly excited states, which have heretofore been prohibitive, and therefore improved thermal weak rates of heavy nuclei at temperatures occurring in stellar cores near collapse. As such, the methods developed in this dissertation are a contribution to progress on this topic.

Chapter 1

Introduction and Theoretical Background

The properties of nuclei are important in many applications, whether nuclear energy and medicine, or understanding astrophysical phenomena. Fundamental to such applications is an understanding of nuclear structure and dynamics. Therefore, this chapter begins with an outline of the basic quantum many-body problem of nuclear physics. Later, I introduce the mathematical concept of symmetry groups, which was applied in the work of Chapter 2, a previously published collaboration on the properties of rotational bands in chromium isotopes, which are associated with another phenomenon in the nuclear energy spectrum called backbending. Then, I discuss weak nuclear force transitions of selected heavy nuclei around mass number $A = 55 - 57$, in preparation for the work in Chapter 3. The weak nuclear force is responsible for beta decay and related processes such as neutrino production, which provides important context to the gravitational collapse of massive stars. The appropriate use of an approximation known as the Brink-Axel hypothesis is analyzed of these iron peak nuclei, but will not be discussed until Chapter 3. At then end of this chapter, I discuss the relevance of the Lanczos algorithm [1], and prescribe the different versions of it used to compute the nuclear Hamiltonian eigenvectors, and spectral decompositions.

1.1 Nuclear Structure

In this work, nuclei are treated as non-relativistic collection of neutrons and protons at low energy (order of keV and MeV) relative to medium and high energy scales of meson exchange, or QCD and quarks, respectively. This will suffice for most applications, including stars at temperatures in the billions of kelvin. These temperatures correspond to energies of MeV, where nuclei may dissociate but are not necessarily relativistic. Because the proton and neutron have similar mass and interaction with the nuclear forces to a good approximation, one can treat them as a single type of particle known as the nucleon, exhibiting a two state symmetry, the two dimensional representation of SU(2). Therefore I use the isospin coordinate, short for *isotopic* or *isobaric* spin, which is analogous mathematically to electron spin [2]. The quantum number for the total isospin of a state is T, where a nucleon has $T = 1/2$. The proton and neutron are assigned spin up and down states, respectively, and given the isospin projections $T_z = 1/2$ and $T_z = -1/2$. For a single nucleus, I use Z for the number of protons, and N for the number of neutrons, such that $T_z = (Z - N)/2$. Lastly, since the same SU(2) algebra holds for isospin, then for a single nucleon the isospin operators τ_i can be represented by the same Pauli matrices, such that in matrix form $\tau_i = \sigma_i$ for $i = x, y, z$.

1.1.1 Many-Body Hamiltonian and Wave Function

In quantum many-body physics, the Hamiltonian is generalized so that one sums over the kinetic energies, T_i, of all the particles, the interparticle interactions, V_{ij}, and any external potentials, U_i, giving:

$$H = \sum_i (T_i + U_i) + \frac{1}{2} \sum_{i \neq j} V_{ij}. \tag{1.1}$$

The many-body Hamiltonian acts on many-body wave functions, Ψ_n, that depend on the spatial coordinates for all $A = N + Z$ particles, $\vec{r}_1, \vec{r}_2, \ldots \vec{r}_A$, where $\vec{r}_i = (x_i, y_i, z_i)$. Ψ_n also depends

on the spin angular momentum $\vec{s}_i = (s_i^x, s_i^y, s_i^z)$ and isospin coordinates $\vec{\tau}_i = (\tau_i^x, \tau_i^y, \tau_i^z)$ of every particle.

General solutions to the many-body eigenvalue problem $H_n \Psi_n = E_n \Psi_n$ are written as linear combinations as:

$$\Psi_n = \sum_{k=1}^{Dim(H)} c_k \Psi_k'(\vec{r}_1, \vec{s}_1, \vec{\tau}_1; \vec{r}_2, \vec{s}_2, \vec{\tau}_2; \ldots, \vec{r}_A, \vec{s}_A, \vec{\tau}_A), \qquad (1.2)$$

where the Ψ_k' are members of a Hilbert space comprising the many-body basis. The c_k are the amplitude coefficients of each basis state. The sum is up to the dimension of the vector space, $Dim(H)$, which could be in principal be infinite. In this work, the total angular momentum of a nucleus is the sum of the individual total angular momentums of each nucleon, $\vec{J} = \sum_i \vec{j}_i = \vec{L} + \vec{S}$, where $\vec{L} = \sum_i \vec{l}_i$ is the total *orbital* angular momentum, and $\vec{S} = \sum_i \vec{s}_i$ is the total *spin* angular momentum, of the constituent nucleons. Sometimes in nuclear physics literature the total angular momentum of the nucleus is labeled by I instead of J.

Ideally, one works with complete basis sets, $\{\Psi_1', \Psi_2', \ldots, \Psi_{Dim(H)}'\}$, meaning sets that span the solution space appropriate to the Hamiltonian. Often these basis sets of functions are constructed from solutions to a simpler problem that has previously been solved, especially if the new problem has similar properties or results form a small perturbation to the old one. An example would be a independent particle model of a mean field of simple harmonic oscillator type. Note: Generally, the term *eigenstate*, *state vector*, and *wave function* may be used interchangeably.

1.1.2 Nuclear Shell Model

In atoms, the quantum states of electron were found to exhibit shell structure, which gives rise to the Periodic Table of Elements and highly stable atoms with filled shells like the noble gases. Similarly, nuclei exhibit shell structure first posited by Nobel Prize winner Maria Goeppert Mayer [3], where filled shells correspond to stable atomic nuclei according to certain *magic*

3
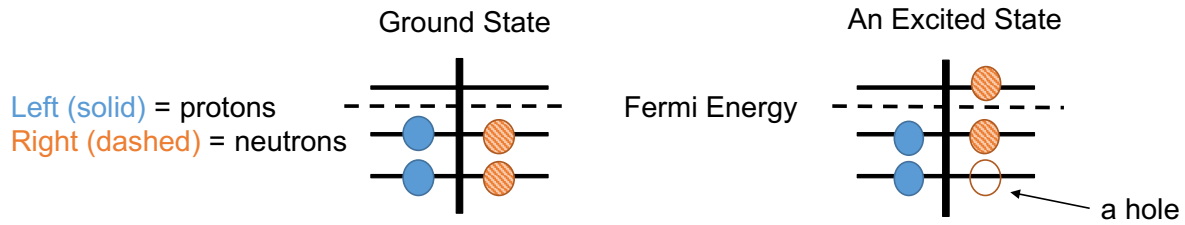
Figure 1.1: Protons and neutrons in the independent particle model

numbers of nucleons. Understanding isospin and shell structure are the first steps in organizing solutions to the nuclear many-body problem, and in this section I develop the nuclear shell model further. Before describing the basis of solutions mathematically, it is useful to provide a mental picture. These shells all represent different energy levels, which are solutions for a single particle in a mean field created by the collective action of all the nucleons. This assumes the *Independent Particle Model*, where none of the particles interact with each other but simply fill up a series of shells that are labeled by specific energy and other quantum numbers. The total energy of the nucleus is therefore the sum of all the individual energies of the protons and neutrons. If one fills up single particle states starting from the bottom upward, one gets the lowest energy state (or states), known as the ground states. But if one allows some of the particles into higher energy shells, one gets *excited states*.

In the simplest case the proton-neutron mass difference, as well as, the Coulomb repulsion of protons is ignored, so the energy levels and states are identical, as in figure 1.1. They are identical fermions, so a proton may not inhabit the same state as another proton, but it may share a state with a neutron. The shells are labeled nl_J by the radial quantum number, n, which by my convention goes as $1, 2, 3, \ldots$, and the orbital angular momentum values $l = 0, 1, 2, 3, \ldots$ that single nucleons would have in the shell, which are given the spectroscopic labels $s, p, d, f, \ldots$, respectively. Hence a major shell labeled 1p means that it has radial quantum number n=1, which is related to the number of nodes in the wave function, and orbital quantum number $l = 1$, and $1p_{3/2}$ is a sub-shell with states of $J = 3/2$. Now the shells with lower n and l are energetically

4

favored and fill up first with nucleons to get the lowest energy state, or *ground state*, though other forces may affect this ordering. But *excited states* of nucleons, where some particles are excited to higher energy shells, will have higher total energies and leave behind holes in the lower energy shells. A nucleus with a ground state comprising of a completely filled shell will be especially stable as the energy gaps between shells make removing a nucleon energetically disfavored. When the total number of protons, or separately the total number of neutrons, corresponds to this filled shell situation, one has a magic number [4] as shown in figure 1.2, where the nucleus has a larger binding energy pointing to stability against decay.

This was mainly used as a tool to understand nuclear structure better, but to get accurate magic numbers and other properties of nuclei, there a few more complications. The usual starting point in the theoretical spectroscopy of nuclei assumes that individual nucleons interact only through a mean field created by the collective action of all the nucleons. The mean field potential takes various forms depending on convenience or desired accuracy, such as the harmonic oscillator or square well. Also, the nuclear Hamiltonian has a strong interaction between the spin and orbital coordinates of the nucleons [5]. The spin-orbit potential takes the form $U_{S-O}(\vec{r}_i)\vec{l}_i \cdot \vec{s}_i$ and becomes part of the mean field, preserving the Independent Particle Model but with newly shifted energies of the orbitals, s, p, d, f,..., along with splitting for different values of total angular momentum, where $|L-S| \leq J \leq L+S$.

In figure 1.2, the major shell groupings (1s or just s, 1p or just p, 2s1d or sd, 1p1f or pf) include these effects. Also in the figure, the pf-shell, having higher energy then the sd-shell, is partially filled and therefore is known as the *valence* shell. Below that all shells (sd, p, and s) are completely filled and represent a frozen core of the very stable nucleus ^{40}Ca, where this corresponds to magic numbers of 20 protons and 20 neutrons.

Again due to the large energy gaps between major shells, it is possible in applications to ignore the frozen core and only deal with interactions of nucleons within finite valence shell subspaces. An interaction among these nucleons is know as a *residual interaction*. Now
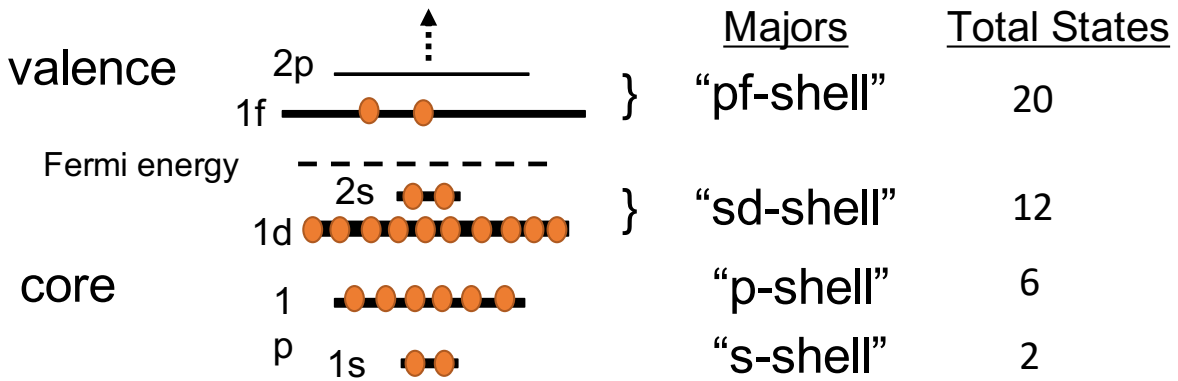
Figure 1.2: Nuclear shell groupings and magic numbers structure, where energy increases vertically. Example "pf" is a major shell made up of two subshells; namely the 1f and 2p. Note: for simplicity only one type of nucleon is shown e.g. protons.

the generic many-body Hamiltonian described in equation 1.1 becomes more specific and is represented in terms of matrix elements. That is, in this work I use so-called *phenomenological interactions*, where the energy contribution of the frozen core is known and the interaction matrix elements for the valence space is provided for diagonalization. The matrix elements of these phenomenological interactions are derived by fitting the eigenvalues of nuclides in the model space to so-called *realistic interactions*, such as the Bonn potential [6], with parameters that were fitted to experimental data, including nucleon scattering data.

1.1.3 Many Body Basis

When restricting to a valence space, as described in the previous section, one gets an interaction in a basis of single particle states, where they are often the same for protons and neutrons. In the M-scheme including isospin, these single particle states, would be labeled $|nljMTTz\rangle$, where for protons and neutrons $T = 1/2$ and $Tz = \pm\frac{1}{2}$. However, since nucleons are fermions, these states are either occupied or not, and a convenient and natural representation to put into a computer is the occupation space representation. For fermions this gives a binary representation in terms of 0 or 1, whereas for bosons one could have occupancies greater than

1. Thus, I assign to each single particle basis state an index in a vector of zeroes and ones corresponding to whether that state is occupied. Finally, I use a complete vector space of states with one for each possible combination of zeros and ones, where in a single basis state the number of ones must add up to the total mass number, $A = N + Z$.

Generally, one can write an occupation space state as a tensor product of possible states for particles to occupy:

$$|n_1\rangle \otimes |n_2\rangle \otimes \cdots \otimes |n_k\rangle = |n_1 n_2 \ldots n_k\rangle, \tag{1.3}$$

where the n_k are the occupancies of the k-th states, the label, i, represents a specific basis state having a unique k-tuple of n_k, and $|0\rangle = |000....0\rangle$ is a vacuum state representing no particles occupying any state. For example in occupation space, if one had three fermions in six different states, then one could have the following:

$$|010101\rangle$$

$$|100101\rangle \tag{1.4}$$

$$|100011\rangle$$

One might wish to work in a space where N, Z, or $A = N + Z$ vary, that is, the total number of neutrons, protons, or nucleons respectively. The direct sum of all possible basis states with different numbers of identical particles is called a Fock space, but generally in nuclear physics, including this work, one keeps the total number of nucleons fixed. This is represented by a *sector* of Fock space with only A nucleons in the occupancy space representation. Also, this fixed basis can be organized as a tensor product of proton states with neutron states, $|p\rangle \otimes |n\rangle$, each in a binary representation. Such a factorized representation can be useful when wanting to save space in terms of memory on a computer [7].

Finally, the Hamiltonians I use in this work have rotational symmetry and conserve total isospin and thus computed eigenstates will have "good" or fixed J and T. However, an M-scheme

algorithm only guarantees a basis keeping $J_z = M$ fixed, but not other quantities. Consequently, basis states ψ used have the following properties:

$$J_z|\psi\rangle = M|\psi\rangle$$
$$T_z|\psi\rangle = \frac{(Z-N)}{2}|\psi\rangle,$$

(1.5)

where these are not necessarily coupled to good J or T. While I have described the quantum many-body basis and someways to simplify its representation, one may still have too large of a basis size to solve the problem practically. Therefore, the number of single particle states will have to be reduced to reduce the computation time and memory required to a tractable amount. These reductions will either be a result of:

1. approximations or truncation, such as but not limited to, inert core of shells with small number of valence shell(s), functional expansions of operators, or restricting the types of excitation (particle-hole, two particle-two hole, particle-particle, etc.)

2. exact reductions to equivalent representations, such as, irreducible representations due to symmetries.

1.1.4 Representations of Operators: Computing Matrix Elements

We start with the second quantization formalism of creation and annihilation operators, where the word *second* comes from the ability to quantize field operators in this context. These operators are $c_k^\dagger$ and c_k, which create or destroy a particle in state, k, respectively. For example one could create a particle in every single basis state:

$$\prod_{k=1}^{Dim} c_k^\dagger|0\rangle = |111\ldots1\rangle$$

(1.6)

Here $|0\rangle = |000\ldots0\rangle$ is known as the vacuum state, where no particles are occupy anything.

Now imagine that an operator acts on a single particle, or two particles, or more by taking

these particles to new states. These are called one-body operators, two-body operators, and so on,

when acting on a many-body basis. These many-body operators can be represented as matrices

using tensor products and Fock space. A simple example of one body operators in Fock space

are pairs of the creation and annihilation of particles. From equation 1.1, the kinetic energy T_i is

another example of a one-body operator and the scalar interparticle interactions, V_{ij}, would be

two-body operators. These operators are converted into matrices using inner products, so that the

matrix element of an operator is:

$$O^{ab...,cd...} = \langle ab... | O | cd... \rangle, \tag{1.7}$$

where a, b, c, and d are single particle states that nucleons may occupy. An n-body operator

takes n particles in n states to n other states, or the same states, but can act on a state that has any

number of particles, including zero (vacuum). As a reminder, this is Dirac, or bra-ket, notation

where the ket, $|cd\rangle$, and the bra $\langle ab|$ is conjugate transpose of $|ab\rangle$, hence this is a scalar product.

In the creation/annihilation operator formalism, a one body operator would look like

$T = -\frac{\hbar}{2m}\frac{\partial^2}{\partial^2 x_i}$ in position space, but in the occupation space it takes the general form:

$$T = \sum_{jk} T(j,k) c_j^\dagger c_k, \tag{1.8}$$

with the sum over the single particle basis states. A two body operator would have the form:

$$V = \sum_{a<b,c<d} V(ab,cd) c_a^\dagger c_b^\dagger c_d c_c \tag{1.9}$$

where the sum is again over single particle states.

At times it becomes necessary to do algebra with the creation and annihilation operators.

Therefore one uses the fact that an annihilation operator acting on vacuum gives, due to the nature

9

of fermions only occupying states one at a time, $c_k|0\rangle = 0$ or a creation operator acting on an already occupied k-th state would give after pulling out the creation operator $c_k^\dagger|\ldots\overset{k}{1}\ldots\rangle = 0$. This leads to the conjugate transpose operation with a creation operator $\langle 0|c_k^\dagger = 0$ and $\langle\ldots\overset{k}{1}\ldots|c_k = 0$. Lastly, a consequence of fermions getting a negative sign under exchange, is that these operators anti-commute, written $\{c_{k_2}, c_{k_1}\} = 0$, $\{c_{k_2}^\dagger, c_{k_1}^\dagger\} = 0$, and $\{c_{k_2}^\dagger, c_{k_1}\} = \delta_{k1,k2}$. For example, in the last relation, for $k_1 \neq k_2$, explicitly one gets:

$$0 = \{c_{k_2}^\dagger, c_{k_1}\} = c_{k_2}^\dagger c_{k_1} + c_{k_1} c_{k_2}^\dagger$$
$$c_{k_2}^\dagger c_{k_1} = -c_{k_1} c_{k_2}^\dagger$$

(1.10)

and for $k_1 = k_2$

$$1 = \{c_{k_2}^\dagger, c_{k_1}\} = c_{k_2}^\dagger c_{k_1} + c_{k_1} c_{k_2}^\dagger$$
$$c_{k_1} c_{k_2}^\dagger = 1 - c_{k_2}^\dagger c_{k_1}$$
$$c_{k_2}^\dagger c_{k_1} = 1 - c_{k_1} c_{k_2}^\dagger$$

(1.11)

Consider two identical particles and four single particle states, a,b,c,d. The Hamiltonian typically is made of sum of a one body and a two body interaction, but here it will have only two two-body elements. First is, H(ab,bc)=0.5. Second because it is Hermitian, there is H(bc,ab)=0.5, so if it sees two particles in states b and c, it will take them to states a and b, or vice versa. In this case the fermion many-body basis has six unique anti-symmetrized states $\{1 = ab, 2 = ac, 3 = ad, 4 = bc, 5 = cd, 6 = cd\}$. Not surprisingly, for two identical particles one just gets the same matrix. That is, the only matrix elements in this two particle basis are the ones mentioned

above, which looks like:

$$H^{(2)} = \begin{bmatrix} 0 & 0 & 0 & 0.5 & 0 & 0 & 0 \\ 0 & 0 & 0 & 0 & 0 & 0 & 0 \\ 0 & 0 & 0 & 0 & 0 & 0 & 0 \\ 0.5 & 0 & 0 & 0 & 0 & 0 & 0 \\ 0 & 0 & 0 & 0 & 0 & 0 & 0 \\ 0 & 0 & 0 & 0 & 0 & 0 & 0 \end{bmatrix} \tag{1.12}$$

However, if instead one does three identical particles with the same basis and interaction, it gets more interesting. Now there are only four unique many-body states {1=abc,2=abd,3=acd,4=cbd}. Thus, because there aren't as many holes to move particles around in, then there are less total configurations. Generally, this involves creation/annihilation particle algebra In this three particle basis one gets the following non-zero matrix elements:

$$
\begin{aligned}
H_{24}^{(3)} &= \langle 2|H|4\rangle \\
&= \langle abd|H(ab,bc)c_a^\dagger c_b^\dagger c_c c_b|cbd\rangle \\
&= H(ab,bc)\langle 0|c_d c_b c_a c_a^\dagger c_b^\dagger c_c c_b c_c^\dagger c_b^\dagger c_d^\dagger|0\rangle \\
&= H(ab,bc)\langle 0|c_d c_c c_b c_c^\dagger c_b^\dagger c_d^\dagger|0\rangle \\
&= H(ab,bc)\langle 0|c_d c_c (-c_c^\dagger c_b)c_b^\dagger c_d^\dagger|0\rangle \\
&= -0.5\langle 0|0\rangle = -0.5(1) = -0.5
\end{aligned}
\tag{1.13}
$$

To get to the last step one just notices that when acting on the vacuum state to the right the pairs $c_{k_1} c_{k_2}^\dagger$ are just the identity operator that does nothing and can be moved out of the way, so there ends up being a minus sign. The only other non-zero element is $H_{24} = \langle 4|H|2\rangle$, which is the

same by symmetry of a Hermitian operator. This gives a matrix that looks like:

$$H^{(3)} = \begin{bmatrix} 0 & 0 & 0 & 0 \\ 0 & 0 & 0 & -0.5 \\ 0 & 0 & 0 & 0 \\ 0 & -0.5 & 0 & 0 \end{bmatrix} \tag{1.14}$$

Note: State 4 $|cbd\rangle$ results in negative matrix elements because c and b are reversed, but if they were in order one would get a positive number, which highlights the important of tracking signs correctly in fermion exchange.

In general the Hamiltonian interactions I use in this work will take the form $H = H_1 + H_2$, where in equation 1.1 these corresponds to the one-body term $\sum_i T_i + \sum_i U_i$ and the two-body term $\frac{1}{2}\sum_{i \neq j} V_{ij}$, respectively. The one-body part is:

$$H_1 = \sum_\alpha \varepsilon_\alpha [j_\alpha][c_\alpha^\dagger \times \tilde{c}_\beta]_{J=0} \tag{1.15}$$

and the two body part is:

$$H_2 = \frac{1}{4} \sum_{abcd} \zeta_{ab}\zeta_{cd} \sum_{JT} V_{JT}(ab,cd) \sum_{M,M_T} A_{JM,TM_T}^\dagger (ab) A_{JM,TM_T}(cd) \tag{1.16}$$

Within the model space one is supplied with the single particle energies, ε_α, and the two-body matrix elements between two states a and b, $V_{JT}(ab,cd)$. Here $\zeta_{ab} = \sqrt{1 + \delta_{ab}}$. Further, the two-body pair creation operators operators $A_{JM,TM_T}^\dagger(ab)$ are coupled to total J and T and projections $J_z = M$ and $T_z = M_T$, specifically:

$$A_{JM,TM_T}^\dagger(ab) = [c_a^\dagger \times c_b^\dagger]_{JM,TM_T} \tag{1.17}$$

12

where the coupling is accomplished via a sum over all possible individual angular momentum z-projections m_a and isospin projections μ_a involving Clebsch-Gordan coefficients, that is:

$$[c_a^\dagger \times c_b^\dagger]_{JM,TM_T} = \sum_{m_a,m_b} \langle j_a m_a, j_b m_b | JM \rangle \sum_{\mu_a,\mu_b} \langle 1/2\, m_a, 1/2\, m_b | T\, M_T \rangle c_{j_a m_a, 1/2\, \mu_a}^\dagger c_{j_b m_b, 1/2\, \mu_b}^\dagger,$$

(1.18)

which creates a state $|ba; JM, TM_T\rangle$. While three-body or higher order terms are sometimes used to account for other affects, these will not be significant in this work.

For phenomenological shell model interactions, the single particle energies and two-body matrix elements are parameters that are varied so as to obtain accurate quantities for the nuclei in the model space, such as the energy eigenvalues of the low energy spectrum. Examples of phenomenological interactions are USDB [8] for the sd-shell or GXPF1A [9] for the pf-shell, which were from derived from intermediate effective interactions computed using G-matrix theory on realistic nucleon-nucleon interactions mentioned at the end of section 1.1.2 [10].

1.1.5 Symmetries, Group Theory and Algebras

To introduce the concept of symmetry groups, let us consider a free particle with no interaction forces. For a single particle, the total angular momentum, $\vec{j} = \vec{l} + \vec{s}$, would be conserved, where one has a sum of its orbital, $\vec{l}$ and spin, $\vec{s}$, angular momentum. However for multiple particles, an important property of the nuclear Hamiltonian is that the total angular momentum, $\vec{J} = \sum_i \vec{j_i}$, and total isospin $\vec{T} = \sum_i \vec{\tau_i}$ of all the particles is conserved. Note: Sometimes I is used instead of J for total angular momentum. The representations of these symmetries have useful properties:

1. Transformation operators representing a symmetry of the system form a mathematical group structure, that is, the set of transformation operators is closed under a binary operation, for example matrix operators and matrix multiplication.

2. For a continuous symmetries, there is an associated Lie algebra of the group made

up of linear combinations of operators called generators. The generators follow commutation relations of the following form:

$$[O_a, O_b] = \sum_c f_{abc} O_c, \tag{1.19}$$

where f_{abc} are structure constants unique to the algebra and the commutator is the following operation $[O_a, O_b] = O_a O_b - O_b O_a$. The generators are called as such because they generate a transformation of the state of a system, such as a rotation.

For example in physics, these generators sometimes represent measurable values called observables. But the generators may not commute with each other, therefore they cannot be measured simultaneously. For example, in a system with rotational symmetry, the symmetry group is called SO(3). One representation of a rotation operator would take the form:

$$\Re(\vec{n}, \phi) = \exp\left(-i\frac{\vec{J} \cdot \vec{n}}{\hbar}\phi\right), \tag{1.20}$$

where one has the total angular momentum vector $\vec{J} = (J_x, J_y, J_z)$, the normal vector, $\vec{n}$ along the desired axis of rotation, and ϕ the angle of rotation. Here one possible set of generators are the operators representing the Cartesian components of the total angular momentum vector J_x, J_y, and J_z, where in this basis one can derive:

$$\Re(\alpha, \beta, \gamma) = e^{-i\frac{J_z}{\hbar}\alpha} e^{-i\frac{J_y}{\hbar}\beta} e^{-i\frac{J_z}{\hbar}\gamma}, \tag{1.21}$$

where the operators depend on the Euler angles, (α, β, γ).

3. There exists a special operator known as the Casimir invariant that commutes with all of the generators and consequently the entire Lie Algebra. The operator therefore acts as just a scalar (or number) when next to a basis state. These are typically quadratic or higher order forms of the generators. For example, in rotational symmetry one has the square of the angular momentum vector operator, $J^2 = \vec{J} \cdot \vec{J} = J_x^2 + J_y^2 + J_z^2$.

4. When an operator, O, such as a generator or the Casimir invariant, commutes with the Hamiltonian, that is, $[H, O] = 0$, then its eigenvalues, known as quantum numbers in physics, are conserved quantities. This is related to Noether's first theorem, which states that conserved quantities are implied by a dynamical symmetry, where the Hamiltonian is the generator of dynamics. A set of basis states, which are constructed from a previously solved Hamiltonian, can be labeled by a set of conserved quantities for that Hamiltonian.

Should it suit the particular problem, the Casimir invariant eigenvalues can be used as labels for closed subspaces of the solution space, known as irreducible representations, where group generators on vectors will result in vectors in the same subspace. This concept is useful when applied to conserved quantum numbers. For example, if one knows the total angular momentum quantum number is $J = 2$, then one only has to use certain basis states labeled by $J = 2$, and that simplifies computation by reducing the basis dimension.

Further, if one uses a basis arranged in irreducible representations of matrix operators that act on vector states, then the operators in this representation will take a block diagonal form according to the quantum number labels. As an example, using one Cartesian angular momentum generator, J_z and the Casimir invariant, one gets a basis of vectors like, $|jm\rangle$, where j is the eigenvalue of the Casimir invariant and m is the eigenvalue of J_z. In this basis, rotation operators will take the Wigner $\mathfrak{D}$-Matrix representation:

$$\mathfrak{R}(\alpha, \beta, \gamma) = \begin{bmatrix} \mathfrak{D}^0_{00} & 0 & 0 & 0 & 0 & 0 & \dots \\ 0 & \mathfrak{D}^0_{-1-1} & \mathfrak{D}^0_{-10} & \mathfrak{D}^0_{-11} & 0 & 0 & \dots \\ 0 & \mathfrak{D}^0_{0-1} & \mathfrak{D}^0_{00} & \mathfrak{D}^0_{01} & 0 & 0 & \dots \\ 0 & \mathfrak{D}^0_{1-1} & \mathfrak{D}^0_{10} & \mathfrak{D}^0_{11} & 0 & 0 & \dots \\ 0 & 0 & 0 & 0 & \mathfrak{D}^0_{-2-2} & \mathfrak{D}^0_{-2-1} & \dots \\ 0 & 0 & 0 & 0 & \mathfrak{D}^0_{-1-2} & \mathfrak{D}^0_{-1-1} & \dots \\ \vdots & \vdots & \vdots & \vdots & \vdots & \vdots & \ddots \end{bmatrix}, \qquad (1.22)$$

where the matrix elements are $\mathfrak{D}^j_{m'm}(\alpha,\beta,\gamma) = \langle jm'|\mathfrak{R}(\alpha,\beta,\gamma)|jm\rangle$. These blocks are indecomposable subspaces, that is, they act independent of each other. So again as an example, if one acts on a vector with values only in a certain block, then the result is as if the operator matrix had zeros everywhere else:

$$\mathfrak{R}(\alpha,\beta,\gamma)\Psi = \Psi'$$

$$
\begin{bmatrix}
\mathfrak{D}^0_{00} & 0 & 0 & 0 & 0 & 0 & \cdots \\
0 & \mathfrak{D}^1_{-1-1} & \mathfrak{D}^1_{-10} & \mathfrak{D}^1_{-11} & 0 & 0 & \cdots \\
0 & \mathfrak{D}^1_{0-1} & \mathfrak{D}^1_{00} & \mathfrak{D}^1_{01} & 0 & 0 & \cdots \\
0 & \mathfrak{D}^1_{1-1} & \mathfrak{D}^1_{10} & \mathfrak{D}^1_{11} & 0 & 0 & \cdots \\
0 & 0 & 0 & 0 & \mathfrak{D}^2_{-2-2} & \mathfrak{D}^2_{-2-1} & \cdots \\
0 & 0 & 0 & 0 & \mathfrak{D}^2_{-1-2} & \mathfrak{D}^2_{-1-1} & \cdots \\
\vdots & \vdots & \vdots & \vdots & \vdots & \vdots & \ddots
\end{bmatrix}
\begin{bmatrix}
0 \\ 0 \\ 0 \\ 0 \\ \frac{1}{\sqrt{5}} \\ \frac{1}{\sqrt{5}} \\ \vdots
\end{bmatrix}
=
\begin{bmatrix}
0 \\ 0 \\ 0 \\ 0 \\ \frac{1}{\sqrt{5}}(\mathfrak{D}^2_{-2-2}+\mathfrak{D}^2_{-2-1}+\cdots) \\ \frac{1}{\sqrt{5}}(\mathfrak{D}^2_{-1-2}+\mathfrak{D}^2_{-1-1}+\cdots) \\ \vdots
\end{bmatrix}
$$

Here my initial state vector Ψ is non-zero only in the J=2 block, and due to the structure of the matrix operator, so is the resulting state vector Ψ'. Thus I ignore, better yet remove, all of the other blocks of the matrix operator acting on the state, because all elements are being multiplied by zero. This allows for an exact finite representation, where one does not have to worry about infinite sums. However, there are situations when infinite sums are unavoidable, and this is usually the case in computational quantum physics research, so the hope is that truncating higher energy blocks would give a good approximation.

1.1.6 Wigner-Eckart Theorem

An indispensable mathematical relation for applications to quantum physics is the Wigner-Eckart theorem, which applies to matrix elements of tensor operators transforming under a symmetry group. Spherical tensors transform under the rotation group symmetry SO(3), or

equivalently SU(2), and these include angular momentum and isospin operators. The Wigner-Eckart theorem factorizes matrix elements of operators into the Clebsch-Gordan coefficient, which depends on orientation or spin component, M, and the reduced matrix element that only depends on J. Specifically, using the standard convention of Edmonds [11]:

$$\langle JM|T_q^{(k)}|J'M'\rangle = \frac{1}{2J_f+1}\langle J'M'kq|JM\rangle\langle J||T^{(k)}||J'\rangle \tag{1.23}$$

where k is known as the rank of the spherical tensor and q is the component, where $-k \leq q \leq k$. The Clebsch-Gordan coefficients, $\langle J'M'kq|JM\rangle$, come from angular momentum addition in the coupling of two angular momenta. The coupled state with total angular momentum, J, and z-component, M, is then the sum over all possible values of the two individual z-components, M' and q,:

$$|JM\rangle = \sum_{M'=-J'}^{J'} \sum_{q=-k}^{k} |J'M'kq\rangle\langle J'M'kq|JM\rangle \tag{1.24}$$

Because of selection rules, the Clebsch-Gordan coefficients are zero unless $M' + q = M$ and $|J' - k| \leq J \leq J' + k$, reducing hte number of matrix elements to compute. For example, since the square of total angular momentum J^2 acts like a scalar on the basis states or rank $k = 0$ operator, one gets also that $q = 0$, so the selection rules for matrix elements of the form $\langle JM|J^2|J'M'\rangle$ are $\Delta M = M - M' = 0$ and $\Delta J = J - J' = 0$.

1.2 Nuclear Transitions

1.2.1 The Weak Nuclear Force

The weak nuclear force is known for decay or capture reactions. For example, electron emission would result in the nucleus losing a neutron and gaining a proton; hence changing its charge but not changing much in size or mass. Later, it was discovered that neutrinos must also

be involved to account for missing energy. Relevant reactions in this work are:

$$\beta^- \text{ Decay (Electron Emission)} \quad {}_Z^A X \to {}_{Z+1}^A Y + e^- + \bar{\nu}_e$$

$$\beta^+ \text{ Decay (Positron Emission)} \quad {}_Z^A X \to {}_{Z-1}^A Y + e^+ + \nu_e$$

$$\text{Electron Capture} \quad {}_Z^A X + e^- \to {}_{Z-1}^A Y + \nu_e$$

$$\text{Positron Capture} \quad {}_Z^A X + e^+ \to {}_{Z+1}^A Y + \bar{\nu}_e$$
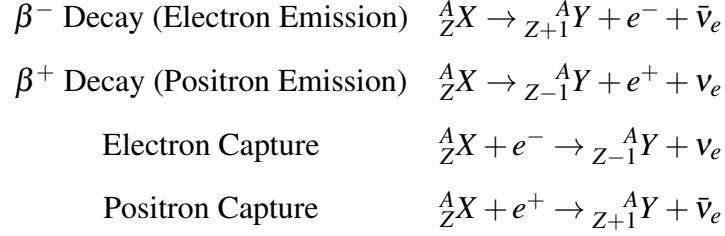
Here X and Y are parent and daughter nuclei, respectively, the $e^{\pm}$ is the (positron) electron, ν_e is the electron neutrino, and $\bar{\nu}_e$ is the electron anti-neutrino.

The V-A theory [2] for charge changing weak interactions causes transitions like beta decay and electron capture, where the nucleus changes its number of neutrons and protons, hence its charge. The theory has two major components, where the first *vector* term gives Fermi transitions and the second *axial vector* term gives Gamow-Teller transitions:

$$V_{weak} = g_V O_F + g_A O_{GT}, \tag{1.25}$$

where gs are coupling factors and the O are the respective transition operators. The Fermi transition operator is proportional to the sum of over all of the individual nucleons of raising or lowering ladder operators in isospin space, or just the ladder operator of the total isospin for the entire nucleus:

$$O_F = T^{(\pm)} = \sum_i \tau_i^{(\pm)} \tag{1.26}$$

The plus or minus depends on whether a proton becomes a neutron or vice versa. Similarly, the Gamow-Teller term is:

$$O_{GT} = \sum_i \tau_i^{(\pm)} \vec{\sigma}_i \tag{1.27}$$

The Fermi term commutes with the square of the total isospin $[T^{(\pm)}, T^2] = 0$ and therefore does not change isospin (or angular momentum) for wave functions of the entire nucleus. However, both operators must change the third component of isospin $T_z = Z - N$ depending on the type of

reaction.

As the Gamow-Teller interaction operator does not commute with the total angular momentum or total spin, it changes both the angular momentum quantum number, J, and the isospin quantum number, T, for the nuclear wave function. In calculations, the above leads to simplying selection rules. Specifically, for Fermi transitions $\Delta J = 0$ and $\Delta T = 0$, while for Gamow-Teller $\Delta J = 0, \pm 1$ and $\Delta T = 0, \pm 1$.

1.2.2   Weak Processes in Massive Stars

One of the major motivations for studying the nuclear physics of stars is to understand the origin of the elements, known as nucleosynthesis, and to explain the relative abundances for each isotope. A star like our Sun will mostly produce helium from hydrogen, but only elements up to ^{16}O in significant amounts through its lifetime. These lighter elements reside in the lower energy s and p nuclear shells. Thus, in this work I focus on nuclear processes in massive stars, which are on the order of ten solar masses and heavier, especially because through fusion they can produce elements as heavy as iron and nickel from the pf-shell.

The reason massive stars fuse larger elements is their larger mass leads to even larger gravitational pressure. Thus, they get much denser and hotter in their cores before they run out of nuclear fuel, but also it is these higher densities and temperatures that allow the ignition of fusion reactions involving heavier elements. By the time a massive star collapses it will have gone through multiple ignition cycles. The core becomes denser igniting a new type of fusion for heavier elements up to iron with the previous types of fusion for lighter elements occurring in successive outer shells as in Figure 1.3. The higher densities and temperatures gives a higher kinetic energy of particles allowing the electrical repulsion of the protons in different nuclear reactants to be overcome, which is more important as the nuclear reactants get larger.

According to Woosley and Heger, while our hydrogen burning Sun has 150 g/cm^3 in core density and will continue burning for billions of years, the core of a massive star starts out around
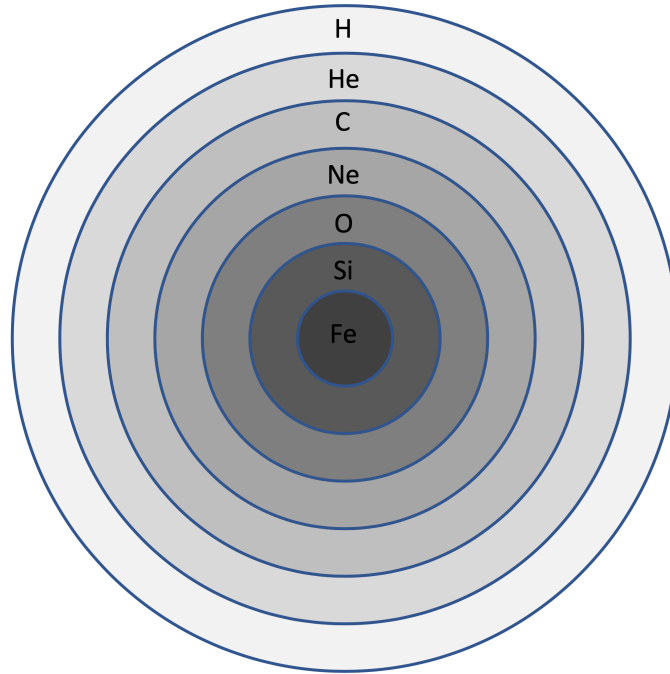
Figure 1.3: The layers of a massive star near the end of its life with an iron core at the center, followed by a silicon burning shell up to hydrogen burning in its outermost shell.

1-2 orders of magnitude less dense and will burn hydrogen in its core for tens of millions instead. The massive stellar densities are increasing at each stage, but also length of each stage of burning. As the star hits helium burning the density is upwards of 10^3 g/cm^3, which lasts for around one million years. Then carbon burning it reaches 10^5 g/cm^3 falling in length dramatically to only a thousand years. Neon and oxygen burning happen at densities near 10^{6-7} g/cm^3 and only last a year. Finally silicon burning start above 10^8 g/cm^3, and get near 10^{10} g/cm^3 before collapse initiates, where this stage lasts only days [12].

Increasing density is associated with increasing temperature. For example, in comparison, our sun is about 4000 K on the surface and tens of millions of kelvin at the core, but a massive stellar core can reach near a hundred billion kelvin, which gives an energy range of stellar core from 0.001 to 10 MeV. In fact up to carbon burning the core when in hydro-static equilibrium follows a so-called polytropic trend where the central temperature and density are related as $T_c \propto \rho_c^{1/3}$. Then the electrons start to become degenerate and relativistic and the density grows

faster with temperature [12].

These temperatures are highly relevant to the quantum excitation levels of nuclei, which are on the order of keV and MeV. Under the Fermi gas approximation for nucleons described in Bethe et al. [13], using the density of nuclear levels along with their Boltzmann probability at a given temperature, T, one gets that the average excitation energy, E_x, as follows:

$$E_x = a(kT)^2, \tag{1.28}$$

where $a \approx \frac{A}{8MeV}$ is the level density parameter parameter relating to the mass number, A, of a chosen nucleus and k is Boltzmann's constant. As an example, if one chooses $A = 56$ and $kT = 1$ MeV, one gets an average excitation of 7 MeV. This is relevant context, but does not yet explain the significance of the weak nuclear force.

Bethe et al. [13] further described two important factors determining the composition and stability of the stellar core, namely the entropy per nucleon of the core and the presence of degenerate electrons, which are highly sensitive to weak nuclear interactions. First, entropy is important because low entropy means implies there are more bound neutrons and protons, hence heavy nuclei, while high entropy would mean are more disordered mix of more particles made up of lighter nuclei and disassociated protons or neutrons. Second, massive stars in their early stages of burning release energy primarily via photons, but around silicon burning neutrino emission dominates as a byproduct of weak nuclear force reactions, especially electron capture [12]. While weak nuclear processes that create neutrinos happens slowly and out of equilibrium relative to strong nuclear and electromagnetic processes, neutrinos at typical pre-collapse densities below 10^{12} g/cm^3 so weakly interact that they easily carry away heat. At higher density, neutrinos start to scatter more strongly, getting trapped and returning some of the heat to the collapsing star aiding the supernova explosion. Thus weak processes are crucial in the release of energy and entropy, which cools the star and keeps the core at low entropy. Third, due to the Pauli Exclusion

Principle, electrons cannot be in the same state (non-degeneracy) and this degeneracy pressure helps to hold up the star. Therefore the ratio of electrons to baryons, or electron fraction, Y_e, becomes an important quantity [13].

Eventually a massive star will become so dense that it collapses and explode in a supernovae leaving behind a neutron star or blackhole, where the environment becomes one hundred times hotter. This gravitational instability happens when the electrons can no longer hold up the star, and the core reaches about 1.4 solar masses or the Chandrasekhar mass, M_{lim}, which depends on the electron fraction mentioned above and the stellar density:

$$M_{lim} \propto \frac{1}{\mu_e^2} \propto \frac{1}{(\rho Y_e)^2} \tag{1.29}$$

Lastly, the weak nuclear force plays an important part in the nucleosynthesis of heavy elements via the s-process and the r-process, where neutrons are captured by seed nuclei that beta decay into new elements of higher proton number. The s-process, where s is for *slow*, happens when neutron captures are slower than beta decay, but also where there are adequate numbers of free neutrons. The main s-process occurs in helium flashes of low mass stars, but a weaker contribution to abundances happens during helium burning in massive stars with some contribution from carbon and oxygen burning [12]. Neutron creating processes are alpha capture on ^{13}C and ^{22}Ne, where elements in the ranges of $A = 22 - 50$ and $63 - 209$ have significant s-process contributions [14]. However, during stellar collapse and supernovae the temperatures and densities are high enough to make the neutron capture rate faster than beta decay. Highly degenerate core electrons are Pauli blocked from decaying to low momentum states, but are still captured on protons and nuclei, a process called neutronization that lowers Y_e and accelerates collapse. This results in the r-process, where higher neutron density allows for many *rapid* and successive neutron captures that can make very large elements around $A = 200$. As mentioned above, helium burning could last a million years whereas supernovae collapse happens on the order

of milliseconds and the explosion only hours [12]. Hence, in general knowing the relevant energy and time scales involved in these strong and weak nuclear processes allows for computations of both stellar evolution and elemental abundances.

1.2.3 Computing Transition Strengths and Rates

Relative to the strong nuclear force, the weak interactions in the previous section (Fermi/GT) can be treated as perturbations. One can use time dependent perturbation theory, which results in Fermi's Golden Rule [2] for transition rates, or probability of a change of state per unit time:

$$\lambda_{if} = \frac{2\pi}{\hbar} \int_{-\infty}^{\infty} |\langle f|V|i\rangle|^2 \delta(E_i - E_f) D(E_f) dE_f, \tag{1.30}$$

where V is the perturbation transition operator, D(E) is the density of states. The Dirac delta function assures that these final states have the same total energy as the initial states. Hence energy will be conserved by this transition, with some energy carried away by neutrinos and electrons.

In experiments and applications, the dynamics are often orientation independent. Thus for the squared matrix elements in λ_{if} above, one sums over possible angular momentum orientations M, averages over possible initial states M_i, and sums over final states M_f, applying the Wigner-Eckart theorem to get:

$$\begin{aligned} B_{if}(V) &= \frac{1}{2J_i+1} \sum_M \sum_{M_i} \sum_{M_f} |\langle J_f M_f | V_M^{(J)} | J_i M_i \rangle|^2 \\ &= \frac{1}{2J_i+1} \sum_M \sum_{M_i} \sum_{M_f} |\langle J_i M_i J M | J_f M_f \rangle|^2 \langle J_f || V^{(J)} || J_i \rangle^2 \\ &= \frac{|\langle J_f || V^{(J)} || J_i \rangle|^2}{2J_i+1} \sum_M \sum_{M_i} |\langle J_i M_i J M | J_f M_f \rangle|^2 \\ &= \frac{|\langle J_f || V^{(J)} || J_i \rangle|^2}{2J_i+1} \end{aligned} \tag{1.31}$$

where $\sum_M \sum_{M_f} |\langle J_f M_f kq | J_i M_i \rangle|^2 = 1$ via orthogonality relations for the Clebsch-Gordan coefficients [11].

These B_{if} are called the reduced transition probabilities. If one instead computes matrix elements that are doubly-reduced with respect to both angular momentum isospin, then one applies the Wigner-Eckart theorem again. Since T_z is fixed, then one does not need to average or sum across states, and for a rank 1 raising or lowering operator, such as in Gamow-Teller:

$$B_{if}(V) = \frac{1}{2J_i + 1} |\langle J_f T_f |||V^{(J,T)}|||J_i T_i\rangle|^2 \frac{|\langle T_i T_{z,i} T(\pm 1) | T_f T_{z,f}\rangle|^2}{2T_f + 1} \tag{1.32}$$

Now, if one fixes the initial state, i, one gets the transition *strength function* in terms of the final states, f as:

$$S_V(E_i, Q_{if}) = \sum_f \delta(Q_{if} - E_f + E_i) B_{if}(V) \tag{1.33}$$

As an example, an analytical closed form for the reduced transition probabilities of the Fermi operator is known:

$$B_{if}(O_F) = T(T+1) - T_z^i(T_z^f), \tag{1.34}$$

Further, the the Fermi operator commutes with the iso-spin conserving Hamiltonians I use here, that is, $[O_F = T^{(\pm)}, H] = 0$. Thus, transitions from initial states of the parent nucleus go to final states of the daughter nucleus of the same J,T, and energy, where these states of the daughter nucleus are known as isobaric analogs. In actual nuclei, Coulomb repulsion of the nuclear protons would shift the energy of isobaric analogs. Because the computation of Fermi transition rates are mostly trivial, in this work I focus on the Gamow-Teller interaction.

1.2.4 Thermal Rates in Stellar Environments

In a star, the nuclear reactions mentioned in the previous section don't occur independently but are subject to a background plasma of nucleons, nuclei, electrons, photons, and neutrinos at a

certain density ρ and temperature, T. However, the rates have a similar form to section 1.2.3 on Fermi's Golden Rule. To get the total rate for a specific interaction one must sum over all initial parent states and final daughter states giving the following:

$$\lambda(\rho,T) = \sum_i P_i \sum_f \lambda_{if} = \sum_i \frac{(2J_i+1)e^{-E_i/kT}}{G(T)} \sum_f B_{if}(V)\Phi_{if}(Q_{if},\rho,T) \qquad (1.35)$$

where $P_i = \exp{-E_i/kT}/G$ is the occupation probability, and $G = \sum_i \exp{-E_i/kT}$ is the partition function, for parent nuclei. Similar to the density of states, one has Φ_{if} a phase space factor that depends on the transition energy, Q_{if} between initial parent and final daughter states, and captures the effect of the electrons and neutrinos. The phase space factor is akin to the density of final states in Fermi's Golden Rule in equation 1.30. It is dependent on the type of process, such as beta decay or electron capture, and will be defined later in the text as necessary. At high temperatures, the probabilities for initial parent states become larger and head towards equality with a value of $\frac{e^{-0}}{G(T=\infty)} = \frac{1}{G(T=\infty)}$, where $G(\infty)$ is a constant equal to the total number of possible states for the nucleus. Thus, excited states become ever more important as the temperature increases in accordance with the average excitation energy from equation 1.28.

1.3 Obtaining Eigenstates and Spectral Decompositions

The next step after obtaining the quantum Hamiltonian matrix is to diagonalize for the eigenvalues and eigenvectors. Throughout this research, I worked with very large, sparse matrices as will be explained in this section. Therefore the Lanczos algorithm [1] is indispensable to this work. Further, to obtain other relevant spectral quantities whether symmetry group decompositions or transition strength functions, a modified version of the Lanczos algorithm is used, which I describe in succeeding sections. But first I give some context for why I use the Lanczos algorithm.

For the symmetry group decompositions in chromium the basis size was in the millions, so these could easily be done on modern desktop computers. However, this is not the case for

many weak nuclear force transitions in the middle of the pf-shell with larger basis dimension. Many of the astrophysically relevant nuclear isotopes in a pre-collapse massive star exist around the iron abundance peak with atomic mass number $A = 50 - 65$. In these isotopes, the basis size can exceed one billion, hence storing a single state vector for a nucleus would take at least four gigabytes of memory. Also, relevant are the operators that act on a state vector and their sparsity, where sparser operator matrices, that is matrices with a relatively small number of non-zero elements, are amenable to fast methods of diagonalization. Specifically, I use the BIGSTICK code, which uses an *M-scheme* basis for our calculations that has the z-component of angular momentum $M = J_z$ is fixed for the basis vectors [7] [15]. This leads to relatively large, sparse matrix operators, especially the Hamiltonian operator, compared to *J-scheme* codes that use a basis where total angular momentum, J, is fixed [16].

For example, in the basis used to represent quantum states, ^{57}Co has a basis dimension of 980,474,907 whose square is the number of matrix elements, about 10^{18}. But the actual number of non-zero matrix elements is on the order of 10^{11} giving a sparsity of 10^{-7}. Further, assuming four bytes per basis element this means one single vector takes about 4 GB, and to converge a couple hundred eigenvectors may take a few thousand Lanczos iterations, where such memory requirements exceed typical desktop computer capabilities. Fortunately, BIGSTICK is highly suited to the task being highly parallel with MPI and OpenMP capabilities to increase processing power along with factorized on-the-fly matrix element creation to to reduce memory load.

To compound the situation, as explained above, the probability of nuclear excitation in massive stellar cores near collapse temperatures ($> 10^9$ K), is such that many excited states of a parent nucleus must be used to compute accurate weak nuclear force transitions rates. But even after computing the eigenstates of the parent nucleus, for each eigenstate, one must also compute the spectral distribution of the transition operator requiring more iterations and computer memory. This was understood in the pioneering work on this subject by Fuller, Fowler and Newman [17], where an approximation known as the Brink-Axel hypothesis [18][19] about the

form of transition strength distributions was applied to simplify calculations by avoiding the need to compute strength functions for excited states. However as will be discussed in Chapter 3, to improve the accuracy of thermal rates, the computation of these excited state distributions cannot legitimately be avoided. Thus one can see how this problem quickly becomes intractable without the use of modern supercomputers, as well as, approximations like the one that I will develop later in this text.

1.3.1 Diagonalization and the Lanczos Algorithm

The code used in this work is BIGSTICK [15], an M-scheme code, where M is the quantum number associated with eigenvalues of the generator J_z. This means that M is fixed, but the total angular momentum quantum number J is not. Consequently this basis produces matrices that are larger, but are also very sparse in terms of non-zero matrix elements. These are ideal for the Lanczos iterative method, where it is equivalent to the Arnoldi method for Hermitian operators ($H^\dagger = H$). The method involves taking the matrix, H, that one wishes to diagonalize and applying it to an initial, usually random, *pivot* vector, v_1 as follows:

1. Let $\alpha_1 = \langle v_1|H|v_1\rangle$ and $\beta_0 = 0$.

2. Let $w_1 = H|v_1\rangle - \alpha_1|v_1\rangle$. Then for $j = 2,...,m$ repeat steps 3-5.

3. Let $\beta_{j-1} = \langle w_{j-1}|w_{j-1}\rangle$

4. Let $v_j = \frac{|w_{j-1}\rangle}{\langle w_{j-1}|w_{j-1}\rangle}$ (v_j is w_{j-1} normalized)

5. Let $|w_j\rangle = H|v_j\rangle - \alpha_j|v_j\rangle - \beta_{j-1}|v_{j-1}\rangle$

Solving for $\alpha_j |v_j\rangle$ gives the following result:

$$H|v_1\rangle = \alpha_1|v_1\rangle + \beta_1|v_2\rangle$$

$$H|v_2\rangle = \beta_1|v_1\rangle + \alpha_2|v_2\rangle + \beta_2|v_3\rangle$$

$$H|v_3\rangle = \beta_2|v_2\rangle + \alpha_3|v_3\rangle + \beta_3|v_4\rangle \qquad (1.36)$$

$$\cdots$$

$$H|v_k\rangle = \beta_{k-1}|v_{k-1}\rangle + \alpha_k|v_k\rangle$$

Thus, a tri-diagonal matrix will result with matrix elements $H_{ij}^{(k)} = \langle v_i|H|v_j\rangle$:

$$H^{(k)} = \begin{bmatrix} \alpha_1 & \beta_1 & 0 & 0 & 0 & 0 & 0 \\ \beta_1 & \alpha_2 & \beta_2 & 0 & 0 & 0 & 0 \\ 0 & \beta_2 & \alpha_3 & \beta_3 & 0 & 0 & 0 \\ 0 & 0 & \beta_3 & \ddots & \ddots & 0 & 0 \\ 0 & 0 & 0 & \ddots & \ddots & \beta_{k-2} & 0 \\ 0 & 0 & 0 & 0 & \beta_{k-2} & \alpha_{k-1} & \beta_{k-1} \\ 0 & 0 & 0 & 0 & 0 & \beta_{k-1} & \alpha_k \end{bmatrix} \qquad (1.37)$$

The extremal eigenvalues of $H^{(k)}$ approximate well the extremal eigenvalues of the original matrix H. To get eigenvectors, left-multiply the eigenvectors of $H^{(k)}$ by the matrix $V = [|v_1\rangle, |v_2\rangle, \ldots, |v_k\rangle]$. This method can converge very quickly, where on the order of tens of iterations one can get a few eigenvalues quite accurately. Theoretically in exact arithmetic, the error in the first eigenvalue has been proven to be bounded above by a function that decreases exponentially in the number of iterations, where the constant depends on the gap between successive eigenvalues and also between the desired eigenvalue and the extremal ones. A similar bound holds for other eigenvalues. [1]

1.3.2 Modified Lanczos - Spectral Decomposition in Symmetry Groups

In this section and the next, I will outline two applications of a modified Lanczos algorithm that is used to obtain spectral distributions. First, in Chapter 2, it will be necessary to compute the decomposition of an eigenstate of a certain nucleus to see the fraction of the eigenstate that lies in each irreducible representation (irrep) of the Casimir. The fraction, or probability, of a nuclear eigenstate in a certain irrep is $P(|\mathfrak{C}\rangle) = |d_1(\mathfrak{C})|^2$. One may use the Casimir eigenvalues to label the irreducible representations. Hence one does the following:

1. Pick an initial eigenvector of the nuclear Hamiltonian as a pivot to decompose. That is, $|\psi\rangle = |v_1\rangle$. *Note that for the spectral decompositions in this work, the pivot vectors are not random.*

2. Perform the Lanczos iteration for a desired number of steps, m, using the Casimir invariant operator, $\mathfrak{C}$ of the desired symmetry group.

3. Before transformation, the approximate eigenvectors $|\mathfrak{C}\rangle$ of the matrix $\mathfrak{C}$ are in a basis in terms of the Lanczos vectors v_i as $|\mathfrak{C}\rangle = \sum_{i=1}^{m} d_i(\mathfrak{C})|v_i\rangle$. Since the pivot is the first Lanczos vector, then the approximate coefficient for a specific Casimir eigenvalue is just the first component of the corresponding vector $|\mathfrak{C}\rangle$, up to a phase. Store all the values $d_1(\mathfrak{C})$ for each Casimir eigenstate, $|\mathfrak{C}\rangle$.

Like the usual Lanczos method, this method converges efficiently to the desired result but instead of a set of eigenvalues and eigenvectors, one gets a spectral distribution via its moments (α_i, β_i), where this method provides twice as many moments as iterations. These moments describe the overall shape of the distribution [20]. The second application of this method is to transition rates between different nuclear states, which will be developed in the next section.

1.3.3 Modified Lanczos - Spectral Decomposition in Transition Strength Functions

The second application of the decomposition algorithm is transition strength functions. The transition strength of an operator, V, of the initial wavefunction to a certain final daughter state, $|\psi_f\rangle$, is related to the squared matrix element $|\langle\psi_i|V|\psi_f\rangle|^2 = |d_1(\psi_f)|^2$ up to appropriate scaling factors. The set created from varying final strength, f, is the strength function with m total points. Similarly to the previous section, one does the following:

1. Pick an initial eigenvector, $|\psi_i\rangle$, of the nuclear Hamiltonian as a pivot to decompose into daughter states. Then apply the transition operator, V to get $|v_1\rangle = V|\psi_i\rangle$

2. The transition operator may change previously conserved quantities, such as, total angular momentum, J, or isospin, T. Therefore if desirable, decompose $|v_1\rangle$ in the corresponding Casimir invariant operators, J^2 and T^2.

3. To get the amplitudes of the pivot in the final daughter states, $|\psi_f\rangle$, use the nuclear Hamiltonian to provide the daughter states. Perform Lanczos with H a desired number of times, m.

4. Similarly to above, the basis is in terms of the Lanczos vectors v_i as daughter states $|\psi_f\rangle = \sum_{i=1}^{m} d_i(\psi_f)|v_i\rangle$. Since the pivot is the first Lanczos vector, then the approximate coefficient for a specific transition $i \to f$ is just the first component of the corresponding vector $|\psi_f\rangle$, up to a phase. Store all the values $d_1(\psi_f)$ for each final daughter state, $|\psi_f\rangle$.

Thus, while producing the initial state happens differently compared to symmetry group decompositions from above, the filtering into components for strength functions is essentially the same operation.

Chapter 2

Quasidynamical symmetries in the backbending of chromium isotopes

Quasi-dynamical symmetries in the backbending of chromium isotopes

Raúl A. Herrera

Department of Physics and

Center for Astrophysics and Space Sciences,

University of California San Diego,

9500 Gilman Drive, La Jolla, CA 92093

Calvin W. Johnson

Department of Physics, San Diego State University,

5500 Campanile Drive, San Diego, CA 92182 and

Center for Astrophysics and Space Sciences,

University of California San Diego, 9500 Gilman Drive, La Jolla, CA 92093

Abstract

Background: Backbending is the well-known abrupt change in the moment of inertia along the yrast line. Prior mean-field calculations in ^{48,49,50}Cr suggest a change from strongly prolate to more spherical configurations as one crosses the backbending and increases in angular momentum.

Purpose: In order to better illuminate the evolution as one goes along the yrast line, we analyze wavefunctions into group-theoretical components, looking for evidence of *quasi-dynamical* symmetry, that is, the same or similar decomposition across members of a band.

Methods: We efficiently decompose configuration-interaction shell-model wavefunctions of ^{48,49,50}Cr into subspaces labeled by eigenvalues of Casimir operators, specifically the SU(2) groups L (total orbital angular momentum) and S (total spin), and the groups SU(3) and SU(4), using a modified Lanczos algorithm. We worked in the *pf*-shell using semi-phenomenological interactions.

Results: We find strong signatures of quasi-dynamical symmetry, albeit often of a different character above and below the backbending. In some cases we can continue a band, marked out by its decomposition, both before and after band crossings. While decompositions in SU(3) showed the strongest evolution, they did not suggest a decrease in deformation.

Conclusions: We see strong and persistent quasi-dynamical symmetry in all four groups, but no evidence for a decrease in deformation in SU(3) configurations. We point out with a simple example that mean-field and SU(3) may give very different pictures of deformation. Nonetheless these decompositions, which do not require a special basis but only matrix elements of Casimir operators, provide another tool for investigating complex behavior of nuclei.

34

I.   INTRODUCTION

Backbending is an abrupt change in the nuclear moment of inertia along the yrast line [21], seen in nuclides ranging from ^{22}Ne [22] through the actinides [23]. In a rotational band with constant moment of inertia the gamma transition energy $E_\gamma(I) = E(I) - E(I-2)$ grows steadily with angular momentum I, but in backbending $E_\gamma(I)$ abruptly falls and then rises again with a different slope, as illustrated in Fig. 1 for ^{48,49,50}Cr.

There are three general explanations for the change in the moment of inertia [21]

● a change in deformation;

● a change from superfluid to normal phase;

● a change in alignment of quasiparticles.

Of course, backbending may be due to a mixture of these explanations; furthermore, it may not be the same for all nuclei [24].

Because backbending occurs mostly frequently in heavy nuclei, most calculations of backbending have used mean-field and related methods [25], such as cranked Hartree-Fock-Bogoliubov [26–29] and the (angular-momentum) projected shell model [30]. A favorite target of theory, however, has been backbending in the chromium isotopes [31–36], because in addition to mean-field and similar studies [24, 37, 38] one can fully diagonalize the nuclear Hamiltonian in the $1p$-$0f$ ('pf') shell using configuration-interaction methods [39–46].

We will discuss some of these prior investigations in more detail below. We are especially motivated, however by recent assertions [44] that for ^{48}Cr the lower sub-band (below the backbending) can be associated with a well-defined intrinsic state, but not the upper sub-band (above the backbending). We follow this up by decomposing the nuclear wavefunctions into subspaces defined by group Casimir operators, that is, operators which are invariant under all elements of a Lie group and its related algebra [47–49]. We see strong characteristics of *quasi-dynamical symmetry*, that is, consistent fragmentation of the wavefunction with increasing I; in most cases we see a change as one crosses the backbending, and in SU(3) we see significant evolution of the fragmentation in the upper sub-band as I increases.

As described below in section II B, we use an efficient method to decompose a wavefunction according to subspaces labeled by eigenvalues of Casimir operators. We choose total orbital angular momentum L and total spin S, both of which belong to group the group SU(2), as well as the
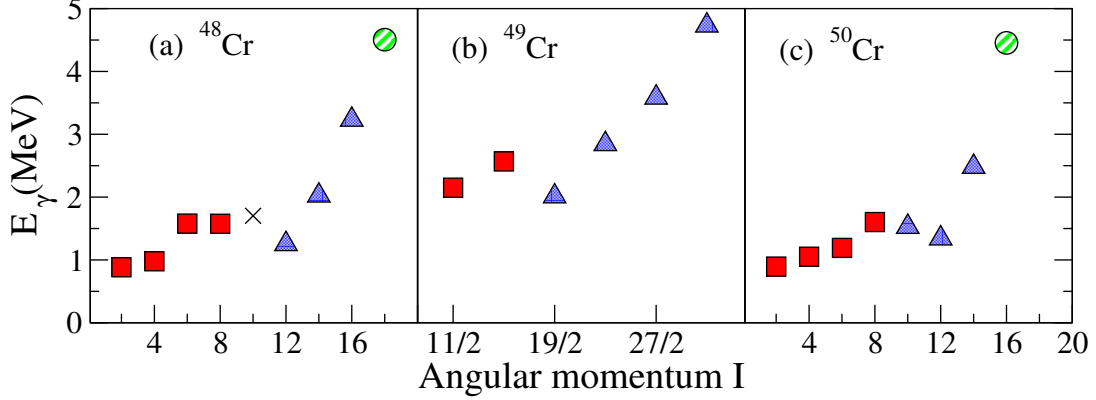
FIG. 1: Backbending in $^{48-50}$Cr, as signaled by the evolution of $E_\gamma(I) = E(I) - E(I-2)$. The distinct shapes/colors represent, to the best of our ability to identify, different configurations along the yrast as discussed in detail in the text: (red) solid squares for the lower sub-band, (blue) dotted triangles for the upper sub-band, and a black 'x' and (green) striped circle for upper and lower 'intruder' levels, respectively. The calculated values are in good agreement with experiment (not shown).

groups SU(3), and SU(4). We limit ourselves to two-body Casimirs.

II. MICROSCOPIC METHODS

A. Configuration-interaction shell model

We carry out calculations in the framework of the configuration-interaction (CI) shell model [50–52], which expresses the nuclear Hamiltonian as a large-dimensioned matrix in a basis of shell-model Slater determinants (antisymmetrized products of single-particle states), recasting the many-body Schrödinger equation as a matrix eigenvalue problem,

$$\hat{H}|\Psi_i\rangle = E_i|\Psi_i\rangle. \tag{1}$$

We find the low-lying eigenpairs, via the Lanczos algorithm, using the `BIGSTICK1` configuration-interaction code [7]. Because the Hamiltonian is rotationally invariant, the total magnetic quantum number M (or J_z, the z component of the total angular momentum) is conserved and one can easily construct a basis with fixed M; this is called an M-scheme basis.

Although *ab initio* calculations for $0p$-shell nuclides are now routine, for the chromium isotopes

36
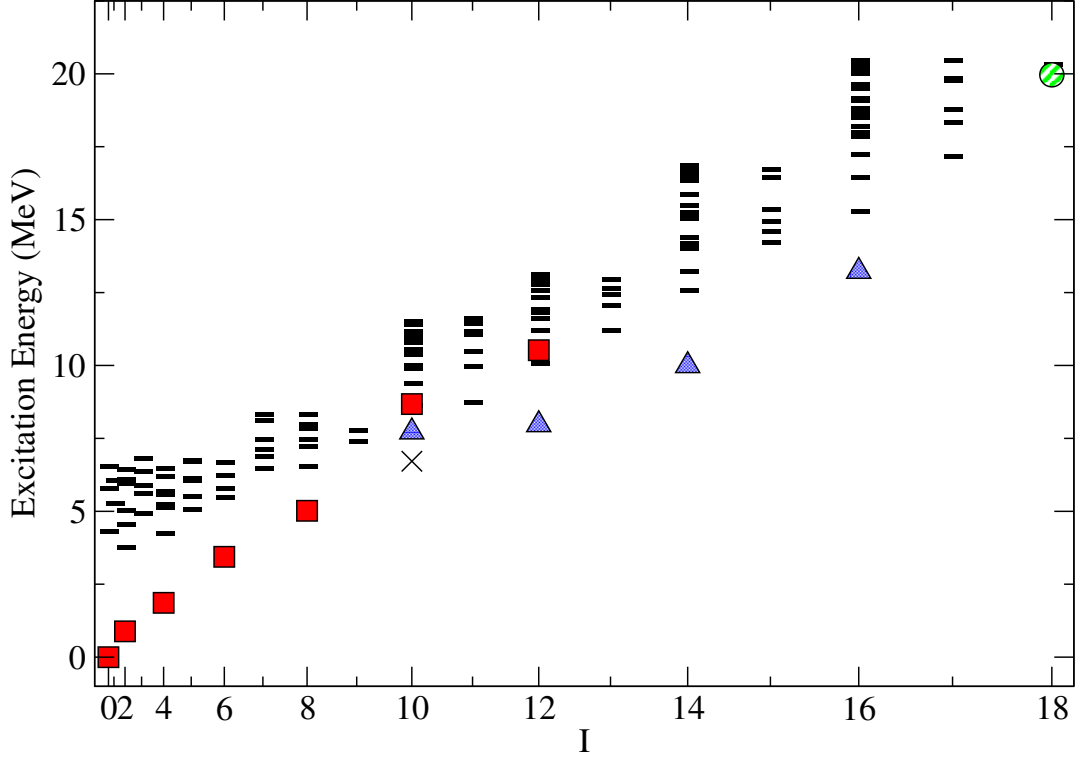
FIG. 2: Calculated spectrum of ^{48}Cr. The *x*-axis (angular momentum *I*) is scaled as $I(I+1)$ so as to emphasize rotational bands. The labeling of levels, i.e., (red) squares, (blue) triangles, and (green) circles, correspond to the same (initial) state as in Panel (a) of Fig. 1. According to our decompositions, the yrast state at $I = 10$, marked by as 'x,' belongs to neither the lower nor upper sub-bands. Bars indicate levels found in our calculation but which we do not decompose.

we use the modified G-matrix interaction for the $1p$-$0f$ (pf) shell GXPF1 [53], which assumes a frozen ^{40}Ca core and valence particles restricted to the $1p$-$0f$ single-particle space. Like other high-quality semi-phenomenological interactions in the pf shell, calculated spectra using GXPF1 have good agreement with experiment (which we do not show to avoid further cluttering our figures). We also made decompositions in the same space using the monopole-modified Kuo-Brown effective interaction version KB3G [54] and the modified GXPF1 interaction, version A, [9] and found very similar results.

FIG. 3: Decomposition of wavefunctions of ^{48}Cr into components of total L (orbital angular momentum). The fill (and color) scheme are matched to the levels shown in Fig. 2, i.e., (red) solid bars (lower sub-band), (blue) dotted (upper sub-band), and (black) cross-hatched, and (green) striped, intruder levels. Here and throughout we superimpose levels which have the same I but which belong to different sub-bands.

B. Group decomposition and quasi-dynamical symmetry

Modern computers allow us to carry out large scale calculations previously unimaginable. The M-scheme dimension for ^{48,49,50}Cr in the $1p$-$0f$ valence space are 2 million, 6 million, and 14.6 million, respectively, but fully converged low-lying states can be computed in a matter of minutes on a laptop, and leadership-class configuration-interaction calculations have basis dimensions of the order of 10^{10}. This begs the question: do we really need that many numbers?

One attempt to simplify the description of nuclei is through *dynamical symmetries*, where the Casimirs of a group commute with the nuclear Hamiltonian; then the eigenstates of the Hamiltonian will also be eigenstates of the Casimirs of the group, and one can just choose a basis within a single irreducible representation (irrep) of the group [47–49], which is the smallest possible sub-

space where all group elements are block-diagonal. (The simplest, though still nontrivial, example of this would be a *J*-scheme basis, where the states have fixed total angular momentum *J* rather than *M*. *J*-scheme bases are an order of magnitude smaller than *M*-scheme bases, but because each *J*-scheme state is a linear combination of *M*-scheme states, computing matrix elements is correspondingly more difficult and the Hamiltonian matrix is significantly denser.) The most prominent choice is the group SU(3), from which rotational bands arise naturally [55, 56], or its extension the symplectic group Sp(3,R). We loosely say we decompose the wavefunctions into group irreps, although in our SU(3) and SU(4) examples we use only one Casimir operator for the decomposition, and hence technically we in those cases we are combining results from different irreps. In principle one could fully decompose into true irreps, but we chose not to, partly to avoid in using three-body Casimirs for SU(3) as well as to keep our already busy figures become less readable.

Alas, it has long been known that the nuclear force, in particular the spin-orbit [57–59] and pairing [60] components, strongly mixes SU(3). But not all is lost: while the wavefunctions are distributed or *fragmented* across many irreps, in many cases the patterns are strongly coherent and consistent across members of a band [57, 59]. This *quasi-dynamical* symmetry [61–63] helps to explain why SU(3) dynamical symmetry works well phenomenologically even though it fails microscopically.

To illuminate quasi-dynamical symmetry, we decompose a wavefunction into subspaces labeled by Casimir eigenvalues. Given a wave function $|\Psi_i\rangle$, which is an eigenstate of the nuclear many-body Hamiltonian (1), and a group Casimir $\hat{C}$ with eigenpairs

$$\hat{C}|z, \alpha\rangle = g(z)|z, \alpha\rangle \tag{2}$$

where z is a quantum number or numbers labeling subspaces of the group (for example, for SU(2) I is a quantum number and $g(I) = I(I+1)$; note that, for consistency with many past papers on backbending, we use I rather than J for nuclear angular momentum) and α labels distinct states in the subspace, that is, solutions of (2) degenerate in $g(z)$, we want to find the fraction $\mathscr{F}(z)$ of the wave function $|\Psi_i\rangle$ in the subspace labeled by z, that is,

$$\mathscr{F}(z) = \sum_{\alpha \in z} |\langle z, \alpha|\Psi_i\rangle|^2 . \tag{3}$$

Luckily, there is an efficient method to find $\mathscr{F}(z)$ using the Lanczos algorithm [59, 64] that does not require finding all states in the irrep. This method only finds the magnitude in each subspace,

39
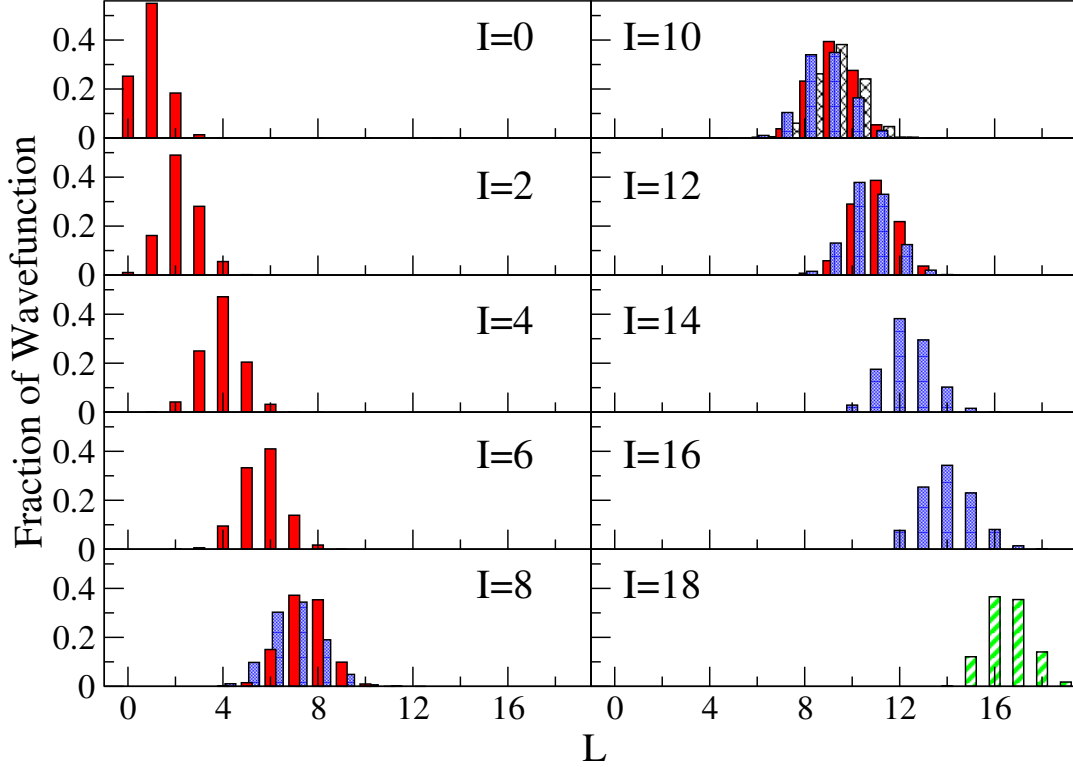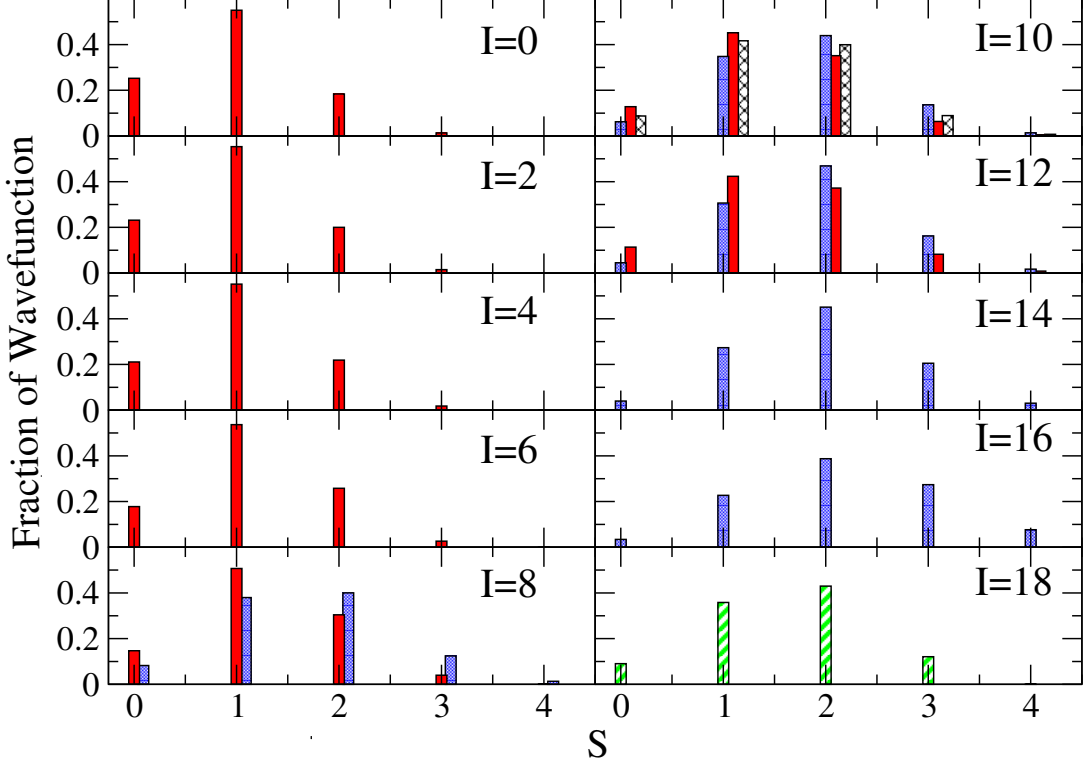
FIG. 4: Decomposition of wavefunctions of ^{48}Cr into components of total S (spin). The fill (and color) scheme are the same as in Fig. 3.

not the phase. In the next section we plot $\mathscr{F}(z)$, the fraction of the wavefunction in the subspace labeled by z, versus either z (or $g(z)$, in the case of SU(3) and SU(4), where z represents several labels) as bar graphs for states along the yrast band.

The group Casimirs we use are: total orbital angular momentum $\hat{L}^2$ labeled by L; total spin $\hat{S}^2$ labeled by S; and the two-body Casimirs of SU(3) and SU(4).

The irreps of SU(3) are labeled by the quantum numbers λ and μ via their Young tableaux [48], and which can be interpreted in terms of the standard deformation parameters β and γ (see Figure 2 in Ref. [65] or Figure 1 in Ref. [60]). We use only the two-body Casimir,

$$C_2(SU(3)) = \frac{1}{4}\left(\vec{Q}\cdot\vec{Q}+3L^2\right),\tag{4}$$

where

$$Q_m = \sqrt{\frac{4\pi}{5}}\left(\frac{r^2}{b^2}Y_{2m}(\Omega_r)+b^2p^2Y_{2m}(\Omega_p)\right),\tag{5}$$

the (dimensionless) so-called Elliott quadrupole operator, whose matrix elements are nonzero only within a major harmonic oscillator shell; here Ω_r and Ω_p refer to the standard angles θ,ϕ in spher-

ical coordinates for the position and momentum vectors, respectively. This Casimir has eigenvalues $\lambda^2 + \lambda\mu + \mu^2 + 3\lambda + 3\mu$ (in the above b is the harmonic oscillator length parameter). One could distinguish between different combinations of λ and μ by including the third-order Casimir, which is numerically more challenging. We discuss interpretation of the SU(3) decomposition in terms of deformation in Section III D.

Wigner suggested [66, 67] looking for an $SU(4)$ symmetry built upon $SU_S(2) \times SU_T(2)$, sometimes called a *supermultiplet*. The irreps of SU(4) are labeled by the quantum numbers P, P', and P'', which arise from the Young tableaux [48, 67], found by the Casimir operator

$$C_2(SU(4)) = \vec{S}^2 + \vec{T}^2 + 4\sum_{i,j}(\vec{S}_i \cdot \vec{S}_j)(\vec{T}_i \cdot \vec{T}_j) \tag{6}$$

where the sum is over particles labeled by i, j, and which has eigenvalues [48, 67],

$$P(P+4) + P'(P'+2) + (P'')^2 \tag{7}$$

In the highest weight states, $P = S$ and $P' = T$. Despite its early history, SU(4) has recently been neglected, in part because it is badly broken in nuclei, for example in the sd and pf shells [68]. It has been primarily investigated in its role in the Wigner energy [69]. Although we confirm breaking of SU(4), we also demonstrate strong quasi-dynamical symmetry.

Group decompositions of the wavefunctions are of course not experimentally observable. Prior work, however, in L- and S-decomposition comparing phenomenological and *ab initio* calculations demonstrated remarkable consistency [64].

III. RESULTS

Throughout we attempt as much as possible to use a consistent labeling scheme of levels, e.g for levels in the lower sub-band we use (red) solid circles for the excitation energies and (red) solid bars for the decomposition; for levels in the upper sub-band we use (blue) dotted triangles for excitation energies and (blue) dotted bars for decomposition; and finally for 'intruder' states, that is, levels which do not belong to either the upper or lower sub-bands, we use black 'x's and black cross-hatched bands and (green) striped circles/bars. In all of this we group together levels via quasi-dynamical symmetry, that is, by inspecting the decomposition into irreps. Using group decomposition and quasi-dynamical symmetry, we attempt to extend members of a band beyond the yrast in order to identify band crossings; we were able to do this for ^{48,50}Cr but not ^{49}Cr.

41
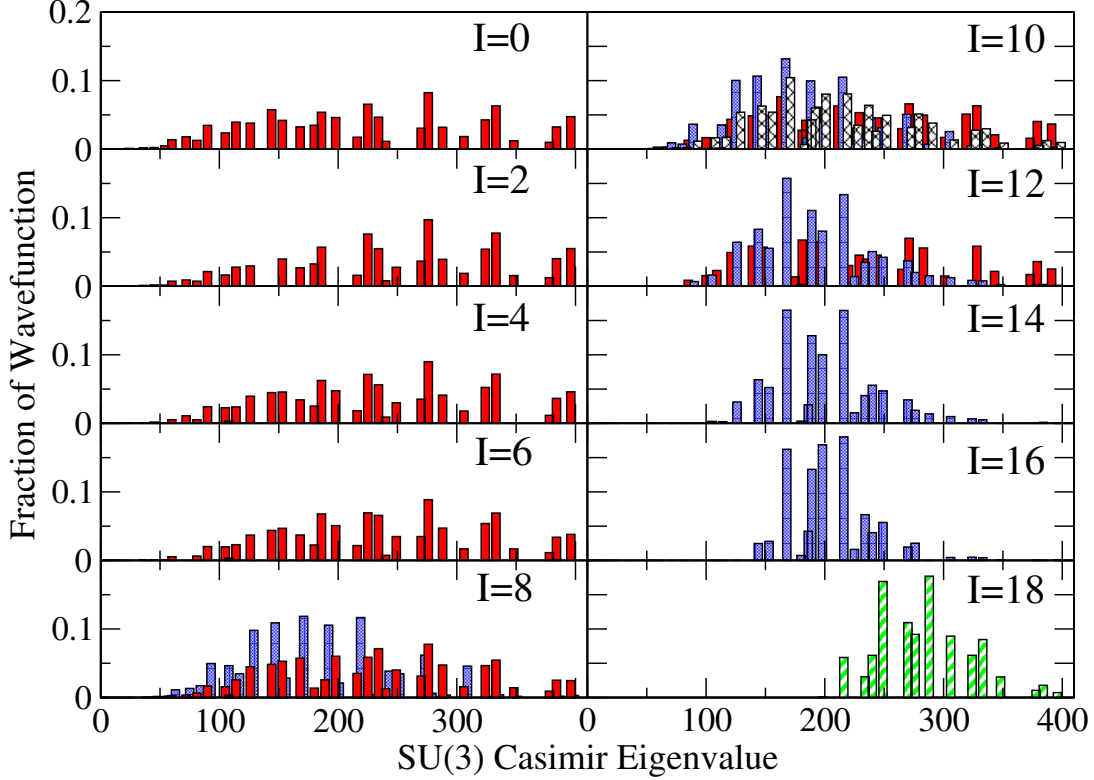
FIG. 5: Decomposition of wavefunctions of ^{48}Cr into SU(3) irreps, labeled by eigenvalues of the two-body SU(3) Casimir (see text for definition). The fill (and color) scheme are the same as in Fig. 3.

Although we attempt to give a reasonable summary of the existing literature, for purposes of comparison we emphasize those whose interpretations mostly clearly can be illuminated by our calculations, namely those which focus on shape deformations, and less so on K quantum numbers (the J_z value in the intrinsic frame) and quasi-particle excitations which, while of course relevant, are harder to connect to our group decompositions.

A. ^{48}Cr

We begin with backbending in ^{48}Cr [31, 32]. Fig. 2 shows the spectrum, spaced by $I(I+1)$ so that rotational bands are linear and easily picked out. In fact we see here and for our other two isotopes that the yrast bands are not ideal rotors but positioned between vibrational (linear in I) and rotational (quadratic in I).

Caurier *et al.* [39] compared a cranked Hartree-Fock-Bogoliubov (CHFB) calculation with

42
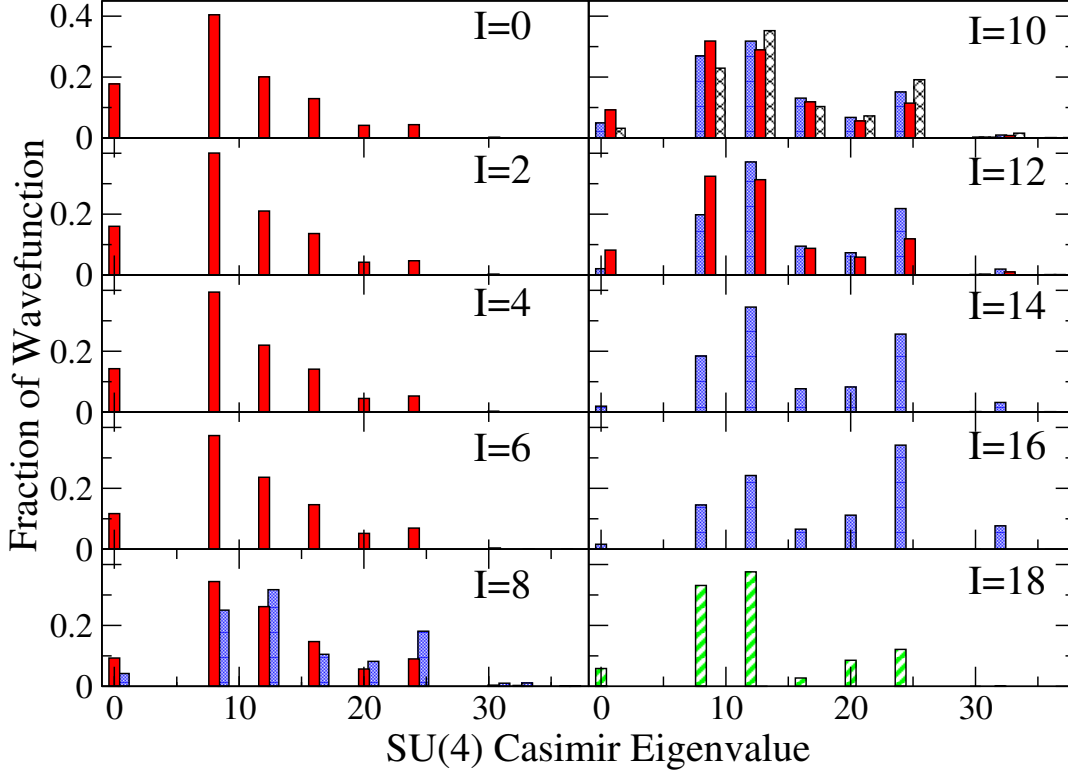
FIG. 6: Decomposition of wavefunctions of ^{48}Cr into SU(4) irreps, labeled by eigenvalues of the two-body SU(4) Casimir (see text for definition). The fill (and color) scheme are the same as in Fig. 3.

the finite range Gogny force against a full pf-shell diagonalization. Both calculations yielded similar backbending and excellent agreement in B(E2) values, quadrupole and magnetic dipole moments, and orbital occupations; the CHFB calculation showed an axially deformed rotor up to the backbend, while the yrast states after the backbend are more spherical and with the triaxiality parameter γ less well-defined. Because full space configuration-interaction (CI) calculations do not have an intrinsic frame, the deformation cannot be computed directly, but Caurier *et al.* argued that, given the good agreement between CI and CHFB in other quantities, the CHFB interpretation is likely robust.

Later calculations support this picture. A subsequent CHFB calculation [24] arrived at similar results, i.e., consistent axial deformation up to the backbending, and then rapid transition to a spherical nucleus. These authors emphasized the lack of a level crossing in the single-particle orbits, which is associated with backbending in heavier nuclides, and the importance of careful treatment of the residual interaction.

Calculations with the "projected shell model" or PSM [37], which uses a basis of deformed quasiparticle-quasihole states projected out with good angular momentum and particle number, also described the backbending of ^{48}Cr in terms of a spherical band crossing a deformed band; furthermore, they identified *two* crossings, the first around $I = 6$, where a 2-quasiparticle (qp) band crosses the ground state 0-qp band, which does not show up as backbending, and the second, around $I = 10$, where a 4-qp band crosses the 2-qp band.

Finally the hybrid "projected configuration interaction" (PCI) [44], which is similar to the projected shell model but using deformed particle-hole states, that is, explicitly number-conserving, rather than quasiparticle-quasihole state, which are then projected out to good angular momentum and the Hamiltonian diagonalized in this basis, found results similar to that of Caurier *et al.*. (Another germane difference is the PSM used a schematic interaction tuned to reproduce levels within their calculations, while the PCI uses semi-realistic shell-model interaction fitted within the full configuration space.) In particular they emphasized levels below the backbending are dominated by a single deformed intrinsic state, but not above the backbending.

Now we turn to our group decompositions for ^{48}Cr. The *L*-decompositions, Fig. 3, at first glance look like a intrinsic shape being spun up: the distribution of *L* is similar for all the yrast states, though shifted up as total angular momentum *I* increases. But there are subtleties. For example, the ground state is dominated by $L = 1$, while the states $I = 2, 4, 6, \ldots$ have their strength centering roughly around $L = I$. Above the backbend at $I \approx 10$, this shifts; now the strength centers roughly around $L \approx I - 2$.

This pattern is of course echoed in the *S* decompositions (Fig. 4): below the backbend, the decomposition is dominated by $S = 1$, with some $S = 0$ which decreases, and $S = 2$ which increases slightly, while after the backbend $S = 2$ dominates with $S = 1, 3$ subdominant. Of course, in this space the maximum *S* is 4, which means when one reaches $I = 18$ the minimum *L* is 14; this helps to explain the shifting pattern in the *L* decomposition. Nonetheless, notice that the $I = 18$ state is significantly different, particular in *S*. This is easily understood: the ground state band is predominantly $(0f_{7/2})^8$ [39] but the maximum angular momentum for that configuration is $I = 16$.

The SU(3) decompositions, Figs. 5, also show a pronounced change around the backbending. SU(3) is highly fragmented, as is well known for the pf shell [59]. After the backbend, the distribution of SU(3) is much more narrow and in fact narrows further with increasing *I*. *K*-band termination may be contributing to this evolution, with some SU(3) (λ, μ) dropping out due to

44
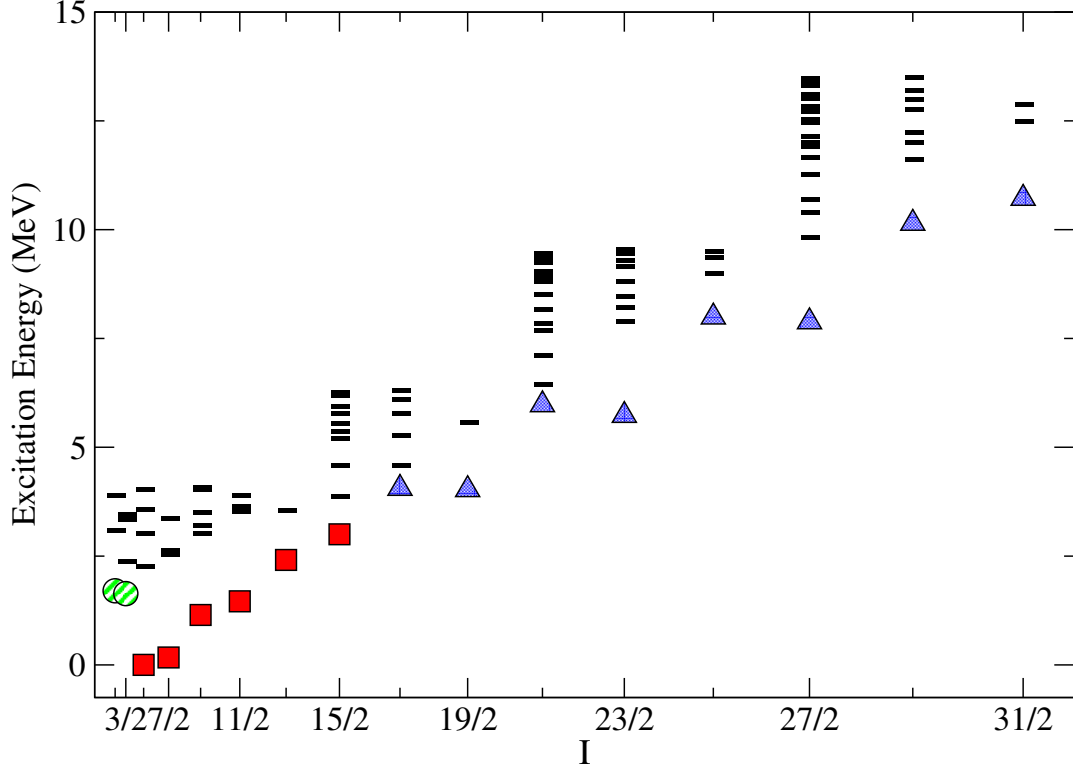
FIG. 7: Calculated spectrum of ^{49}Cr. The *x*-axis (angular momentum *I*) is scaled as $I(I+1)$ so as to emphasize rotational bands. The labeling of levels, i.e., red squares, blue triangles, and green circles, correspond to the same (initial) state as in Panel (b) in Fig. 1. Bars indicate levels found in our calculation but which we do not decompose.

their maximum possible *L* values. On the other hand, the *L*- and *S* decompositions do not change much within the uppper sub-band, until one reaches the termination of the $(0f_{7/2})^8$ configuration at $I = 16$.

Previous work on SU(4) only showed its fragmentation [68], while we appear the first to demonstrate quasi-dynamical symmetry in SU(4) in the *pf* shell, as in Fig. 6. The SU(4) decomposition also changes dramatically at the backbend, although the spread does not evolve as it does so for SU(3). Again the abrupt shifts at $I = 18$ is easily interpreted as the termination of the $(0f_{7/2})^8$ configuration band at $I = 16$. Interestingly, the change in the SU(4) decomposition at the backbend is most pronounced for ^{48}Cr than for our other two nuclides. This is suggestive of studies investigating the relative role of isovector and isoscalar pairing in $N = Z$ and $N \neq Z$ nuclides, as in [69].

By using the decompositions we were able to identify levels which are not part of the yrast

band but which do appear to be continuations of the component sub-bands. For example, we were able to trace the continuation of the lower sub-band up through $I = 12$, as well as trace the upper sub-band down to $I = 8$. Futhermore we can see the actually yrast level at $I = 10$, marked by an 'x' in Fig. 2 and cross-hatched bars in Figs. 3-6 belongs to neither the lower nor the upper sub-bands.

B. ^{49}Cr

Fig. 7 shows the spectrum of ^{49}Cr spaced by $I(I+1)$. The yrast band of ^{49}Cr has been measured up to $31/2^-$ [33, 34], which is the highest angular momentum we calculate. It was previously calculated in the full pf model space using shell-model CI [43], where the authors explicated the results in terms of Nilsson diagrams and detailed effects of the residual interaction; other calculations emphasize the role of K-bands and quasi-particle excitations of the intrinsic state [38, 45, 46].

As with all three of our nuclides, the L decompositions, Fig. 8, increase steadily with I; similar to what we saw with ^{48}Cr, below the the L-decompositions for each angular momentum I centers around $L \approx I - 1/2$, while in the upper sub-band it centers around $L \approx I - 3/2$.

The spin decompositions, Fig. 9 show strong (but distinct) quasi-dynamical symmetry below and above the backbend, and could be approximated by taking the spin decompositions of ^{48}Cr and shifting up by 1/2 unit of angular momentum (the L-decomposition also strongly parallel that of ^{48}Cr): below the backbend the yrast band is dominated by $S = 1/2, 3/2$, while above the backbend $S = 3/2, 5/2$ dominate.

Also like ^{48}Cr, the SU(3) decomposition of ^{49}Cr, Fig. 10, is relatively coherent below the backbend, while above the backbend the distribution becomes narrower and has more pronounced evolution.

Fig. 11 shows strong quasi-dynamical symmetry in SU(4), especially in the lower sub-band, but with significant coherence in the upper band as well; while there is a definite change across the backbend, it is not as dramatic as for ^{48}Cr. Here we were not able to identify continuations of the sub-bands beyond their locations on the yrast band.

In our figures we include the low-lying $I = 1/2, 3/2$ levels which, though part of the yrast band, are not the yrast band heads; in the S and SU(4) decompositions they clearly are grouped with the rest of the low-lying yrast levels, but they have nontrivial differences in the other decompositions,
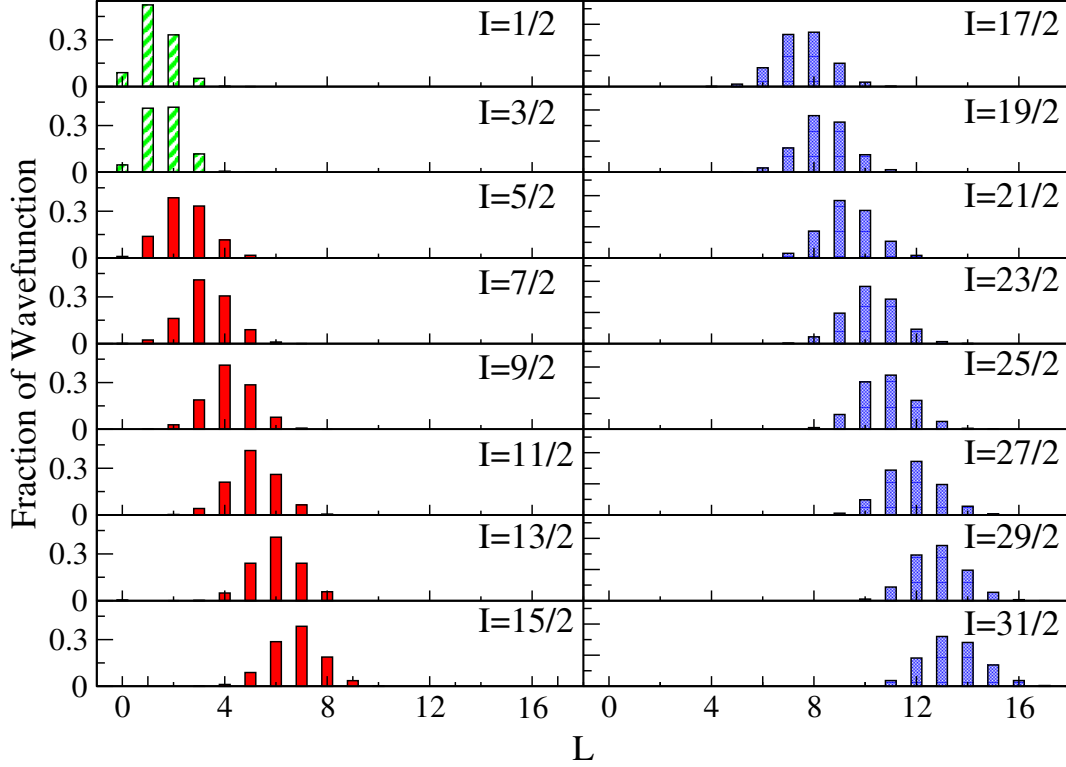
FIG. 8: Decomposition of wavefunctions of ^{49}Cr into components of total L (orbital angular momentum). Much like Fig. 3, the fill (and color) scheme are matched to the levels shown in Fig. 7, i.e., (red) solid bars (lower sub-band), (blue) dotted (upper sub-band), and (green) striped, the lowest $I = 1/2, 3/2$ which technically are not part of the yrast line.

most markedly in SU(3).

C. ^{50}Cr

The yrast band of ^{50}Cr has been measured up to $I^\pi = 18^+$ [34–36], as shown in Fig. 12, with backbending seen around $I \approx 10$ and a second backbending around $I \approx 16$ which is easily interpreted as the terminus of levels generated within the $(0f_{7/2})^{10}$ configuration. The origin of the change at the backbending is somewhat unclear within CI calculations; Martínez-Pinedo *et al* [42] interpret it as a shift from strongly prolate to weakly oblate, similar to what is seen in ^{48}Cr, yet Zamick *et al*, looking at the sign of the quadrupole moments in just the $(0f_{7/2})^{10}$ configuration space [41], argue instead the upper sub-band could belong to a high-K prolate band.

Similar to the work on ^{48}Cr [39], calculations using the configuration-interaction (CI) shell
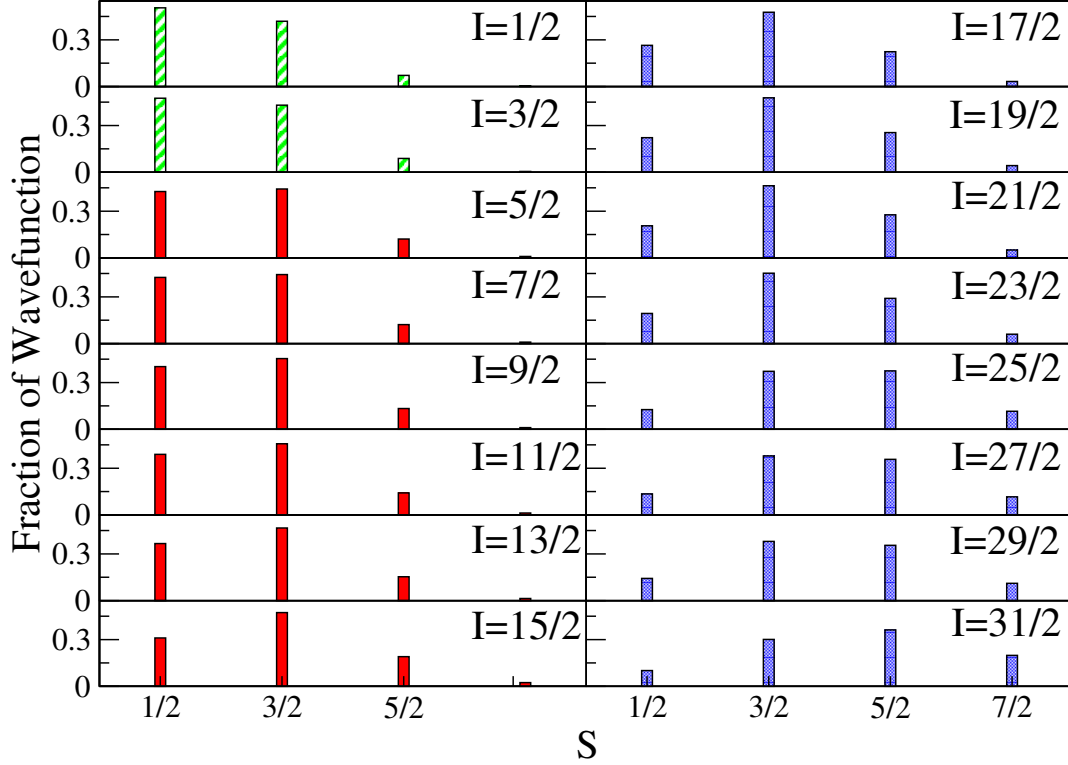
FIG. 9: Decomposition of wavefunctions of ^{49}Cr into components of total S (spin). The fill (and color) scheme are the same as in Fig. 8.

model were compared directly with cranked Hartree-Fock-Bogoliubov calculations [42], and with similar results: both CI and CHFB showed backbending at $I \approx 10$ and $I \approx 16$; the latter is where pure $(0f_{7/2})^{10}$ configurations must terminate. In particular they find ^{50}Cr to be axially symmetric and prolate below $I \approx 10$, afterwhich it becomes oblate and weakly triaxial, until it reaches $I \approx 16$ where, again at the termination of the $(0f_{7/2})^{10}$ configuration it becomes strongly triaxial.

While the decomposition in L, shown in Fig. 13, shows significant shifts at the two backbending points, the decompositions in S, Fig. 14, and SU(4), Fig. 16, are more subtle than for our other two nuclides: in the run-up to the backbend, at $I = 6, 8$, the decompositions of both sub-bands are nearly identical, but as I increases up to and past the backbend at $I = 12$, the decompositions of the upper sub-band shows a stronger evolution. Like the other nuclides, in the SU(3) decomposition, Fig. 15, we see strong quasi-dynamical symmetry in the lower sub-band, with strong changes at the two backbends, and the fragmentation becoming more narrow.
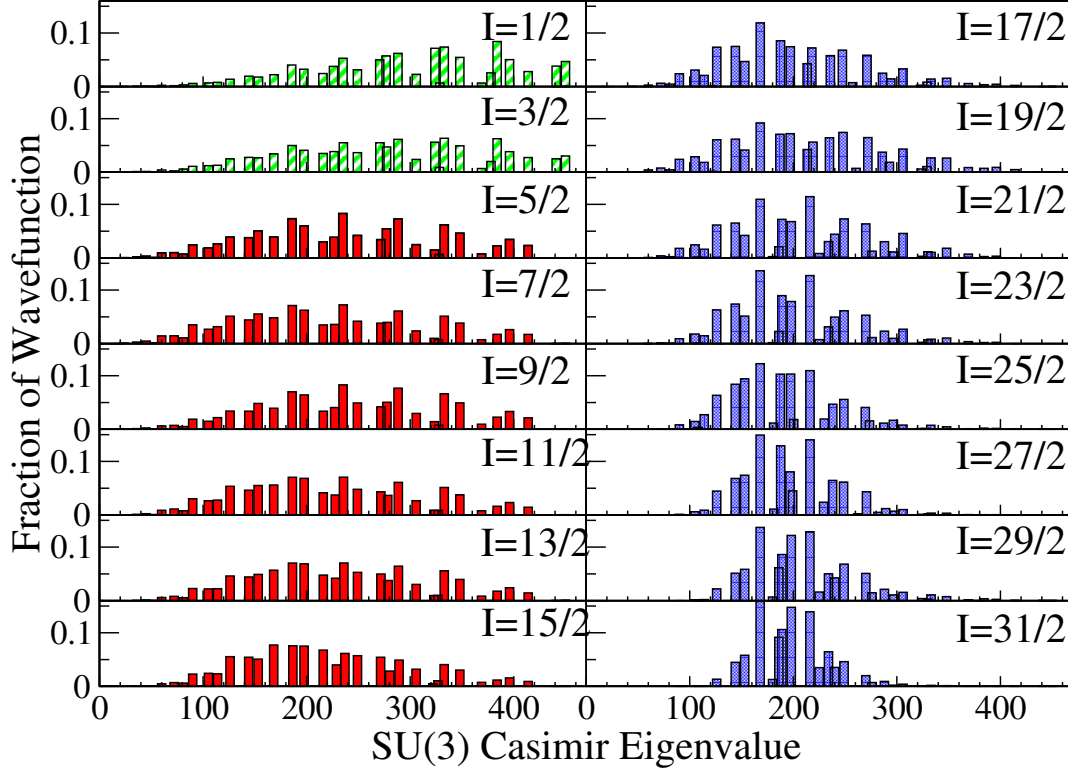
FIG. 10: Decomposition of wavefunctions of ^{49}Cr into SU(3) irreps. See text for the definition of the SU(3) Casimir. The fill (and color) scheme are the same as in Fig. 8.

D.   SU(3) and deformations

For a given state wholly in an SU(3) irrep labeled by (λ, μ) one can map it to a deformed shape and determine its deformation parameters β and γ; in particular, the value of the two-body SU(3) Casimir is proportional to β^2 [65]. This has been used in prior work to examine SU(3) breaking by the pairing and spin-orbit forces [58, 60]. The broad fragmentations we see in SU(3) is similar to the broad distributions of β and γ values in the presence of strong spin-orbit splitting in Figs. 2 and 3 of [58].

It is therefore tempting to interpret our SU(3) decompositions as telling us something about deformation. By eye one can see, and we confirmed in detail, the expectation value of $C_2(SU(3))$ does not change much along the yrast line for each of our nuclides; by the above mapping this would suggest the average value of β^2 also remains near constant. This, however, contradicts prior work using mean-field frameworks suggesting ^{48,49,50}Cr are all strongly prolate, axially symmetric rotors below the backbend, while above the backbend they becomes nearly spherical and are less
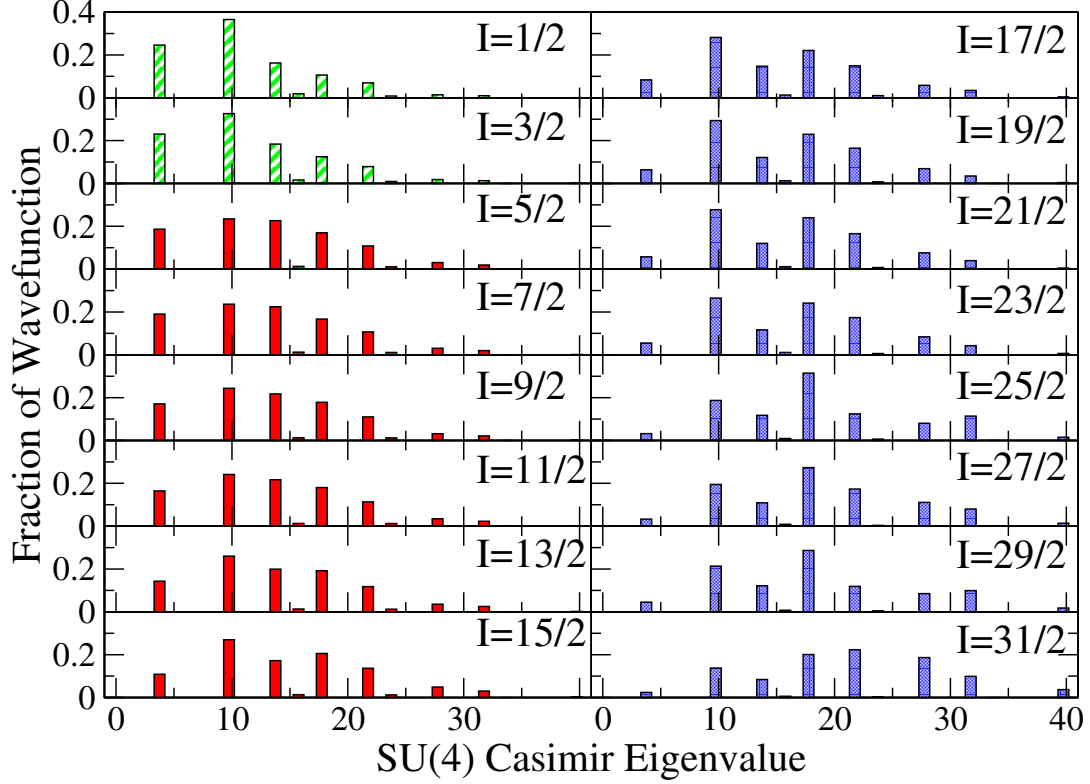
FIG. 11: Decomposition of wavefunctions of ^{49}Cr into SU(4) irreps. See text for the definition of the SU(4) Casimir. The fill (and color) scheme are the same as in Fig. 8.

well-interpreted in terms of a single intrinsic shape [24, 39, 42, 44, 46]. (Although we do not show it, we confirmed this behavior with a separate Hartree-Fock code using shell-model interactions.)

It is important to note that a deformed Slater determinant does not necessarily correspond to a single SU(3) irrep. Rather, it can be fragmented across many group irreps, as previously demonstrated in [70], where a projected Hartree-Fock state had a much stronger overlap with the full configuration-interaction ground state wavefunction than the highest-weight SU(3) state, driven predominantly by the single-particle spin-orbit force.

We can provide a class of simple examples which show the mapping of SU(3) labels (λ, μ) to deformation can conflict with a simple mean-field picture. Consider a state which consists of a filled single-j shell, for example, ^{48}Ca where one fills the $0f_{7/2}$ shell with neutrons. This is a single Slater determinant and is a manifestly spherical shape: the expectation value of the quadrupole tensor vanishes. Yet if one decomposes it using the SU(3) two-body Casimir, it has only a 1% fraction in the spherical $(\lambda, \mu) = (0, 0)$ irrep; the rest of the wavefunction is broadly spread across
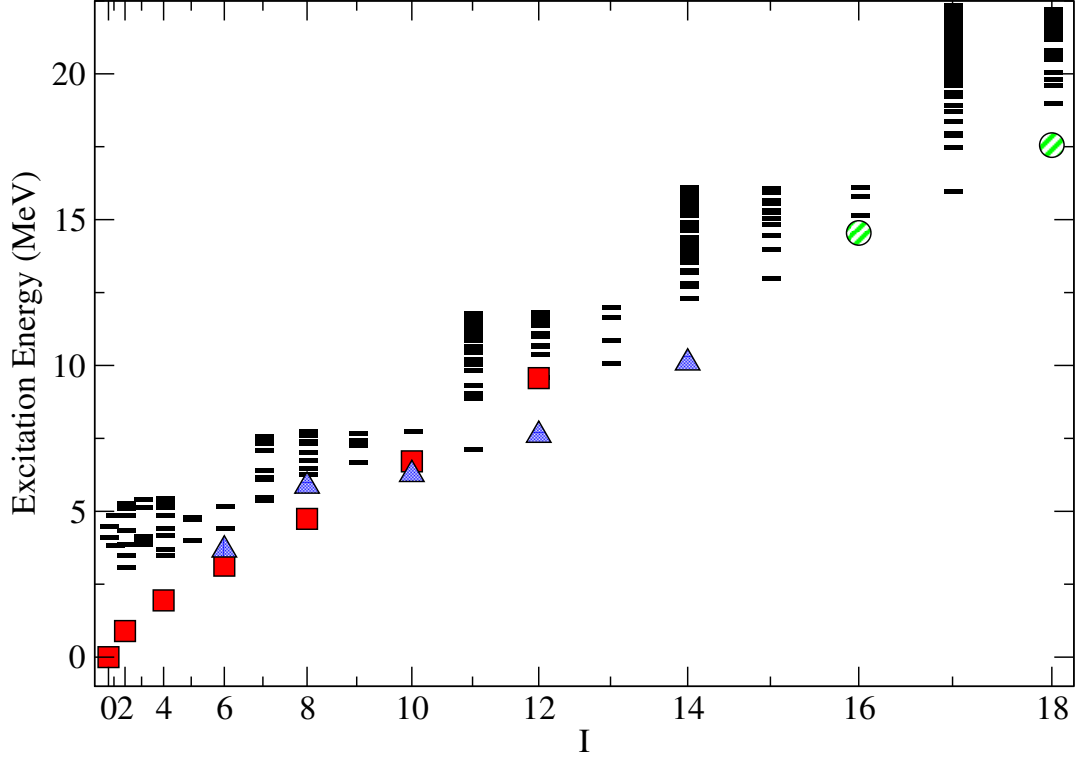
FIG. 12: Calculated spectrum of ^{50}Cr. The *x*-axis (angular momentum *I*) is scaled as $I(I+1)$ so as to emphasize rotational bands. The labeling of levels, i.e., (red) squares, (blue) triangles, and (green) circles, correspond to the same (initial) state as in Panel (a) of Fig. 1. Bars indicate levels found in our calculation but which we do not decompose.

many SU(3) irreps. This result is not unique to ^{48}Ca, but occurs whenever one fills a *j*-shell but not its spin-orbit partner. The fact that one has large SU(3) mixing is not surprising, given the spin-orbit splitting, but it also suggests a picture of deformation can depend strongly upon whether determined from a mean-field solution or from an SU(3) decomposition.

IV.   CONCLUSIONS AND ACKNOWLEDGEMENTS

In order to illuminate backbending in chromium isotopes, we carried out group decomposition of shell model CI wavefunctions, using total orbital angular momentum *L*, total spin *S*, and the two-body Casimir operators of SU(3) and SU(4). We saw strong quasi-dynamical symmetry in all cases, often with a significant shift in the fragmentation as one crosses from the lower to the upper sub-band. Above the backbend the SU(3) distribution show the largest evolution with increasing *I*,
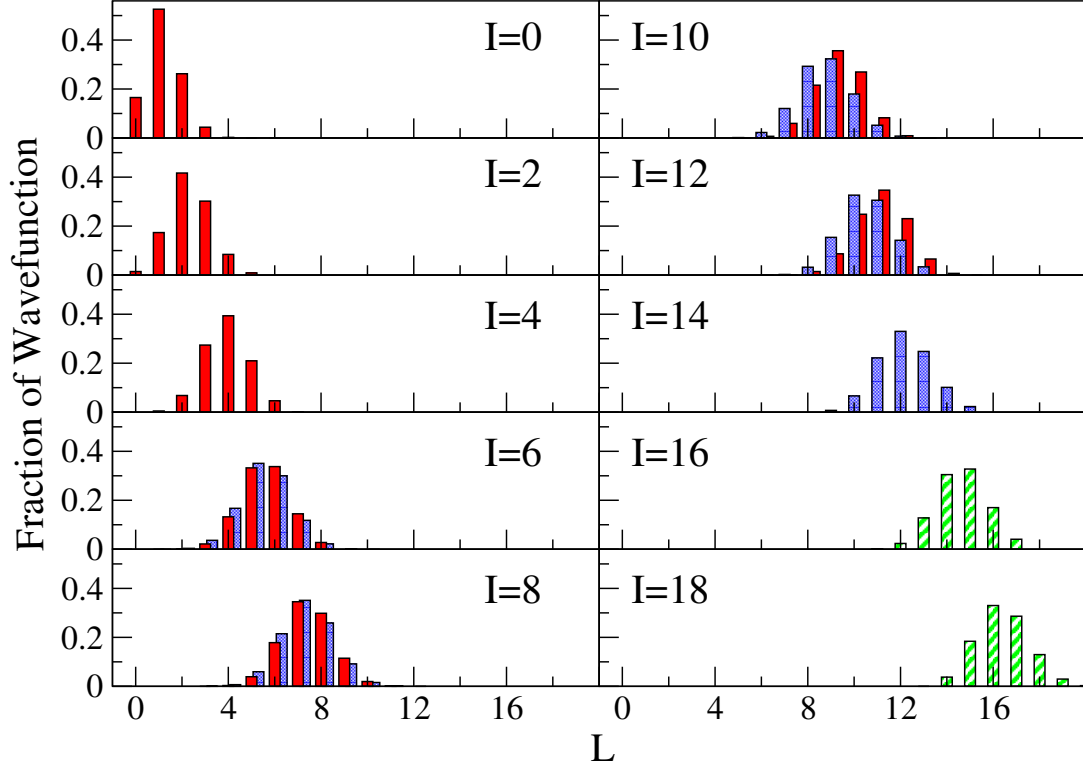
FIG. 13: Decomposition of wavefunctions of ^{50}Cr into components of total L (orbital angular momentum). Decomposition of wavefunctions of ^{50}Cr into components of total L (orbital angular momentum). Much like Fig. 3, the fill (and color) scheme are matched to the levels shown in Fig. 12, i.e., (red) solid bars (lower sub-band), (blue) dotted (upper sub-band), and (green) striped ('intruder,' that is, outside of the $(0f_{7/2})^{10}$ configuration space). Here and throughout we superimpose levels which have the same I but which belong to different sub-bands.

a narrowing of the distribution but with a nearly constant average. On one hand large expectation values of the SU(3) two-body Casimir eigenvalues suggest persistent large deformation, but mean-field calculations consistently depict the yrast states at high I have decreasing deformation. We note this clash of deformation pictures, that is, mean-field versus SU(3), can be found even in the very simple example of a simple spherical Slater determinant, a filled j-shell, which also has a broad distribution across many deformed SU(3) irreps.

In contrast, spin S and SU(4) show less evolution in the sub-bands, both below and above the backbending. SU(4) shows the most pronounced shift in decomposition at the backbend in ^{48}Cr, much less so in our other two nuclides; nonetheless, we have demonstrated pervasive SU(4) quasi-dynamical symmetry in the pf shell. Overall the L decomposition simply shows a steady and
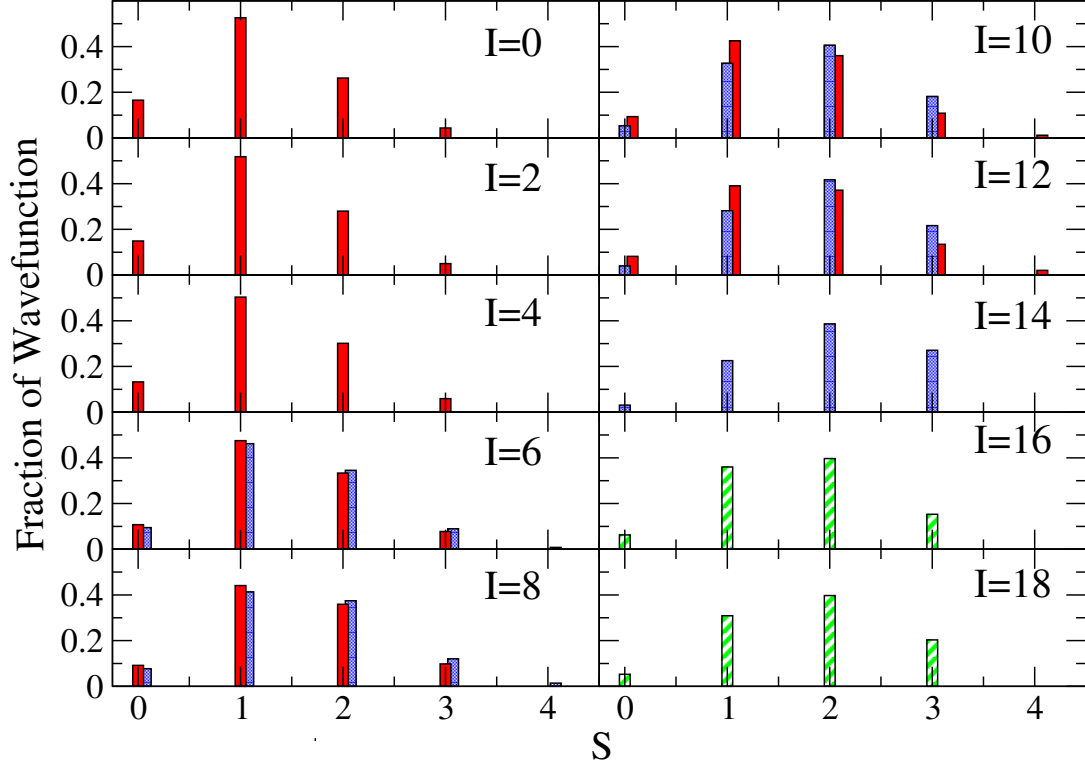
FIG. 14: Decomposition of wavefunctions of ^{50}Cr into components of total S (spin). Fill (and color) scheme same as that of Fig. 13.

coherent increase in angular momentum.

Of course, the pf shell space is limited and the GXPF1 interaction is phenomenological and heavily renormalized relative to the 'real' nuclear force. While there has been work decomposing *ab initio* wavefunction for very light nuclei into SU(3) irreps, [71], quasi-dynamical symmetry has not been deeply investigated such calculations. We only note that one previous investigation, in the L and S decomposition only [64] in p-shell nuclei, showed remarkable congruence between results from phenomenological and *ab initio* interactions.

While it would be interesting to apply these same analyses to heavier nuclei with backbending, the fact that tractable model spaces for such nuclei general exclude spin-orbit partners makes exact decomposition impossible. One could consider pseudospin, psuedo-SU(3), and other approximate symmetries, but this we also leave to future work.
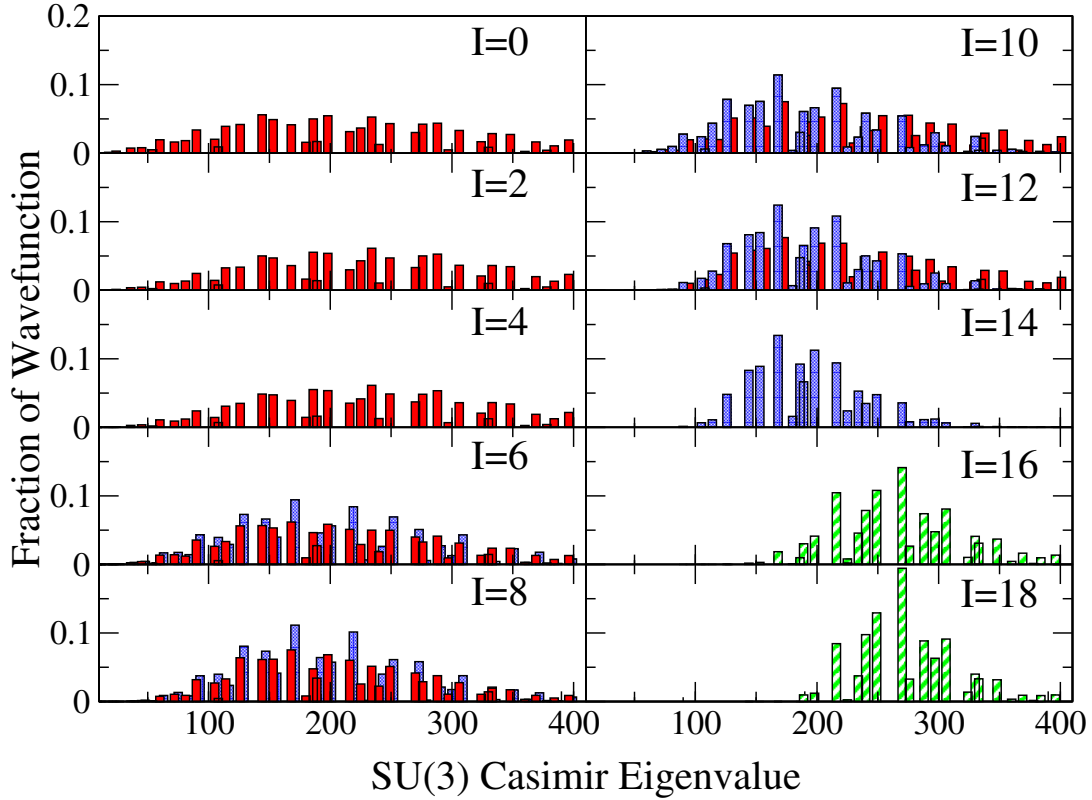
FIG. 15: Decomposition of wavefunctions of ^{50}Cr into SU(3) irreps. Fill (and color) scheme same as that of Fig. 13.

Chapter 2, in full, is a reprint of the material as it appears in Physical Review C, 2017. Herrera Raul; Johnson, Calvin. I, Raul A. Herera, was the primary investigator and author of this paper.
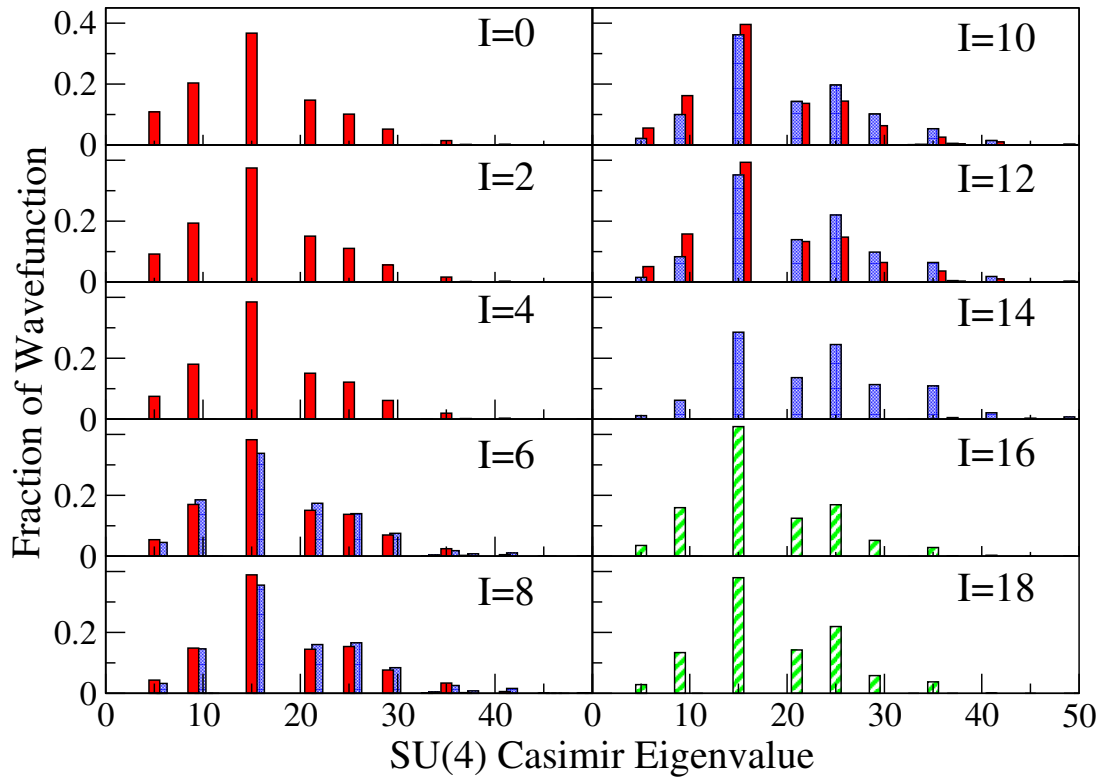
FIG. 16: Decomposition of wavefunctions of ^{50}Cr into SU(4) irreps. Fill (and color) scheme same as that of Fig. 13.

Chapter 3

Localized Brink-Axel in Weak Rates of Astrophysical PF Shell Nuclei

3.1 Introduction

Weak nuclear transitions strengths from highly excited states are needed for accurate modeling of astrophysical properties, but difficult to obtain either from experiment or theory. For experiment, it is rare to find weak decay rates from the first excited state let alone higher excited states. For theory, using computational methods one finds two issues. First, depending on the type of shell, the degeneracy of those shells also increases as $(2J + 1)$, where for example p and f shells have more states than s and d shells. Further, the basis dimension of the shell model space increases in combinatorial fashion as one fills up single particle states within a specific major shell with nucleons. Second, the number of Lanczos iterations required to converge more excited states increases dramatically. Both of these factors require more and more processors, time and memory, up to the point of necessitating supercomputers. However, as I will explain, even given the most powerful modern supercomputers, the full computation of rates for heavier elements in the pf-shell and beyond remain intractable.

In the foundational work of Fuller, Fowler and Newman (FFN) [17], stellar weak rates were computed for mass number $A = 17 - 60$ for grids in temperature and density appropriate to pre-collapse massive stars. To compute the parent ground state they used the Independent Particle Model, and then applied the Brink-Axel hypothesis to approximate distributions for Gamow-Teller (GT) strength functions, as described in equation 1.33, coming from highly excited states. Later in 1994, Oda et al. [72] updated the sd-shell nuclei, $A = 17 - 39$ and an ^{16}O core, while in 2001 Langanke and Martinez-Pinedo (LMP) [73] updated rates for the pf-shell, $A = 45 - 65$ and a frozen ^{40}Ca core. The primary difference between FFN and the updates by Oda et al. and LMP was the use of large scale shell model calculations. Specifically, in the work directly preceding LMP by Caurier, Langanke and Martinez-Pinedo, (CLMP) [74], the authors sought to improve over the independent particle model approach of FFN by using the interacting shell model via the KB3 interaction of Poves and Zuker [75]. CLMP provided evidence that the KB3 interaction more accurately predict the placement of the Gamow-Teller centroid than the FFN model. Also, where FFN puts all the GT strength at one place in the daughter spectrum, the KB3 interaction models the fragmented distribution of GT transition from an initial parent state to many final daughter states, a consequence of SU(4) symmetry breaking.

Even more than 20 years ago, Oda et al. were able to compute at least 100 eigenstates in sd-shell parent nuclei, where they could capture virtually all of the thermal weak transition strength. These rates were appropriate for for the oxygen, neon, and magnesium burning stars of intermediate mass stars below 10 solar masses. However, for massive stars around 10 solar masses and higher, the pf-shell transitions are necessary, but at the time computing highly excited states for these nuclei proved difficult. LMP did an expanded sweep of the pf-shell to heavier nuclei over FFN, but only computed states 4 to 12 parent eigenstates, which limited excitation energy to 1 MeV for odd-A and odd-odd nuclei, and limited to 2 MeV for even-even nuclei. However, in LMP, as in FFN, this was supplemented by the Brink-Axel Hypothesis for the form of transition strength spectra, which will be explained below, and so-called *back resonance* contributions

coming from the reverse transition in low lying daughter states. An examination of the validity of the Brink-Axel hypothesis in sd-shell nuclei was performed by Misch, Fuller and Brown [18], where they were easily able to obtain parent states of up 28 MeV.

Today's desktop computers are easily able to obtain many hundreds of eigenpairs for Hamiltonians in the sd-shell after many thousands of Lanczos iterations. In the M-scheme basis used the sd-shell nuclei can have basis dimensions at most in the tens of thousands (^{28}Si has 90 thousand states), so a computer with gigabytes of memory more than suffices to hold such vectors and associated matrix elements. But in the pf-shell we get many orders of magnitude higher, where for example ^{52}Fe has 100 million basis states [7]. For this work I use the large scale shell model code BIGSTICK [7][15], which has parallel computing capabilities that allows for the computation of spectra and transition rates of pf-shell nuclei with especially large basis dimension by taking full advantage of the resources of supercomputing facilities.

In this work, I explore the limits of the Brink-Axel hypothesis applying it to several Gamow-Teller transitions in the iron region.

$$^{53}\text{Fe} \rightarrow {}^{53}\text{Mn}$$
$$^{55}\text{Fe} \rightarrow {}^{55}\text{Mn}$$
$$^{55}\text{Cr} \rightarrow {}^{55}\text{Mn} \tag{3.1}$$
$$^{56}\text{Fe} \rightarrow {}^{56}\text{Mn}$$
$$^{57}\text{Co} \rightarrow {}^{57}\text{Fe},$$

where I also computed thermal weak rates for the last transition $^{57}\text{Co} \rightarrow {}^{57}\text{Fe}$ at finite temperature and density suitable to massive star core conditions preceding collapse. I find very good agreement with LMP thermal Gamow-Teller rates through most of the density and temperature range up to a temperature of 10^{10} K. But beyond this temperature, there is a sudden uptick in the rates and their growth that could have significant astrophysical implications. It is found that within certain

energy windows strength distributions from neighboring parent states behave more and more similarly at higher energies. Via this principle, I devise and apply a method to obtain transitions strengths for highly excited states that are semi-converged, which can be directly applied in thermal Gamow-Teller (GT) transition rate computations in massive stellar cores.

3.2   Methods

I chose an updated shell model residual interaction in the pf-shell developed more recently in Japan, GXPF1A [9], which have smaller and more uniform deviations in lowing lying excitation energies compared to the classic KB3 family interactions [75] [54]. Also, the GXPF1 family of pf-shell residual interactions have been shown to follow more closely experimental Gamow-Teller distributions in terms of the location of resonance peaks and fragmentation of the distribution [53]. For the transition, ^{57}Co $\rightarrow$ ^{57}Fe, I use initial excited parent states going up to 60 MeV, which requires the use of the significant memory and processing capability of supercomputers for the heaviest nuclei. What is different in these computations is that I include many more initial states in the parent compared to LMP, specifically from 100-200 states, where the spectrum is converged from 4 MeV up to 10 MeV and beyond depending on the parent nucleus. As in Oda et. al. for most temperatures and densities this suffices to converge most of the thermal Gamow-Teller strength. But for temperatures above 10^{10} K it becomes necessary to use more excited states and for this I turn to the Brink-Axel hypothesis describing a sort of translation symmetry in parent excitation energy of strength function distributions. In fact, the primary focus of this chapter is to provide evidence for a modified Brink-Axel hypothesis in the pf-shell, which was first analyzed in detail by Misch, Fuller, and Brown [18] for the sd-shell. Based on this evidence, I propose a new prescription for the calculation of thermal transition rates from strength functions.

The Brink-Axel hypothesis is an approximation stating that excited state strength functions have the same distribution to daughter states as the ground state distribution, except that the

centroid is shifted up. Specifically, in the strength function defined in equation 1.33 I use the Gamow-Teller operator:

$$S_{GT}(E_i, E_{tr}) = \sum_f \delta(E_{tr} - E_f + E_i)B_{if}(GT), \tag{3.2}$$

where E_{tr} is the transition energy. The Brink-Axel hypothesis says that the strength function above is independent of the initial state, i, and only depends on the difference $E_{tr} = E_f - E_i$. Strong evidence exists for electromagnetic excitations [19]. However, the hypothesis is known to fail in systematic ways, especially as one goes up in the excited state energy spectrum [18][19]. I present computational evidence for a Localized Brink-Axel statement (LBAS) in Gamow-Teller transitions that are relevant in astrophysical applications, specifically the PF shell, where *localized* means that strength functions are indeed very similar within small windows of parent excitation energy.

In section 3.3, I demonstrate the Brink-Axel hypothesis for different in initial parent nuclei for electron capture/positron decay (GT^-) type transitions. Then in section 3.4, I show how this principle holds in a more restricted sense, that is, it breaks down globally but survives locally for many different parent nuclides and parent excitation energies, including electron capture/positron decay (GT^+) type transitions as well. Using high energy initial parent states that are not fully converged, I can probe higher in the energy spectrum than usually possible, and will allow the full computation of high temperature stellar rates beyond 10^9 K. Thus finally, in section 3.5 I apply these semi-converged excited states to the computation of such thermal rates.

There are currently two approaches used to compute transition strengths as follows. The first is computing individual transition strengths between converged states. But because both initial and final states must be converged, this is restricted to the low energies or small model

spaces, such as, the sd shell. This method uses one-body density matrices:

$$\rho_{K,T}^{fi}(ab) = \sqrt{\frac{1}{(2K+1)(2T+1)}} \sum_{ab} \langle \psi_f || [\hat{c}_a^\dagger \otimes \tilde{c}_b]_{K,T} || \psi_i \rangle, \tag{3.3}$$

where $[\hat{c}_a^\dagger \otimes \tilde{c}_b]_{K,T}$ is a tensor product of creation/annihilation operators coupled to specific values of angular momentum K, and isospin T. a and b are single particle states. Also, $\tilde{c}_b = (-1)^{j+m}c_b$ is an annihilation operator for time-reversed single particle state b, where j and m are the angular momentum quantum numbers for this specific state. To obtain the doubly reduced matrix element of an transition operator, $V_{K,T}$, which is necessary for a transition strength, one computes:

$$\langle \psi_f ||| V_{K,T} ||| \psi_i \rangle = \sum_{ab} \rho_{K,T}^{fi}(ab) \langle a ||| V_{K,T} ||| b \rangle, \tag{3.4}$$

which relates to the reduced transition probability, $B(GT)$ from equation as in equation 1.32 with $J = K$ and $V = GT$. This method has the limitation that one must compute a large number of eigenstates for both the parent and the daughter, which limits how high one can go in the excitation spectrum. However, it is a useful check against the results of the strength function method, which I discuss next.

The second approach to obtaining transition rates is by computing strength functions, as in equation 1.33. These distributions are produced from the modified Lanczos algorithm described in section 1.3.3 that starts from a single converged initial parent state and results in the transition strength function to many final states as a function of daughter energy. Because strength function calculations require converged initial states, then this approach is still limited to low excitation energy when the basis dimension of the parent nucleus is especially large, where in the pf-shell eigenstates up to 5-10 MeV excitation energy are typical, even after thousands of iterations. However, once a parent state is obtained it takes relatively few iterations to converge a good distribution to final states compared to what is needed for converging eigenstates. For example, it could take a few thousand Lanczos iterations to converge 150 eigenstates, whereas
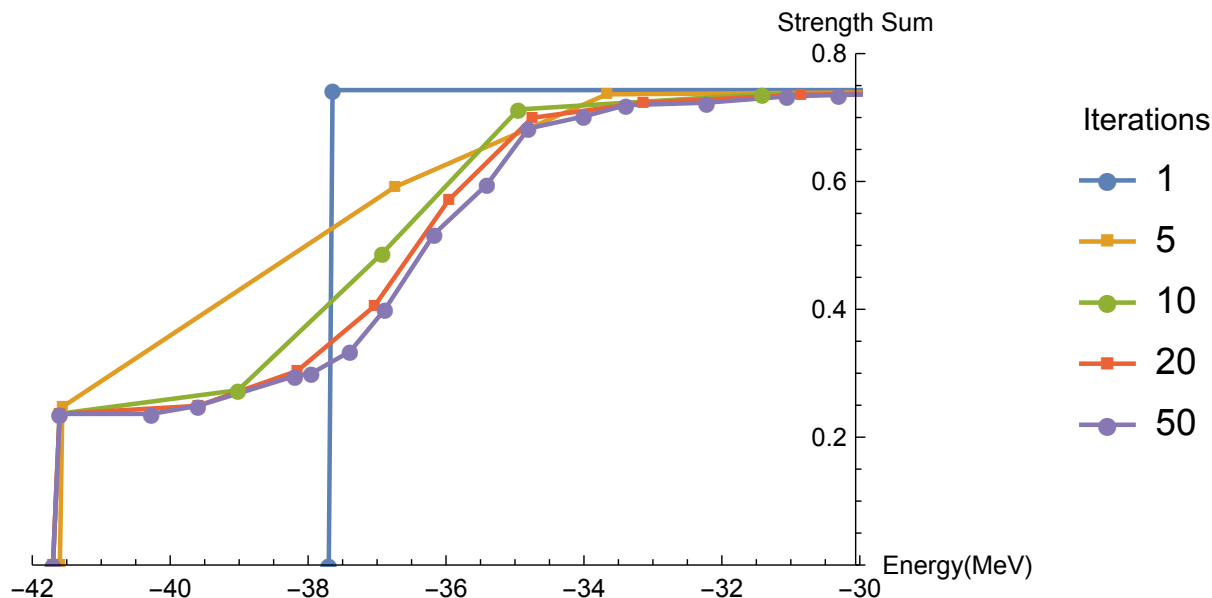
Figure 3.1: Convergence of the running sum of the strength function for the transition $^{44}\text{Ti} \rightarrow$ ^{44}V as a function of daughter energy. The points are the data, and the lines are only visual aids.

in computing strength functions LMP ran 33 iterations, whereas I ran 100 iterations. Thus it takes 1-2 orders of magnitude less computational resources to obtain decent strength function distributions compared to computing eigenpairs. Figure 3.1 gives an example of strength function convergence.

In this work, I develop and apply a third method. I start from semi-converged initial parent states whose variance in energy expectation value is small. This allowed me to sample the parent energy spectrum up to whatever is necessary to converge the thermal B(GT) transition rates. To reduce the energy variance of a semi-converged state, a targeted thick-restart Lanczos algorithm is used [15], which targets a specific energy window of the Hamiltonian. The algorithm localizes states in energy by running the Lanczos algorithm up to a maximum number of iterations, and then removes excess Lanczos vectors and restarts the filtration process a desired number of times. But it remains to be examined how well neighboring states in an excitation energy window resemble each other.

3.3 Gamow-Teller Transition Strengths and Brink-Axel

Before computing thermal rates in stellar environments, one first needs the reduced transition probabilities, $B(GT)$, which are proportional to the square of the transition matrix elements. Therefore I start with some examples of Gamow-Teller transition strengths, B(GT), as functions of transition energy. The transition energy is related to the Q-value:

$$E_{tr} = E_f^{theory} - E_i^{theory} = Q_{if} + constant = Q_0 + E_f - E_i + constant, \tag{3.5}$$

and is a measure of the available energy for various processes in the reaction, such as, the excitation energy or kinetic energy of the electrons, neutrinos or the nuclei. Here the Q-value, $Q_0 = m_{re} - m_{pr}$, is the difference in mass of the reactants and products in their ground states, E_i is the excitation energy relative to the ground state of the parent nucleus, and finally E_f is the excitation energy relative the ground state of the daughter nucleus. However, the transition energy I use in the Brink-Axel graphs will be shifted by a constant because I use the theoretical initial parent and final daughter energies, which may not exactly agree on the masses nor include the electron/positron mass. For the thermal rates, I use Q_0 as provided by experimental masses.

Notice in Figure 3.2 I show a sample of the four of the five different transitions mentioned above (GT^- type), where the strength functions all have initial parents states of around 4.5 MeV excitation energy. Here one sees the generalized Brink-Axel hypothesis holding, in that for each transition the two different distributions in each graph look very similar to each other. There is an apparent upward shift in the resonance peak as the mass number increases for the iron to manganese transitions, and one might wonder if this is a general trend. This is in contrast to the bottom graph, which has two transition strength functions for $^{57}Co \rightarrow {}^{57}Fe$ with the peak instead at a lower point in the spectrum. However, one drawback of strength functions is that these are a collection of delta function spikes with highly varying distances between them, which further move around as the Lanczos iterations proceed. Thus, the true location of a giant resonance,
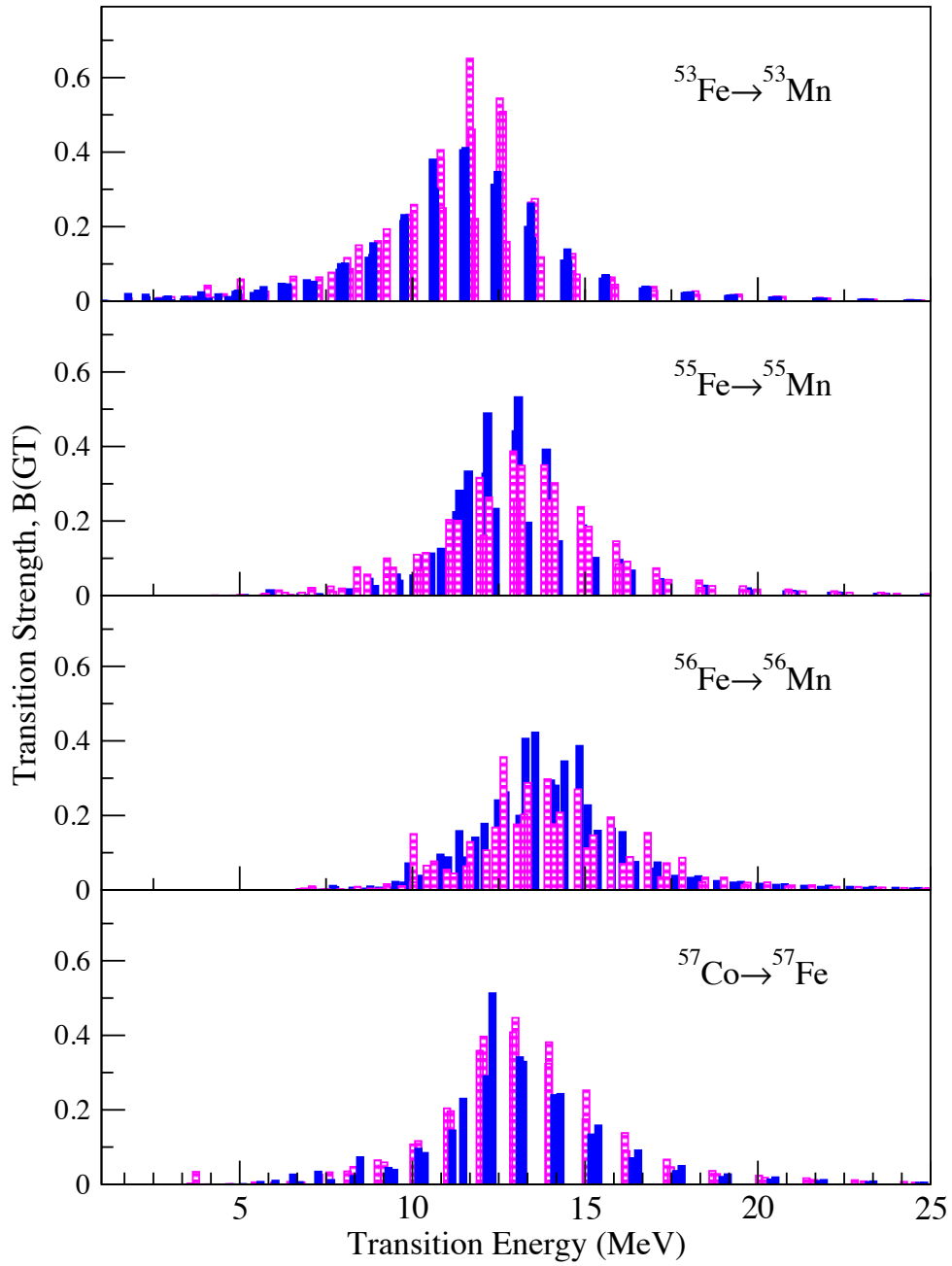
Figure 3.2: Strength functions for various nuclides with two adjacent initial parent states excited near 4.5 MeV, where solid and dotted bars differentiate between the two.

or any resonance peak, can be unclear without folding the peaks together with an appropriate resolution function, as described by Haxton, Nollett, and Zurek [20], but I do not do this here. Instead, one can get around this in other ways by averaging in bins or by using the running sum of the strength function, as will be described in succeeding sections, where in this work I use both.

3.4   Generalized Brink-Axel Hypothesis versus Localization

In this section I analyze how the strength functions evolve with the parent excitation energy. One could examine the average of strength functions, $S(GT)$, for parent states within an energy bin. However, the strength function may not always provide an adequate visual aid to describe desirable features of the transition spectrum. As another tool, I use the running sum, $R(GT)$, which is defined for an initial parent state, i, as a sum over the strength function from equation 1.33:

$$R(GT)[E_i, Q_{if}] = \sum_f \delta(Q_{if} - E_f + E_i) \sum_{f'=1}^{f} B_{if}(GT), \tag{3.6}$$

The running sum gets rid of some of the noise caused in the vacillating strength functions. Also, when plotting a set of individual running sums of strength functions on the same graph, one can see visually the variance of the total strength of the set. Figure 3.3 shows a transition strength function $B(GT)$ simultaneously with its running sum $R(GT)$. $R(GT)$ is a type of discrete integral of the $S(GT)$ with varying intervals int the dependent variable. Thus the slope of the running sum gives an idea of the shape of the $S(GT)$ as well. Increases in slope followed by decreases in slope correspond to broad peaks, where the position of resonances is noticeable.

Now I provide crucial evidence in lower parts of the spectrum that a version of the generalized Brink-Axel hypothesis does hold, that is, one sees the average of running sum strength functions are similar within fluctuations. In these figures, ΔE represents an energy window, where many parents running sum distributions are averaged together around a central parent excitation energy; the resulting distribution is plotted as a function of transition energy
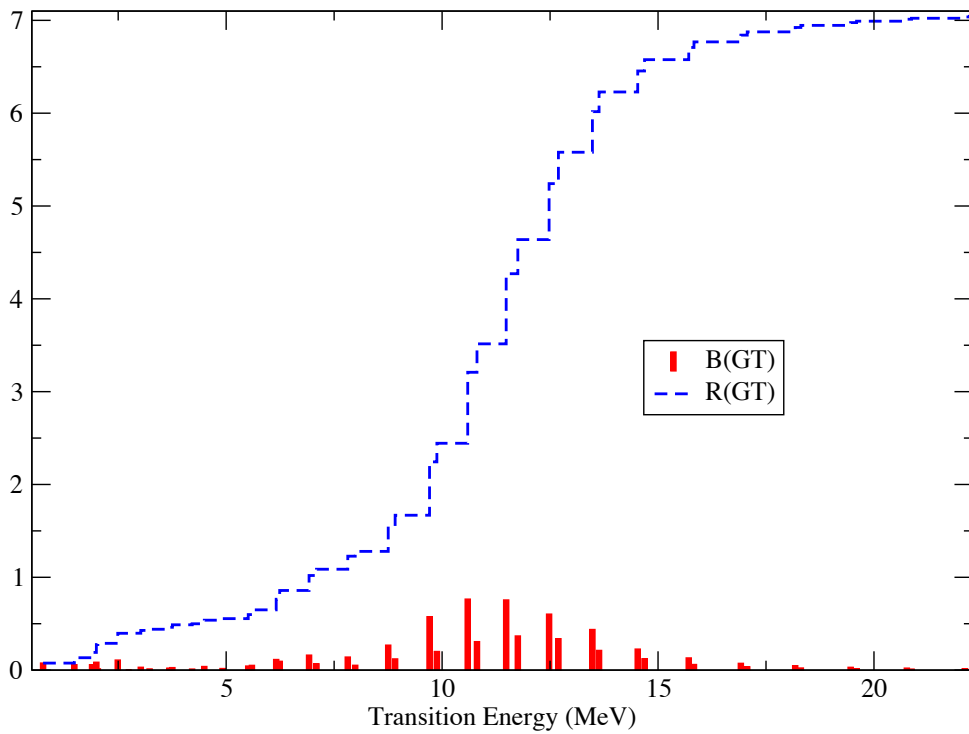
Figure 3.3: The running sum, R(GT), of the transition strength function S(GT) for ^{53}Fe $\rightarrow$ ^{53}Mn for a parent state with $J = T = 0.5$. Note the largest slope of R(GT) occurs at the largest peak of S(GT).
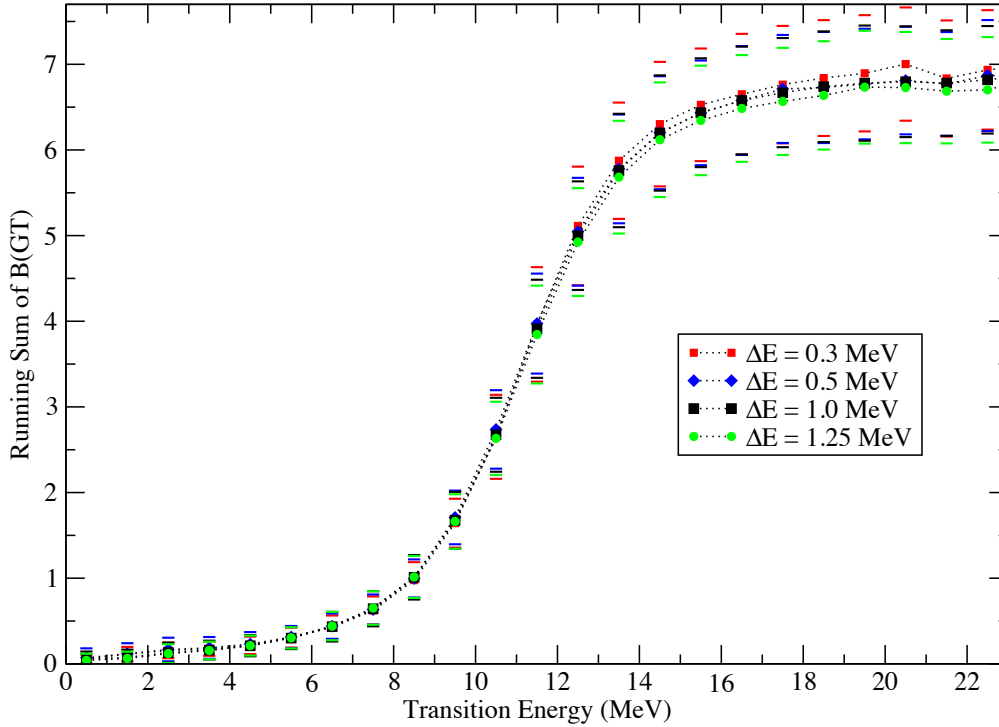
Figure 3.4: Average of running sums in ^{53}Fe $\rightarrow$ ^{53}Mn for parent states around 3.96 MeV

from parent to daughter, in equally spaced 0.5 MeV bins. One can see in Figure 3.4 for the

^{53}Fe $\rightarrow$ ^{53}Mn transition centered at 3.96 MeV, this window does not seem to affect significantly

the variance or shape resulting in self-similar shapes as the size of the windows changes. The

variance in total strength is about 0.6 at the end. At the lower end of excitation energy the variance

is smaller signaling more similarity in shape. Further, the highest slopes for the running sum

would correspond to peaks in the strength function, which in this case are around 11 MeV in

excitation energy. Figure 3.5 shows parents states around 4.92 MeV, which shows similar trends,

except that the smallest energy window of 0.3 MeV has a smaller variance. This means that in

this more restricted region the strength functions are even more alike on average. Increasing the

window gives a larger spread of 0.6 in running strength similar to figure 3.4. To see whether the

above patterns are ubiquitous, I looked at other transitions. Figures 3.6,3.7,3.8, and 3.9 show

other transitions at low energy up below 5 MeV. In general, the data show the independence

of running sum with initial state energy windows of size 0.5-1 MeV. This starts to break down
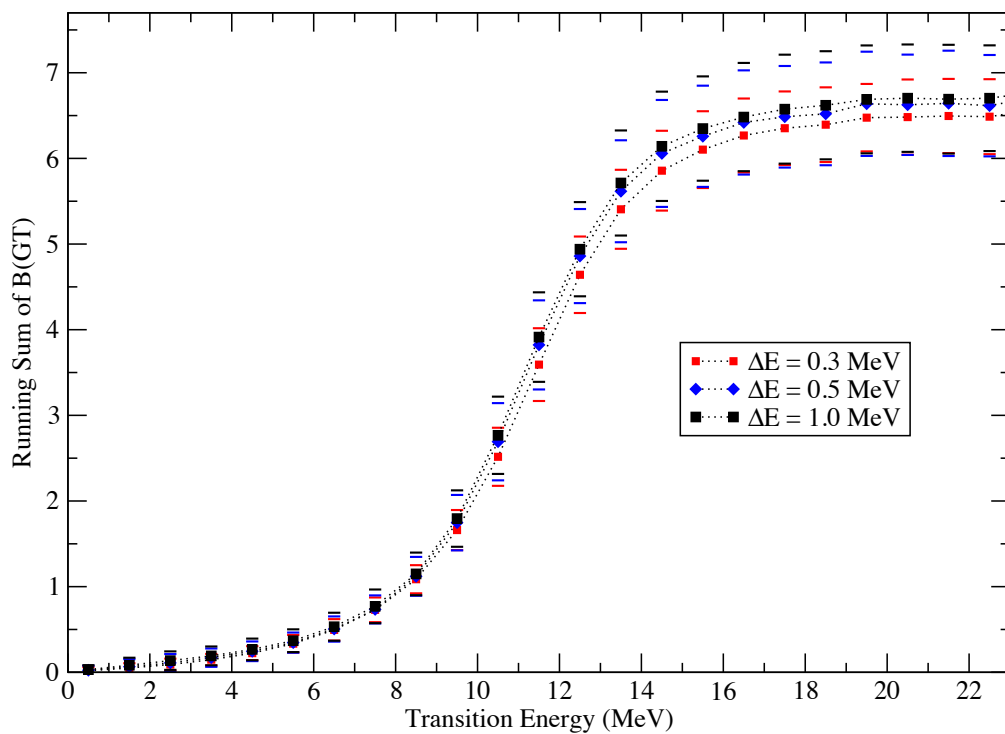
Figure 3.5: Average of running sums in ^{53}Fe $\rightarrow$ ^{53}Mn for parent states around 4.92 MeV
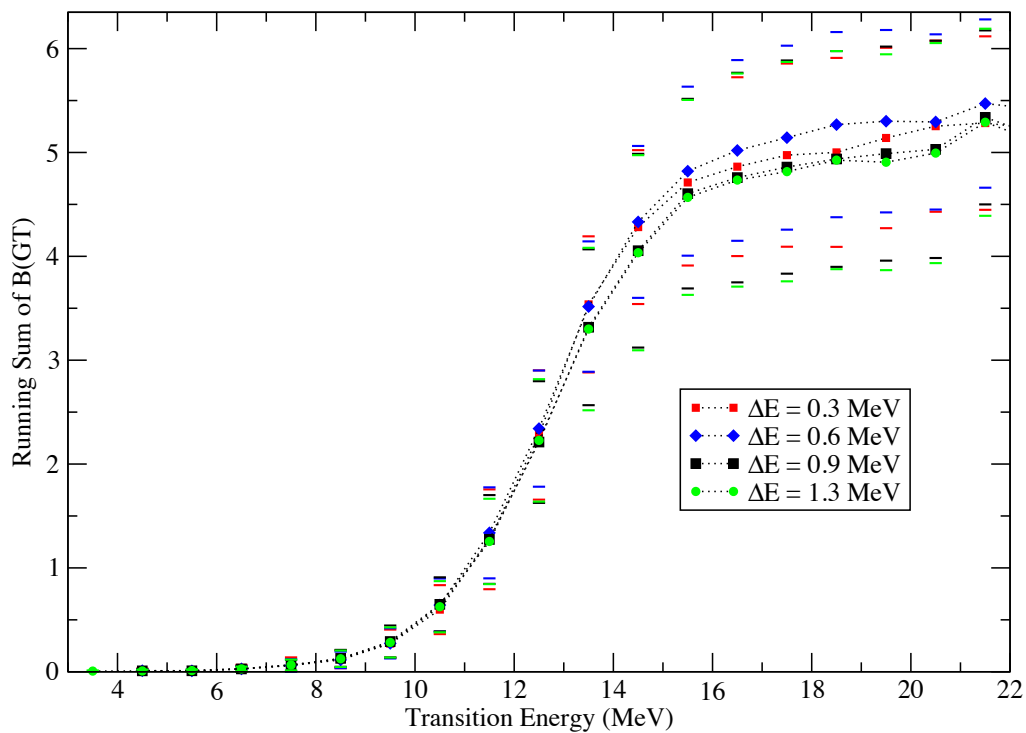
Figure 3.6: Average of running sums in Fe ^{55}Fe $\rightarrow$ ^{55}Mn for parent states around 2.52 MeV
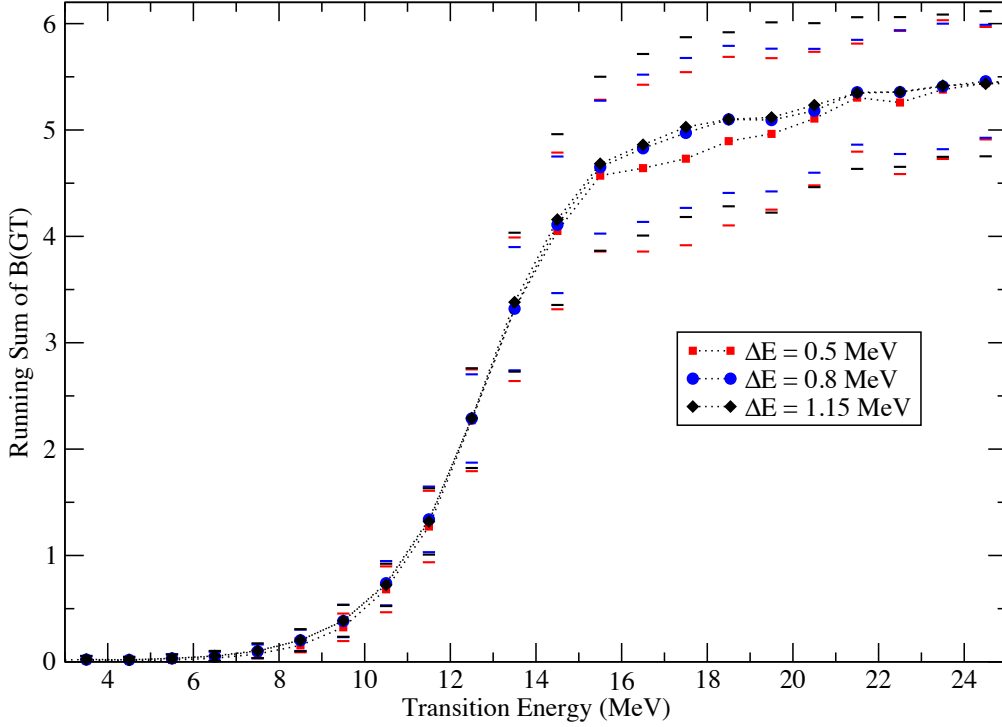
Figure 3.7: Average of running sums in ^{55}Fe $\rightarrow$ ^{55}Mn for parent states around 3.56 MeV

when adding states further away from the mean, or for windows that are two small, where the former shows the breakdown of the Generalized Brink Hypothesis, and the latter is simply due to approaching granular details of individual parent strength functions.

3.5   Semi-Converged States

Unfortunately even with a method that could pick out converged eigenstates in energy windows in more advanced parts of the spectrum, for high energies the level density gets so large that available computational resources are insufficient necessary to resolve the many tightly packed quasi-continuous states. Thus I explore whether it is necessary to have a fully converged state by comparing to semi-converged states. These semi-converged parent excited states were projected to good J and T, but are only partially localized in energy. The variance around the peak for a such a parent state, $|\psi\rangle$, is given by the formula $\langle H^2 \rangle_\psi - \langle H \rangle_\psi^2$ with the expectation value
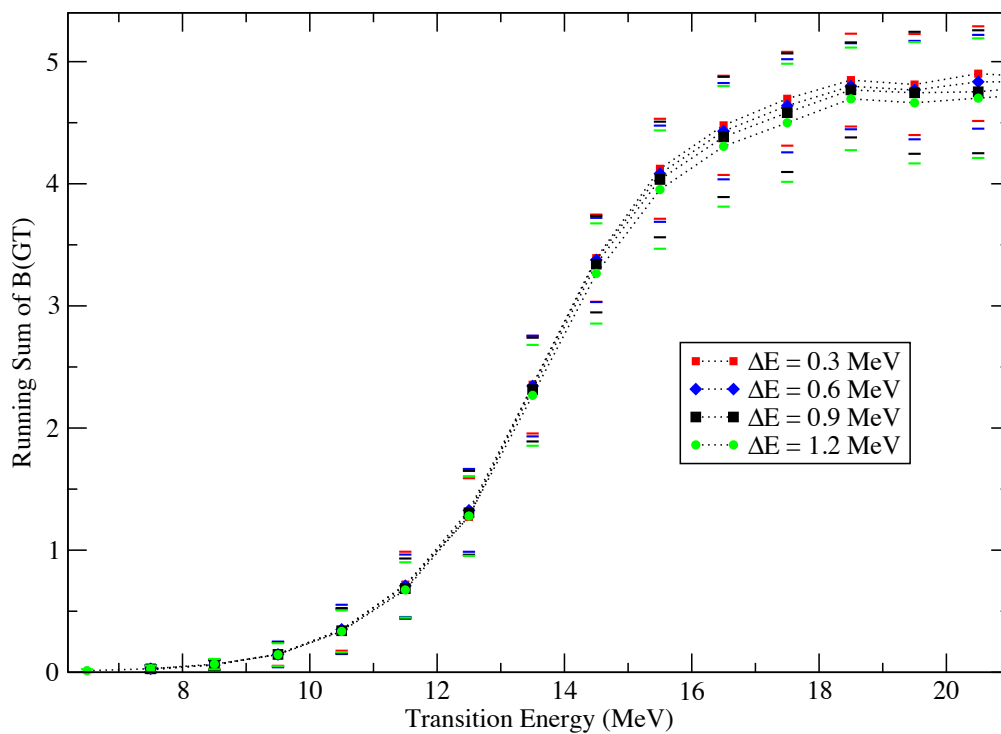
Figure 3.8: Average of running sums in ^{56}Fe $\rightarrow$ ^{56}Mn for parent states around 3.29 MeV
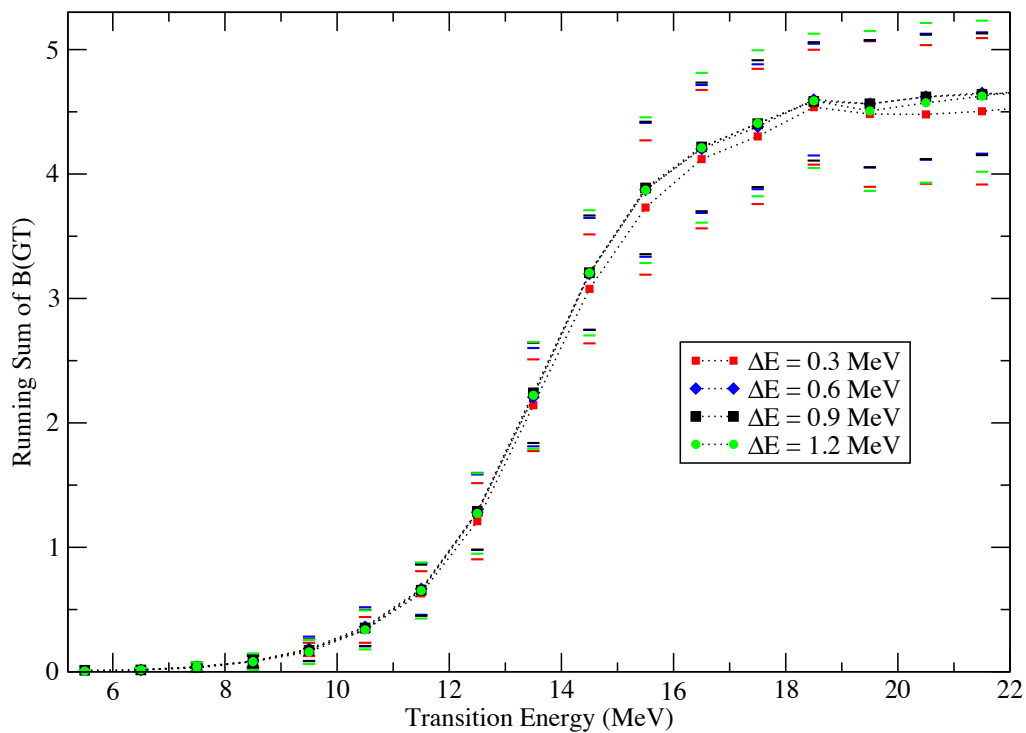
Figure 3.9: Average of running sums in ^{56}Fe $\rightarrow$ ^{56}Mn for parent states around 4.25 MeV

for an operator O defined as $\langle O \rangle_\psi = \langle \psi | O | \psi \rangle$. In the figures in this section, semi-converged parent states have fixed T, T_z, and M, but can be decomposed as linear combinations for possible J:

$$|\psi\rangle = \sum_J C_J |JMTTz\rangle, \tag{3.7}$$

where in the figures C^2 is therefore the amplitude squared, or probability, of such a state being measured to have angular momentum, J. As mentioned previously, I use targeted thick restart Lanczos, to localize the state to within the desired energy window, where one would expect strength functions to be similar.
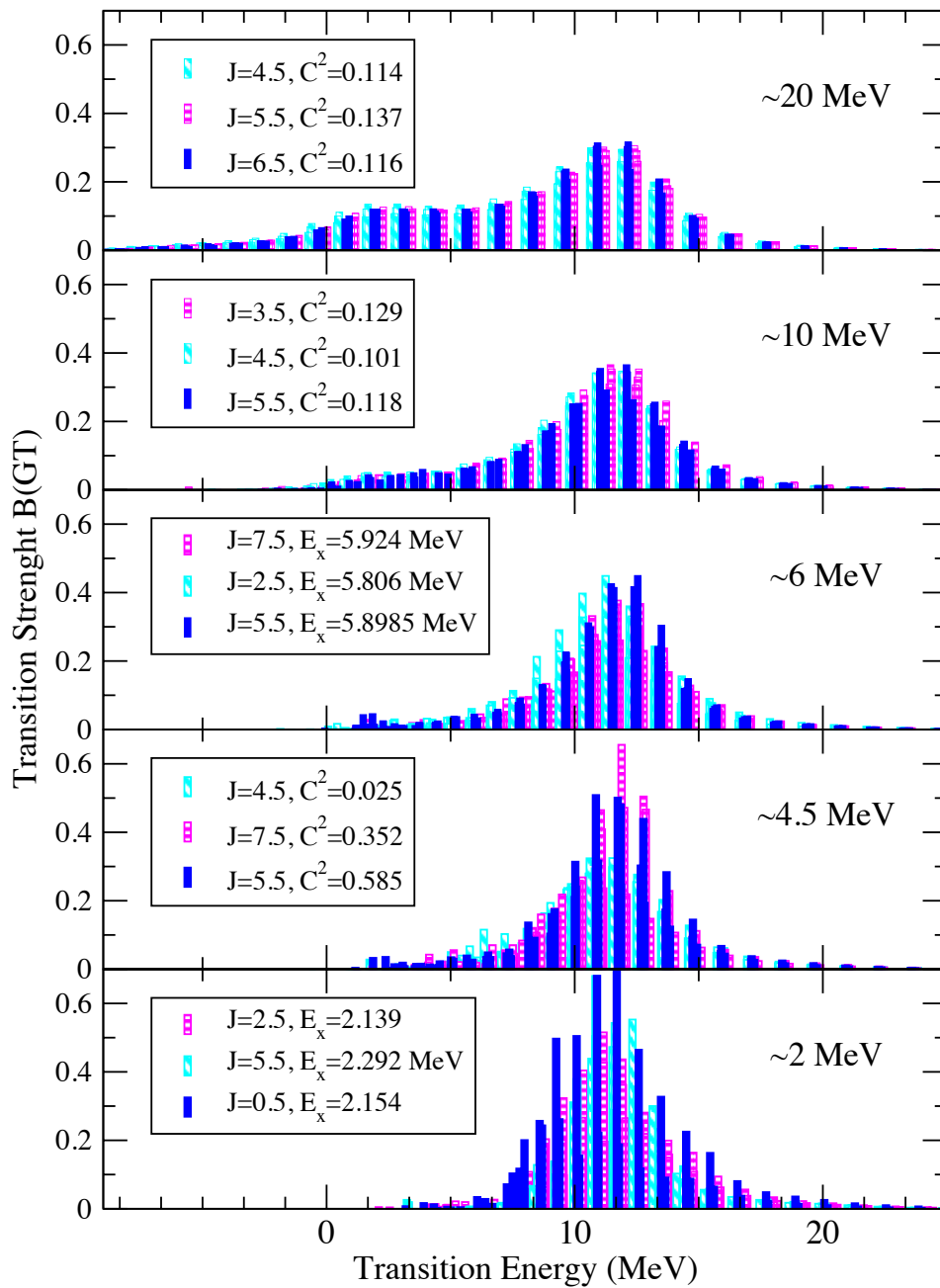
Figure 3.10: The evolution of the transition ^{53}Fe $\rightarrow$ ^{53}Mn as one goes higher in parent excitation energy. Each graph has strength functions for parents of different angular momentum J. Those having C^2 are semi-converged states projected to the given J, and those having excitation energy, E_x, are fully converged states of that specific excitation energy.

That is, the strength functions follow a *Local Brink Axel Statement* (LBAS), where for the strength function in equation 3.2, I claim:

> The strength function evolves in a secular fashion, such that, within a sufficiently small energy window the spectral distribution from nearby parent excited states to their daughter states is the same independent of the parent index, i.

As a first example, figure 3.10 has examples of strength functions at successive energy scales for the transition ^{53}Fe $\rightarrow$ ^{53}Mn, which could be used to compute electron capture or positron decay rates. The functions are very similar in shape and magnitude. There is an evolution going up in excitation energy, where at around 20 MeV in initial parent excitation (top graph) there is a second peak around 2-3 MeV transition energy. To show that this phenomenon is ubiquitous, Figure 3.11 has strength functions for a transition between ^{55}Cr $\rightarrow$ ^{55}Mn, which could be used in electron decay or positron capture calculations. Here the same pattern arises, where as one goes up in parent excitation energy a peak on the right is shrinking from 1.5 to 1 strength units, while a second peak on the left side is growing.

Notice that in Figure 3.11, the 5 MeV parent case (middle graph) the dashed line goes higher than the other two, but still follows a similar pattern. This is because it is a $J = 1/2$ line, so it has less transition channels and resulting data points, which makes it appear less smooth. Often these are smoothed out with Gaussian or Lorentzian functions that are appropriate in matching the experimental spectrum [20].

Thus one can see that the Brink-Axel hypothesis is broken, in that when going up in energy the shape of the distribution changes. But this work shows that the magnitude of the total sum evolves in a smooth manner. Further, it appears that parent states that are close in energy are very similar and get closer to identical as the parent excitation energy is increased. This gives strong evidence for the LBAS described earlier.

Similar conclusions can be drawn for the running sums, $R(GT)$. First in figure 3.12, I compare to the averages computed in section 3.4 for ^{53}Fe $\rightarrow$ ^{53}Mn at lower energy values around
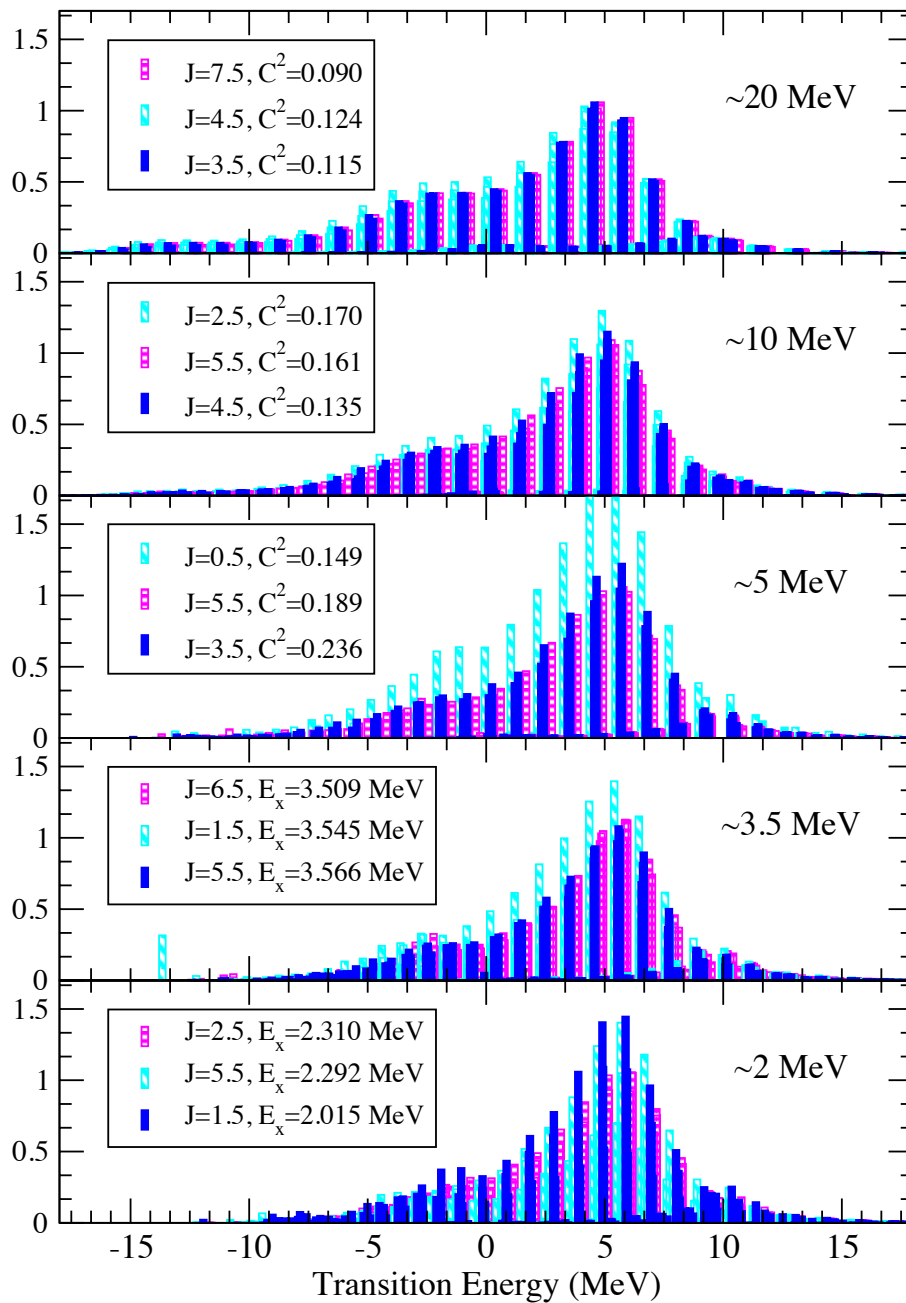
Figure 3.11: The evolution of the transition $^{55}\text{Cr} \rightarrow {}^{55}\text{Mn}$ as one goes higher in parent excitation energy. Each graph has strength functions for parents of different angular momentum J. Those having C^2 are semi-converged states projected to the given J, and those having excitation energy, E_x, values are fully converged states of that specific excitation energy.
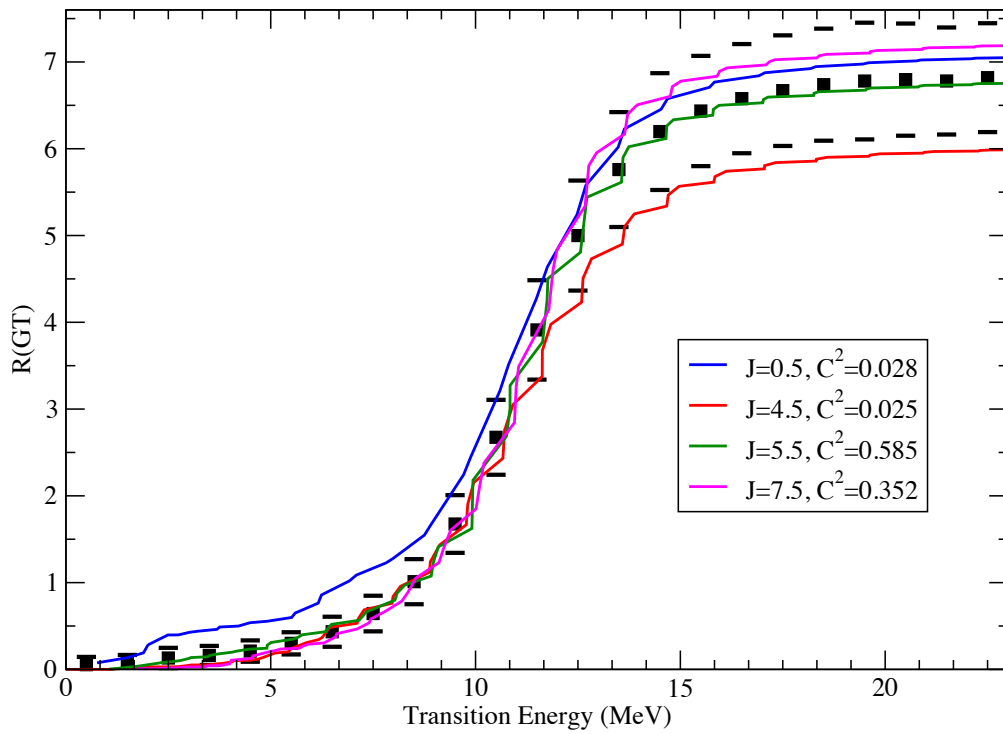
Figure 3.12: Comparison of running sums for converged states average around 4.5 MeV excitation (blocks and broken lines) and individual semi-converged states also around 4.5 MeV excitation (colored, connected lines) in the ^{53}Fe $\rightarrow$ ^{53}Mn transition
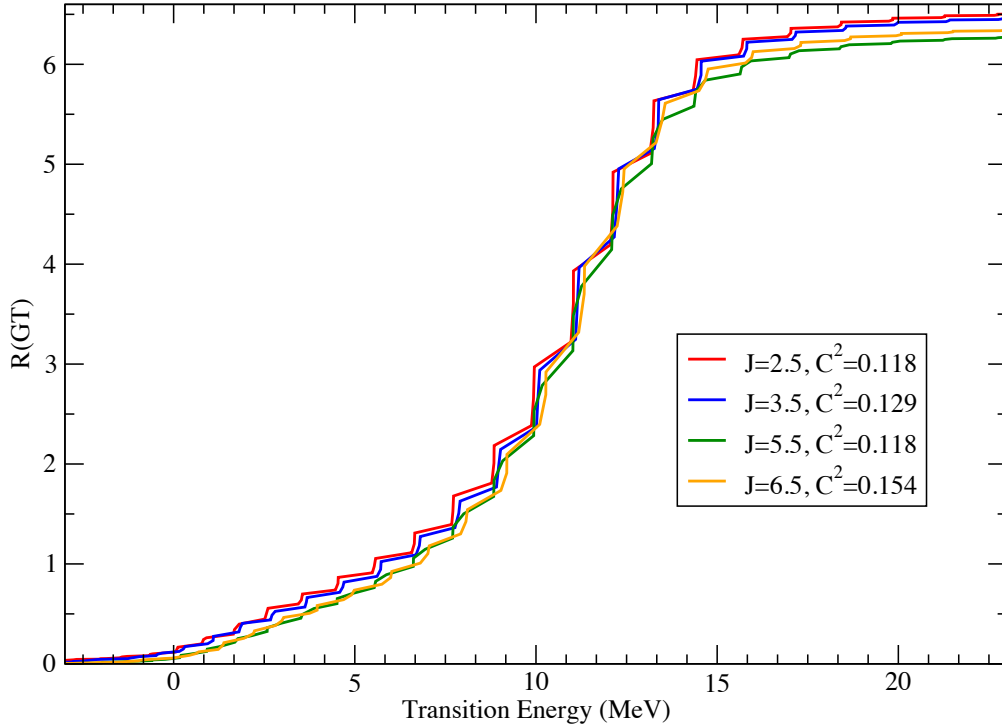
Figure 3.13: Running transition strength sums in ^{53}Fe $\to$ ^{53}Mn for semi-converged parent states around 10 MeV

5 MeV. One can see that the semi-converged states seem to mostly fall within the averages, which confirms that they follow the pattern 1 of a generalized Brink hypothesis.

Unfortunately as mentioned before because of computational constraints one cannot generally go much beyond 5-15 MeV if fully converged states are used. Thus for higher excitation energies at 10 and 20 MeV I again use projections of semi-converged states. Notice in figures 3.13 and 3.14 that as one progresses higher in the energy spectrum the shape of the running sum of strength becomes independent of J, and are virtually identical. However, the curve starts to spread out more towards negative transition energy, evolving smoothly as parent energy increases to 10 MeV and 20 MeV. This shows more evidence for a version of the Brink hypothesis, but one that is localized. In addition, it seems that the total strength has a slight J dependence with higher J having smaller total strength, where this is most pronounced in the 20 MeV case at about a 5 percent deviation.
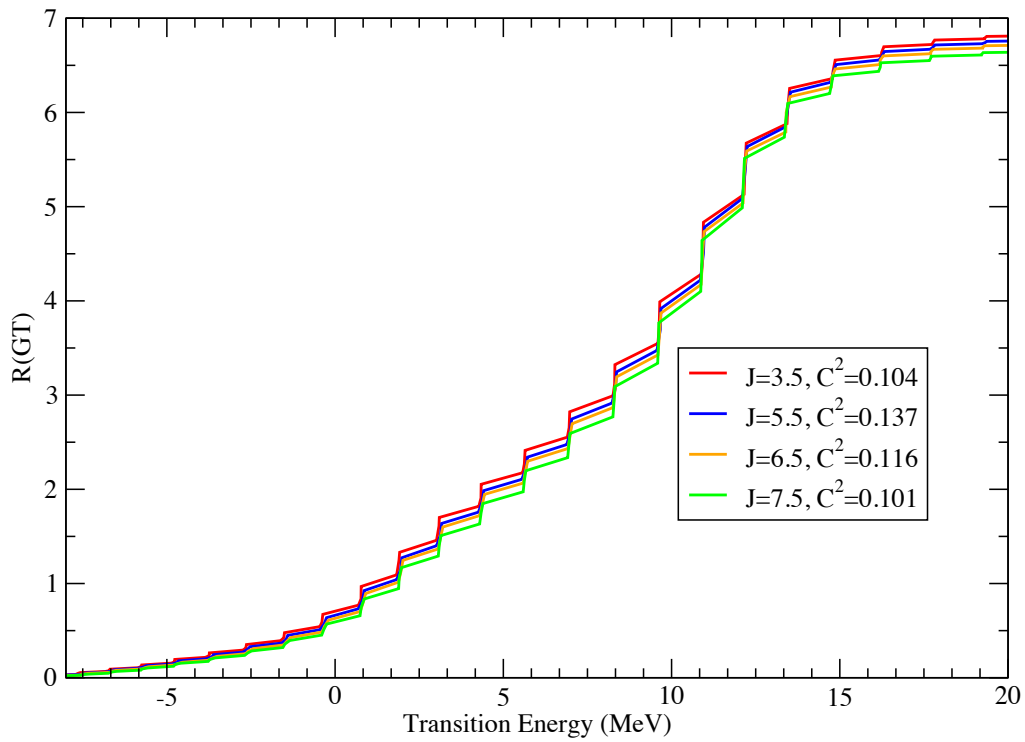
Figure 3.14: Running transition strength sums for ^{53}Fe $\rightarrow$ ^{53}Mn for semi-converged parent states around 20 MeV
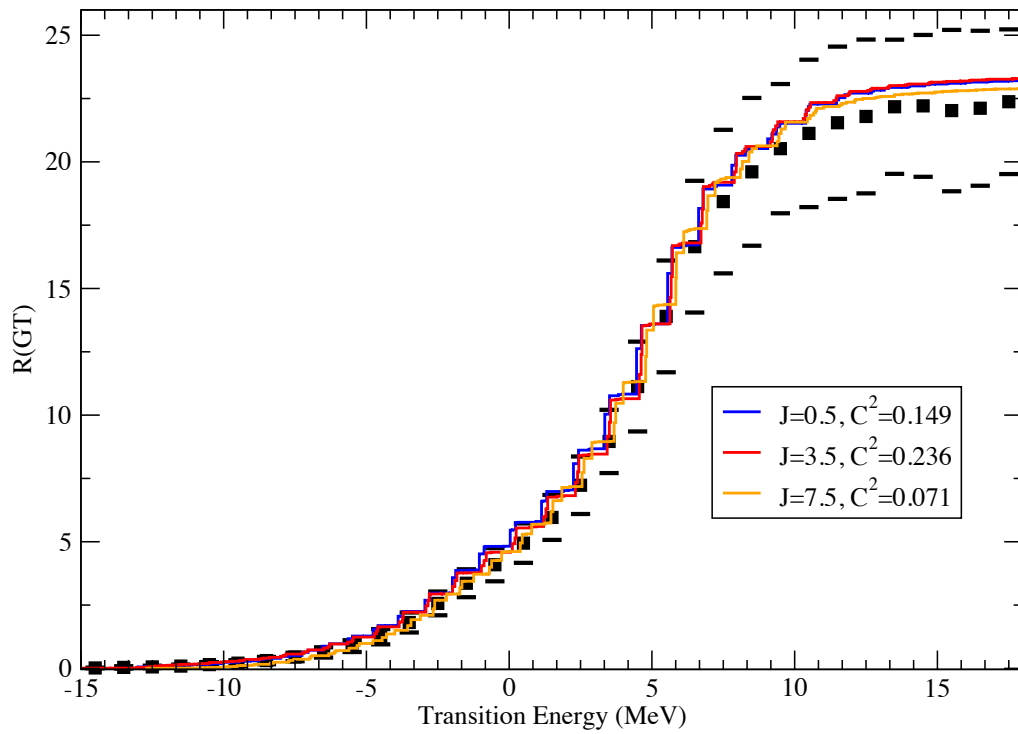
Figure 3.15: Comparison of running sums for converged states average around 4 MeV excitation (blocks and broken lines) and individual semi-converged states around 5 MeV excitation (colored, connected lines) in the ^{55}Cr $\rightarrow$ ^{55}Mn transition
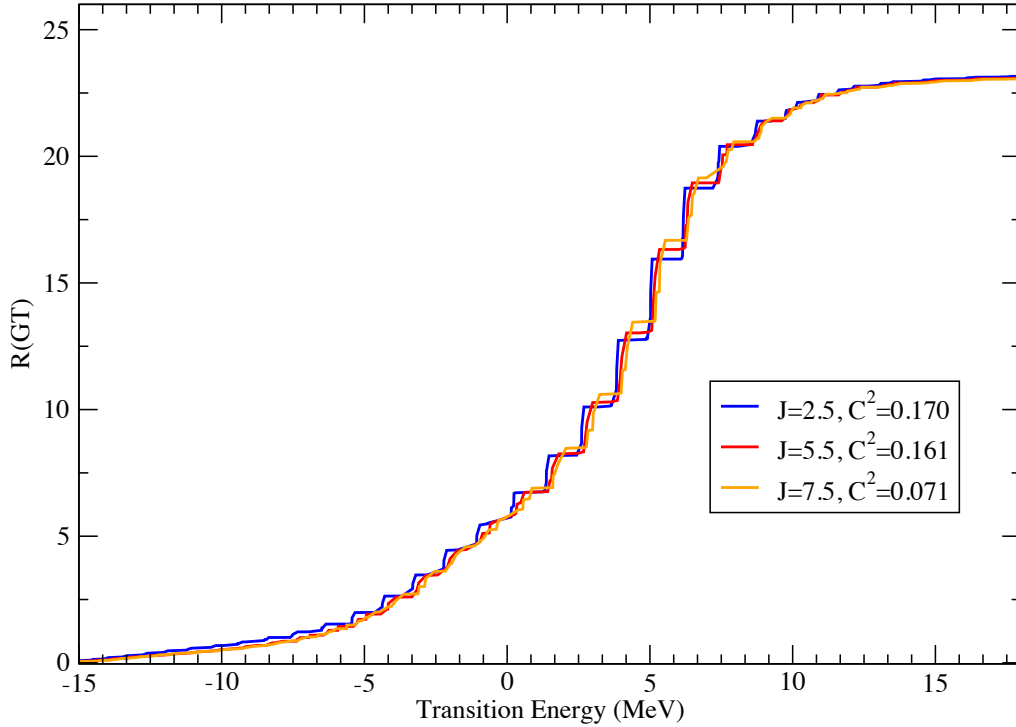
Figure 3.16: Running transition strength sums for ^{55}Cr $\rightarrow$ ^{55}Mn for semi-converged parent states around 10 MeV

There is very similar behavior but now in the direction of lowering isospin for the transition ^{55}Cr $\rightarrow$ ^{55}Mn, where the transition could electron decay or positron capture. In figure 3.15, one sees that the semi-converged states line up well within the variance of the converged average for around parent excitation energy 4-5 MeV. As parent excitation energy increases, as in figures 3.16 and 3.17, the same two features appear again. That is, the overall shape of the curves become less dependent on the angular momentum J of the parent excited state, but the total strength also has a slight systematically decreasing dependence on J though now much smaller at less than 1 percent. However, one major difference is that the total sum has not changed much from $R(GT) = 23$ for this transition as we increased parent excitation energy.
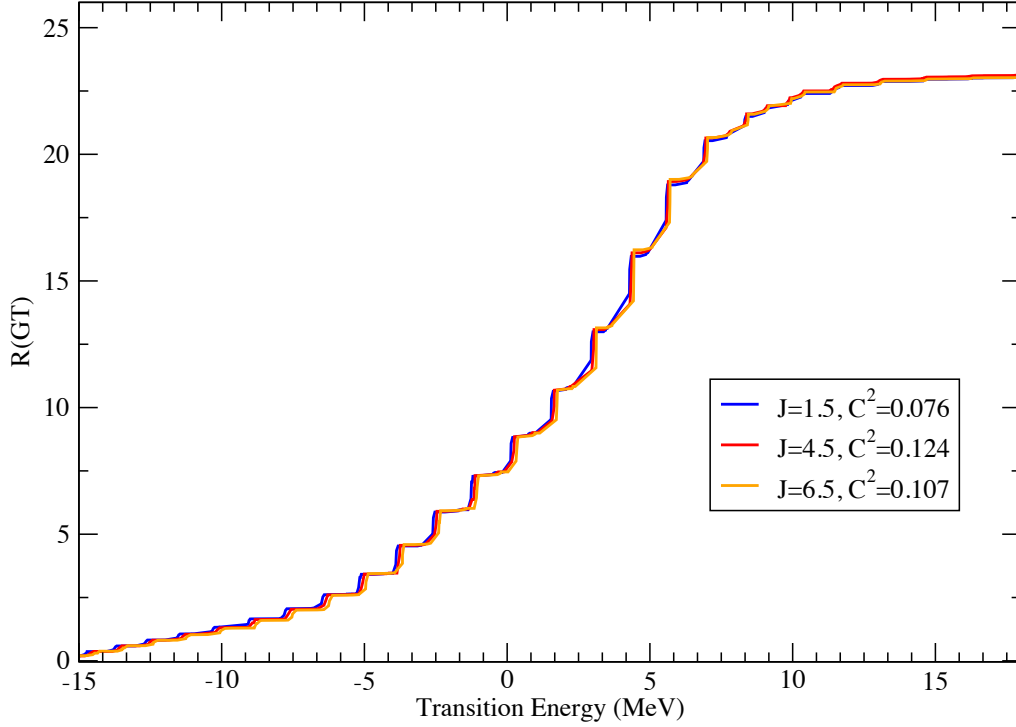
Figure 3.17: Running transition strength sums for ^{55}Cr $\rightarrow$ ^{55}Mn for semi-converged parent states around 20 MeV

3.5.1   Application to Massive Stellar Thermal Rates

In astrophysical applications, such as pre-collapse massive stars, the high temperatures in billions of kelvin make higher energy parent states more significant in the thermal sum of rates. The Fermi and Gamow-Teller rates determine the baryon to lepton fraction and the neutrino flux, which are vital inputs to the final collapse dynamics of a star and the composition of the products.

As a test of the efficacy of the method, I calculated the thermal GT rates for ^{57}Co $\rightarrow$ ^{57}Fe, a near 1 billion basis dimension case, and much larger compared to previous studies. I affirm that the contributions of excited states to stellar transition rates are more important at high temperatures. Here I look at both electron capture and positron decay rates for ^{57}Co, which was chosen because the basis size being around 1 billion gives a good test of the BIGSTICK code [15], but also because it was noted as significant in recent pre-collapse stellar evolution research [76]. These BIGSTICK derived rates are compared to the work of Fuller, Fowler, and Newman

(FFN) [17], and also the work of Langanke and Martinez-Pinedo (LMP) [73].

Importantly, the standard formulas used for weak interaction transition rates given in FFN and LMP are applied. Phase space factors account for the final states of the electron and neutrino, where the Q-value, Q_{ij}, goes to their mass and kinetic energy depending on the reaction type. As seen in the previous sections, parent energy windows around 1 MeV give strength functions that are increasingly similar, particularly for excitation above 5 MeV where our ability to converge eigenstates is gets more and more limited. Therefore as the approximation method derived from the LBS, we take that in these energy windows or *bins* the excitation probabilities P_i, the reduced transition probabilities, $B(GT)$, and the phase factors, Φ_{if}, are identical. This means that these factors are also independent of energy, angular momentum, or isospin, where when the energy factors in I use the midpoint energy, ε, of the window. The equation 1.35 for thermal transition rates, where the sum over initial states i, is re-done with a *converged state sum* that proceeds normally, and a *semi-converged state sum* in $\Delta\varepsilon = 2$ MeV wide bins that does the rest up to convergence of the total transition rate:

$$
\begin{aligned}
\lambda &= \sum_i P_i \sum_f B_{if}(GT)\Phi_{if} \\
&\approx \sum_{i=1}^{N_{conv}} P_i \sum_f B_{if}(GT)\Phi_{if} + \sum_{bin=1}^{N_{bins}} P_{\varepsilon(bin)} \, N_{\varepsilon(bin)} \sum_f B_{\varepsilon(bin),f}(GT)\Phi_{\varepsilon(bin),f},
\end{aligned}
\tag{3.8}
$$

where $bin = 1$ picks up at states starting above the highest energy converged state and the total partition function is also split as:

$$
G \approx \sum_{i=1}^{N_{conv}} e^{-E_i/kT} + \int_{\varepsilon(bin=1)-\Delta\varepsilon/2}^{\varepsilon(bin=1)-\Delta\varepsilon/2+N_{bins}\Delta\varepsilon} e^{-E_x/kT} D(E_x)dE_x
\tag{3.9}
$$

As a result, two new factors must be introduced in the semi-converged sum, namely the number of states in the energy window, $N_{\varepsilon(bin)} = \int_{bin} D(E_x)dE_x$, and $D(E_x)$ the corresponding level density, where the integration is over the excitation energy of the parent nucleus, E_x. Therefore the level

81

density plays a significant role in these calculations, and the sensitivity of thermal GT rates to level density will be explored in section 3.5.4. I will give results using two different level densities, one from the shell model used in calculation and one from an empirical back-shifted Fermi Gas fitted to experiments [77].

These sums are used in conjunction with the following phase space factors for electron capture and positron decay:

$$
\begin{aligned}
\Phi_{ij}^{(ec)}(\mu_e, T) &= \int_{W_{min}}^{\infty} W \sqrt{W^2 - 1}(Q_{ij} + W)F(Z, w)f(T, \mu_e, +\varepsilon)dW \\
\Phi_{ij}^{(pd)}(\mu_e, T) &= \int_{1}^{W_{max}} W \sqrt{W^2 - 1}(Q_{ij} - W)F(-(Z-1), w)f(T, \mu_e, -\varepsilon)dW,
\end{aligned}
\tag{3.10}
$$

with $W_{max} = Q_{ij}$ and $W_{min} = 1$ if $Q_{ij} > -1$, or else $W_{min} = |Q_{ij}|$, when where $F(Z, W)$ is called the Fermi function that accounts for the attraction of beta particle and the nucleus:

$$
F(Z, w) = 2(1 + \gamma)(2pR)^{-2(1-\gamma)} \frac{|\Gamma(\gamma + i\alpha Zw/p)|^2}{|\Gamma(2\gamma + 1)|^2}
\tag{3.11}
$$

with $\gamma = \sqrt{1 - (\alpha Z)^2}$, where α is the fine structure constant, and R is the nuclear radius. Finally $f(T, \mu_e; Wm_ec^2)$ are the Fermi-Dirac statistics for the beta particles:

$$
f(T, \mu_e, \varepsilon) = \frac{1}{\exp\left(\frac{\varepsilon - \mu_e}{kT}\right) + 1}
\tag{3.12}
$$

Here μ_e is the electron chemical potential and $p = \sqrt{W^2 - 1}$ is the momentum in units of the mass of the electron times the speed of light (m_ec). The total energy of the electron including mass is $\varepsilon = Wm_ec^2$. For the transition energy defined in equation 3.5, $Q_0 = M_p - M_d$ in units of m_ec^2 with M_p and M_d the nuclear masses of the parent and daughter, respectively. The chemical potential was obtained using a root-finding algorithm on the following integral equation:

$$
\rho Y_e = \frac{(m_ec)^3}{\pi^3 \hbar^3 N_A} \int_{1}^{\infty} W \sqrt{W^2 - 1}[f(T, \mu_e, \varepsilon) - f(T, -\mu_e, \varepsilon)]dW,
\tag{3.13}
$$

where $\hbar$ is Boltzmann's constant and N_A is Avogadro's number.

At 4 MeV up to 80 MeV, semi-converged states are used at 2 MeV intervals. The approximation is used that all the transition strength functions in these intervals for states of different J are identical. The contributions of higher isospin $T = 5/2$ states are less than ten percent up to 25 MeV, where most of the strength has been summed for the temperatures computed in this work, but pass 30 percent near 80 MeV along with the rise of $T = 7/2$ states. These energies ranges open up Fermi transitions to the isobaric analogs from the ^{57}Co parent. Lastly, the Boltzmann factor used is constant in each interval, where I take the midpoint of the energy. However, this report is meant to just give very basic results for the thermal rates of ^{57}Co $\rightarrow$ ^{57}Fe, so as to give opportunity for feedback, as this is the capstone of the final chapter.

The LMP and FFN rates were obtained from the MSU NSCL Charge Exchange Group at URL: https://groups.nscl.msu.edu/charge_exchange/weakrates.html. The parent energy levels and transition rates I computed using the GXPF1A interaction [9]. The Gamow-Teller operator is generated using auxiliary code provided with BIGSTICK [15].

3.5.2   Electron Capture Results, ^{57}Co $\rightarrow$ ^{57}Fe

First consider a comparison of FFN and LMP electron capture rates: As one can see, the FFN electron capture rates in figure 3.18 are generally higher than the LMP rates, in some case by many orders of magnitude, but become much closer at high temperature and separately at high density as well. This was noted to be a general trend for the various nuclides and beta processes, which for electron capture rates would result in higher values for Y_e and the in the production of neutron-rich nuclei [73].

For electron capture, one sees that my rates have similarities to LMP with some notable differences. In Figure 3.19, I show another comparison of rates but this time for two different level densities including my *full* rates with semi-converged excited states added and *partial* rates that don't include excited states at all (marked by 'X'). At the highest temperature regions, Note
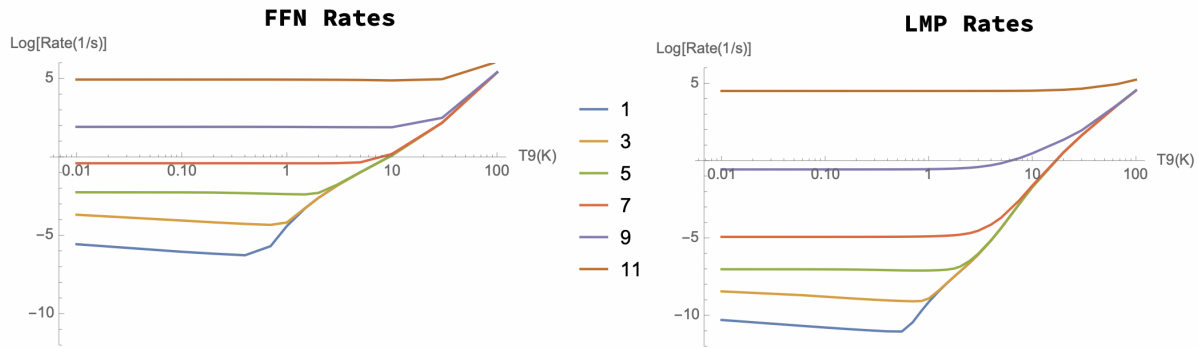
Figure 3.18: Comparison of previous work in electron capture for ^{57}Co $\rightarrow$ ^{57}Fe. The numbers in the legend are $Log[\rho y_e] = 1, 3, 5, \ldots$, that is, density times electron fraction in grams per cubic centimeter. The lines are plotted in reverse order to the legend, so that $Log[\rho y_e] = 1$ is the first line from the bottom.

three different regions in Figure 3.19. First at low temperature and low density both my full and partial rates are virtually identical to the LMP rates. Going up in density to 10^9 g/cm^3 ($Log[\rho y_e] = 9$), both the full and partial rates are about 0.2-0.3 higher in log-rate, or almost a factor of 2 in absolute rate over the LMP rates. In the high temperature range approaching 10^{10} K and higher with densities higher than or equal to 10^5 g/cm^3 ($Log[\rho y_e] = 5$), the empirical level density full rates (bottom graph) are even higher and lifted off by up to 1 in log-rate or a factor of 10 in absolute rate. Going up a bit more in temperature, the full shell model rates (top graph) also start to have noticeable increases over the LMP rates. Lastly, in both graphs at high temperature and density, the difference between the full rates and the partial rates (marked by 'X') increases as temperature increases.

3.5.3   Positron Decay Rates, ^{57}Co $\rightarrow$ ^{57}Fe

The positron decay rates, show more drastic differences. At low temperature and density, the positron decay rates are many orders of magnitude smaller than electron capture; however, at extreme temperature and density they become comparable to other processes and may contribute in a significant way. The chemical potential for positrons is such that there is not much difference
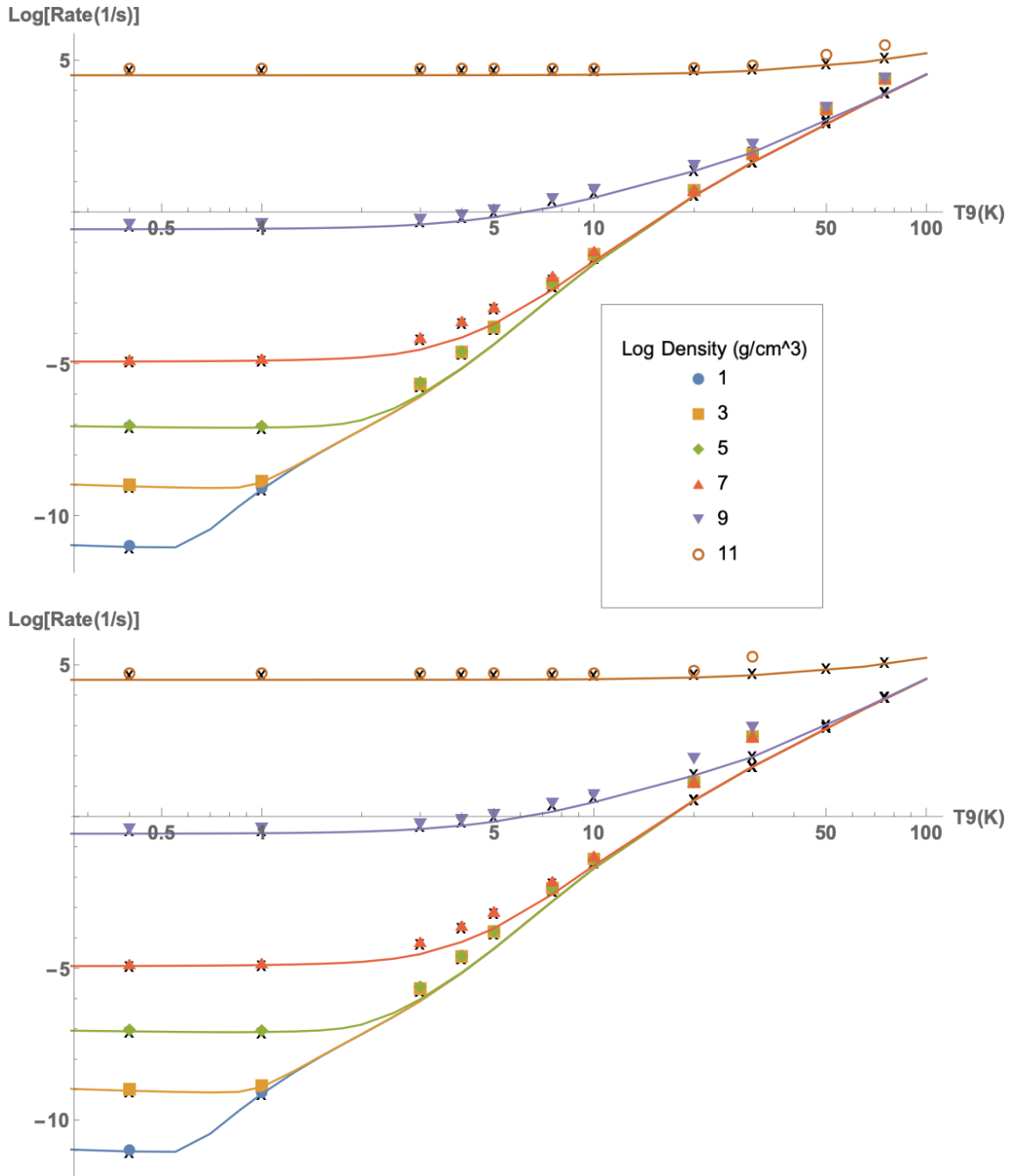
Figure 3.19: Electron capture in ^{57}Co $\rightarrow$ ^{57}Fe. Top graph is using the gaussian shell model level density, and bottom is using the empirical level density. The lines represent the LMP rates, and the symbolic markers represent my full rates. The values marked by 'X' are partial rates that do not include the semi-converged excited state contribution. The plotting of lines is in reverse to the legend, where $Log[\rho y_e] = 11$ is the topmost line.

in the rates for different stellar densities ($Log[\rho y_e]$). Thus in the two graphs in Figure 3.20, all lines overlap. As with the electron captures rates, the positron decay rates computed in this work are noticeably higher for high temperature and densities when compared to the LMP rates, but lower than the FFN rates in the regions computed. However, there are two other important features. First, at low temperature the full and partial rates are higher than the LMP for both level density graphs, but increase at a slightly lower trend as one goes higher in temperature. Second, at around 5×10^9 K, the full rates I derived using shell model and empirical level densities start to deviate significantly from the LMP line and head toward the FFN line, but then the full shell model density rates slow down and follow a similar curve to LMP. The partial rates (marked by 'X') are dramatically less than any of the other rates graphed including LMP. Importantly, my full rates in both graphs are 1-2 orders of magnitude higher than LMP at these higher temperatures for both level densities.

3.5.4   Level Densities and Convergence of LBAS Method, $^{57}\text{Co} \rightarrow {}^{57}\text{Fe}$

As I showed in preceding sections, knowledge of the density of energy levels for parent nuclei becomes necessary for this binned approximation. In these calculations, the shell model level density is well approximated by a Gaussian function, or normal distribution, of the form $D(E_x) = \frac{C}{\sigma\sqrt{2\pi}}e^{-\frac{1}{2}(\frac{E_x-\mu}{\sigma})^2}$, where E_x is the nuclear excitation energy. Also, for this transition $C = 980,474,907$ is the total number of states, $\sigma = 12.55$ is the standard deviation or width, and $\mu = -147.15$ is the energy centroid for the ^{57}Co nucleus. On the other hand, the back-shifted Fermi gas model, which is empirically fitted to experimental data, takes the form:

$$D(E_x) = \frac{\exp\left(-2\sqrt{a(E_x-\delta)}\right)}{12\sqrt{2}\sigma a^{1/4}(E_x-\delta)^{5/4}} \tag{3.14}$$

The values for $^{57}\text{Co} \rightarrow {}^{57}\text{Fe}$ in this empirical model are the level density parameter, $a = 6.5$, and the backshift parameter, $\delta = 0.7$ MeV. These parameter values were obtained from Mishra et al.
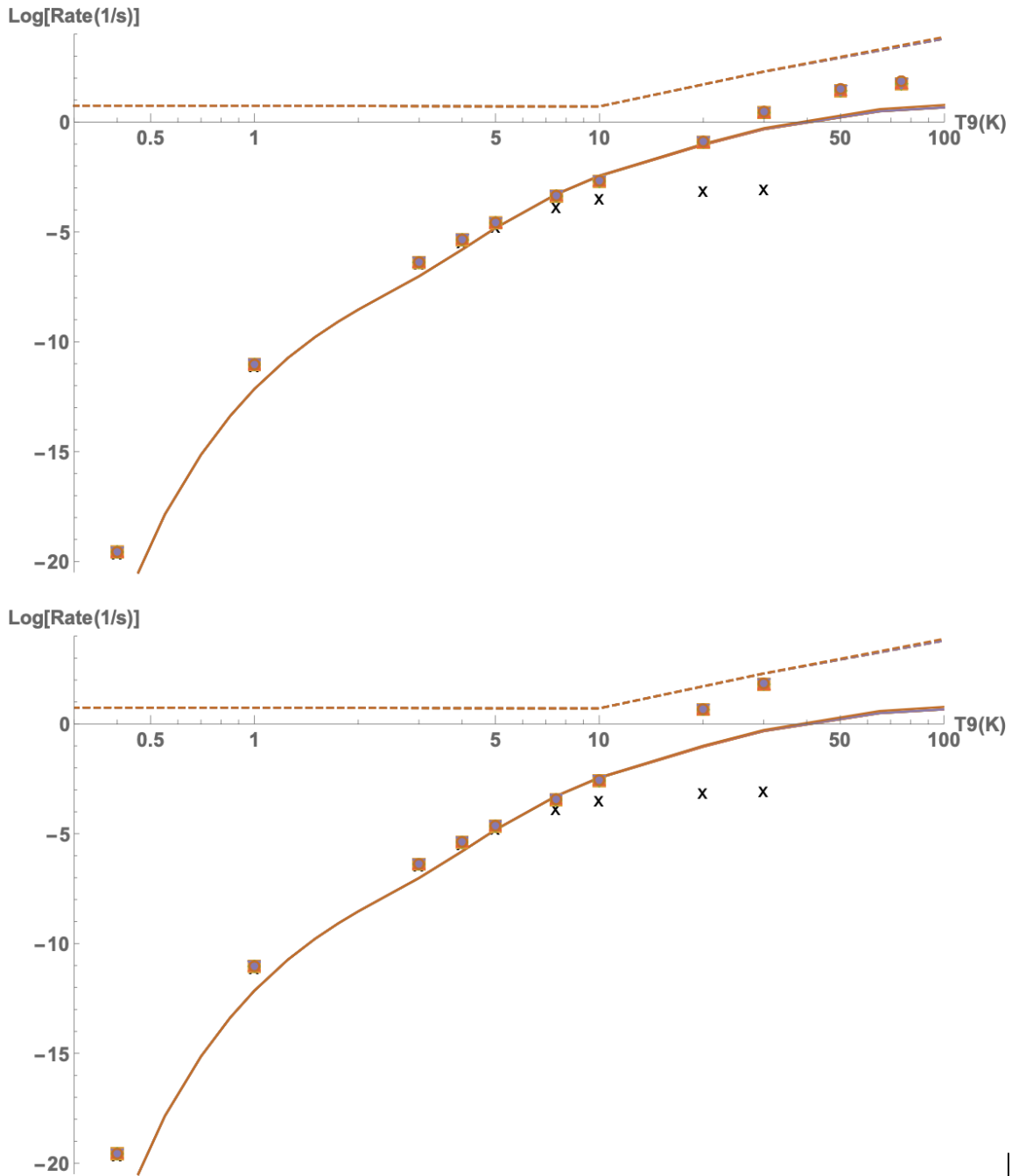
Figure 3.20: Positron decay in ^{57}Co $\rightarrow$ ^{57}Fe. Top graph is using the shell model level density, and bottom graph is using the empirical level density. The solid lines represent the LMP rates and the dashed lines represent the FFN rates, and the symbolic markers represent my full rates. The log-rates are mostly indistinguishable for all stellar densities $Log[\rho y_e]$. The values marked by 'X' are partial rates that do not include the semi-converged excited state contribution.

[77], but not given there was the spin-cutoff parameter σ though it was noted that the dependence on σ is weak with a tolerance of 20 percent. I use $\sigma = 3.96$ taken from graphs for pf-shell nuclei in Spinella and Johnson [78], where $\sigma = \langle J_z^2 \rangle$ is dependent on excitation energy but it is shown to be approximately constant over a wide range in the PF shell.

When discussing the convergence of their method, LMP describes using so-called 'average states' that are not fully converged, which are essentially like the semi-converged states I use though presumably at different levels of energy localization. However, it is unclear how these states were applied in their work. I assume they were treated like typical parent states with specific quantum numbers that would have to be rounded, if not converged to good values. Instead my use of the LBAS implies that I should treat a semi-converged parent states just like any other within the energy window as if all these states had the same strength function regardless of quantum number, except perhaps for isospin. Therefore, I only need to count the number of states in the window, hence the need for the level density.

This leaves us with an important caveat: the empirical back-shifted Fermi Gas level density grows much faster than the shell model level density, which directly affects the parent state partition function and the total states per energy bin from our LBAS approximation in equation 3.8. Thus, for the same weak interaction matrix elements, one will have different behavior depending on the chosen level density scheme.

To understand the convergence of this method it is helpful to study the plot of the product of level density and Boltzmann factor in figure 3.21: Here the empirical back shifted fermi gas density is 1-2 orders of magnitude greater. Thus, in order to capture the full rate at 3×10^{10} K for the empirical level density, I needed to obtain semi-converged excited states up to at least 80 MeV. Figure 3.22 shows a typical graph for the convergence of this method assuming one has gone high enough in excitation energy.

It becomes obvious from performing these calculations that using the shell model level density is more practical, in that it does not grow as quickly, but one may also prefer it from a
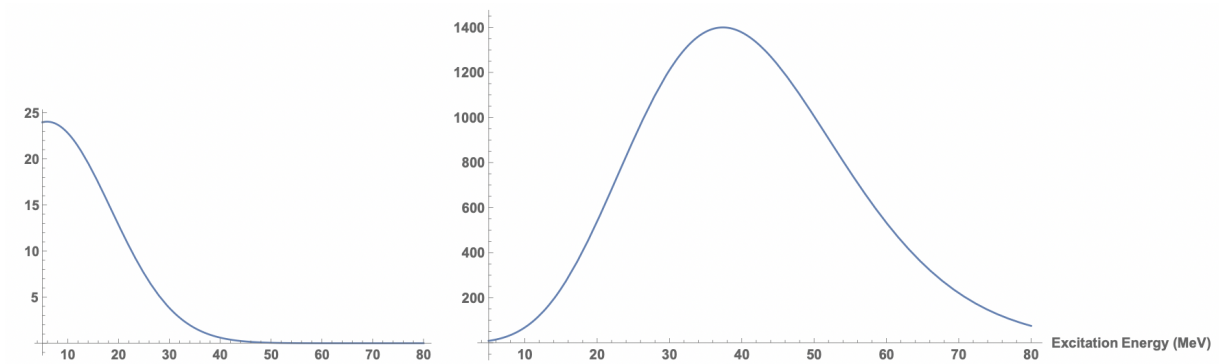
Figure 3.21: Product of Boltzmann factor and the level density from 0-80 MeV. The left graph is using the gaussian shell model level density, and right graph is the empirical back-shifted Fermi gas level density. Peaks represent the most probable energy.
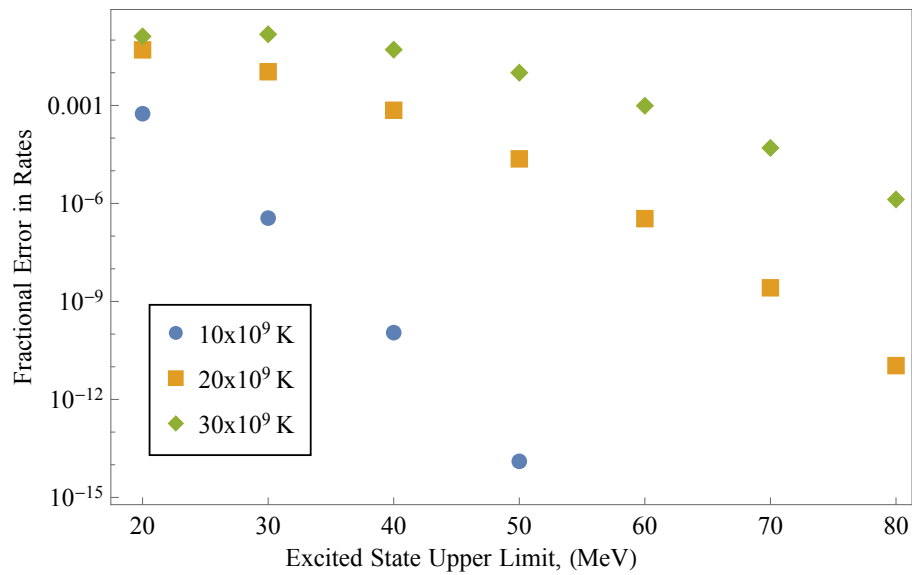
Figure 3.22: Fractional error in thermal Gamow-Teller transition rate when adding excited states in increments of 10 MeV for three different temperature points, and $Log[\rho y_e] = 1$

consistency point of view. Using the experimental level density, I am including states that don't exist in the theoretical shell model for nuclear structure and are not connected to the Gamow-Teller transition operator. The primary limitation of the shell model is that at some energy scale the level density hits an inflection point, drops off, and becomes unrealistic. But in principle before particle separation, or disassociation, the level density should approach a continuum. A larger model space could include the higher energy $g_{9/2}$ shell, which due to the spin-orbit coupling is nearby in energy to the pf-shell [5]. Consequently, this addition would also create more channels for GT strength. For the Gaussian shell model level density, we can take the difference of the energy centroid, μ and standard deviation σ mentioned above, which means the inflection point is around 135 MeV. It would be a valid question as to whether the semi-converged states in the region around this downward inflection point are legitimate representations of highly excited states. While for this nuclide (^{57}Co), I am not at all limited in going higher than 80 MeV in parent excitation energy, a larger shell model space may be required to provide realistic results for transition rates at temperatures nearest to 10^{11} K or above.

3.6 Discussion

In this chapter, I showed that Gamow-Teller strength distributions follow a Local Brink-Axel Statement more restrictive than the generalized Brink-Axel hypothesis. The LBAS shows that transition strength distributions becomes more similar locally as one goes higher in excitation energy for parent nuclei, where in many cases this held within an energy window of 1.3 MeV. After this one would not expect similarity due to the secular evolution of the total sum of strength [19]. This holds even for parent excited states that are semi-converged linear combinations of eigenstates (up to 80 MeV excitation in this work). Thus, this implies that one can still obtain strength distribution information at higher energies that would be prohibitive otherwise when requiring convergence of eigenstates. Further, I provided evidence that in some cases finer energy

windows for semi-converged parent states could be used that improve the similarity of strength functions. Specifically figures 3.5, 3.6, and 3.8, where windows of 0.3 MeV or 0.5 MeV for parent excitation energy, show smaller variance in average running sum of strength functions, when compared to average running sums for windows nearer to 1 MeV.

As the application, my rates for ^{57}Co $\rightarrow$ ^{57}Fe Gamow-Teller transitions computed using semi-converged excited states up to 80 MeV tend to be higher than the rates of Langanke and Martinez-Pinedo (LMP) [73], but lower than FFN rates in the computed regions. The differences cannot be explained by an overall quenching factor, which would raise all rates by the same amount in all density and temperature regions where FFN does not include such a factor. For electron capture, I found that the rates computed in this work are higher than LMP for temperatures above 10^9 K and densities greater than or equal to 10^5 g/cm^3 up to an order of magnitude. For positron decay, the rates are different from LMP by 1-2 orders of magnitude, except for a lull in temperatures between 10^9 K and 10^{10} K where they mostly match. Also for positron decay, above the temperature 10^{10} K, there is an uptick where my rates trend towards the higher FFN rates above the LMP rates by up to 2 orders of magnitude, especially when using the back-shifted Fermi Gas level density. Positron decay rates tend to match each other at all stellar densities and are primarily a function of temperature. My rates were in general higher than the LMP rates, which as they noted in their work could have significant implications for neutrino production, core temperature and entropy [73].

After obtaining strength functions for ^{57}Co up to 80 MeV, I was able to converge Gamow-Teller transition rates up to 7.5×10^{10} K for the Gaussian level density model, but only up to 3×10^{10} K for the empirical level density. This directly due to the fact that the empirical back-shifted Fermi gas level density continues to grow exponentially as energy increases, whereas the Gaussian-type shell model level density accelerates, then decelerates and inflects. For most temperatures and densities in both electron capture and positron decay, the empirical Fermi gas model rates tracked the Gaussian model rates in transition rates until temperatures near 10^{10} K

and beyond, which is due to the lack of excited state contributions. Notably, at high temperatures the Fermi gas level density rates diverge towards the FFN rates though this might be expected as FFN also uses an independent particle model.

While using the empirical level density may provide an upper limit on the rates, for a few reasons, as explained above, this may not be either practical or consistent. Nevertheless, my rates are computed up to temperatures and densities that are significant for massive stellar evolution up to collapse. The results of a broader sweep of Gamow-Teller rates in pf-shell nuclei remains to be completed and analyzed. However, I have shown that for certain iron peak nuclei of the pf-shell, a Local Brink Axel Statement holds. Based on this, I applied a new method that can compute transition rates at temperatures above 10^{10} K using up to arbitrary excitation energy in the parent state spectrum, which bodes well for updated stellar evolution calculations.

3.7   Acknowledgements

Chapter 3 is coauthored with Johnson, Calvin W. and Fuller, George M. I was the primary investigator and author of this chapter.

Chapter 4

Conclusion

In this dissertation, I presented two different applications of the Lanczos spectral decomposition method, that is, *symmetry group decompositions* and *transition strength functions* in Chapters 2 and 3, respectively. The methods used to produce each type of distribution are quite similar between each case, and were described in Chapter 1. But there is another strong relationship between the two works, namely Wigner's SU(4) symmetry [66] [67].

As discussed in Chapter 2, a Hamiltonian respecting a specific symmetry will have eigenstates corresponding to one single eigenvalue of the Casimir invariant operator of the symmetry group. When a dynamical symmetry is explicitly broken in the Hamiltonian, the eigenstates of the Hamiltonian were fragmented across the eigenvalues of the Casimir operator of the symmetry group. The Casimir invariant of SU(4) was applied to chromium nuclei, members of the pf shell, to show a quasi-dynamical symmetry pattern. I showed that even though Hamiltonian eigenstates in chromium isotopes were fragmented in SU(4), there were patterns that persisted in progressions of states known as rotational bands, which is called quasi-dynamical symmetry. As one progresses up the yrast band of lowest energy states of total angular momentum J, this corresponded to increased energy and orbital angular momentum L, as expected for a nucleus that is rotating faster. However, the spectral distributions for states of the yrast line in the Casimirs of

SU(4) and spin angular momentum, S^2, were relatively stable until band crossing. Then, from a second band that took over the yrast another pattern of quasi-dynamical symmetry emerged, which was also stable. Only a small, coherent evolution in SU(4) and spin was seen in either band for these nuclei.

This SU(4) quasi-dynamical symmetry has quantitative implications to the Gamow-Teller strength computed in Chapter 3. A Hamiltonian exactly respecting the SU(4) symmetry would commute not just with the Fermi operator, but also the GT operator, which is a generator of SU(4). In the case, eigenstates of the nuclear Hamiltonian would be simultaneous eigenstates of both the Fermi operator and GT operator up to isospin rotation. All of the GT strength would therefore be highly concentrated at a certain point in the energy spectrum, as in Fermi transitions and the isobaric analogue, where the total Gamow-Teller strength follows the Ikeda sum rule, $3(N-Z)$ [79]. The sum rule was another useful way to check calculations. However, the Ikeda sum rule is only exhausted when adding GT transitions in both directions, that is, where a proton is changed to a neutron ($p \rightarrow n$) or vice versa ($n \rightarrow p$). Uni-directional sum rules can also be computed [80]. Also of note, the sum rule for Fermi transitions is exactly equal to $N-Z$.

In Chapter 3, I showed that for selected iron peak nuclei, even though there is fragmentation, the strength functions are collected around certain resonances. Further, these collected response functions, a.k.a. strength functions, evolve in a smooth, secular manner as one increases parent excitation energy, which in nuclei generally involves increasing average angular momentum, J, [19] and increasing isospin T. The generalized Brink-Axel Hypothesis was modified to become a Local Brink Axel Statement about local similarity and secular evolution of strength functions. This was applied to the calculation of Gamow-Teller rates in astrophysical conditions relevant to massive stellar cores.

While it appears that the Local Brink-Axel statement and quasi-dynamical symmetries are aspects of the same phenomenon, where spectral distributions evolve smoothly as a certain input changes. To what extent this is quantitatively and directly connected is not always

completely clear. One would want to check whether the results were independent of basis and phenomenological interaction. But understanding the origin and mechanism of quasi-dynamical symmetry, specifically here in SU(4) symmetry breaking, would be a useful part of such an analysis. For example, this was explained in terms of embedded representations and adiabatic mixing of irreducible representations of broken symmetries in both Elliot's nuclear SU(3) model and a "soft" rotor system [81].

As the Gamow-Teller operator effects both spin and isospin, it is necessary to understand the evolution of GT transition strength functions in isospin, T, as well. In a more precise use of this method, one could include the minor angular momentum dependence of the Gamow-Teller transition matrix element, as shown above, and the spin-cutoff factor. But it is more likely that isospin would be a larger factor, as shown in Misch, Fuller and Brown [18] for sd-shell nuclei. To fully test the applicability of this method, I would also want to look for patterns or breakdowns in multiple cases of different types of parent nuclei, whether even-even, odd-odd, or even-odd. One would also want to look at neutron rich nuclei versus otherwise due to the dependence of the total weak transition strength on the difference $(N - Z)$ as above. And of course nuclei differ in Q-value and beta stability.

Besides specific properties of nuclei, or nuclear models, the uncertainties in this LBAS method arise from the difference between using a semi-converged representative state over an energy bin versus using fully converged states, and also potentially on the size of the bin. However, the nuclear level density is necessary to count states within the bin. Thus, I showed how assumptions about level density could affect the final rates, where at high temperatures this will become highly dependent on the type of nuclear model one is using. Specifically, I compared the shell model level density and the back-shifted Fermi gas level density.

Ideally though, a full update of weak transitions for pf-shell nuclei would now follow. For $A \geq 65$, computations of weak interaction rates have avoided a full scale shell model approach, but have been computed using various methods, including the FFN method [82], the random

phase approximation (RPA) and Shell Model Monte Carlo [83]. It remains to be seen whether the LBAS method developed here could accurately tackle larger model spaces such as the fpg shell, which is the pf-shell plus $g_{9/2}$, as the single particle states would increase by 50 percent, or 10 states. This combinatorially leads to a massive increase in basis dimension for nuclides in the middle of this combined model space.

Nevertheless, it is clear from my work that the inclusion of more excited states can have consequences on stellar weak interaction rates not previously seen in other work. However, another direction worthy of exploration is the computation of spectral distribution of thermal operators. Would it be possible with an iterative algorithm to directly and efficiently compute thermal rates? This could remove the need to compute the initial excited states in the first place. An algorithm involving a Boltzmann factor runs into the problem of how to properly treat exponential functions of matrix operators, such as the Hamiltonian. There are standard approaches [1]. For example, one could directly compute it from the definition of the matrix exponential as a power series, or perhaps use the eigenspectrum, or instead focusing on the result of the exponential operator acting on a vector. A common approach is scaling and squaring using special functions known as Pade approximants.

Relatedly, finite temperature Lanczos algorithms have been developed in solid state systems [84], which depend on thermal averaging of many separate Lanczos runs and in this case would be doubled as one would need the eigenspectrum of the parent and the daughter. One could apply a massively parallel block Lanczos algorithms [1] to speed up this process. A good starting point is to transform the system via a Laplace or Fourier transform, where one no longer has to deal with the Dirac delta functions in the strength function definition of equation 1.33, as is done in the Shell Model Monte Carlo method [85]. This Monte Carlo approach was used for GT transitions and electron capture by Radha et al. [86] and Dean et al. [87], respectively. Of course any method that would reduce the uncertainty in the nuclear physics relevant to stellar evolution would be welcome. I look forward to contributing to progress on these fronts.

Bibliography

[1] G. H. Golub and C. F. V. Loan, *Matrix Computations, 4th Edition* (The Johns Hopkins University Press, 2013).

[2] A. deShalit and H. Feshbach, *Theoretical Nuclear Physics, Vol. 1: Nuclear Structure* (John Wiley and Sons, Inc., 1974).

[3] M. G. Mayer, Physical Review **74**, 235 (1948).

[4] O. Haxel, J. H. D. Jensen, and H. E. Suess, Phys. Rev. **75**, 1766 (1949).

[5] M. G. Mayer, Phys. Rev. **78**, 16 (1950).

[6] R. Machleidt, K. Holinde, and C. Elster, Physics Reports **149**, 1 (1987).

[7] C. W. Johnson, W. E. Ormand, and P. G. Krastev, Computer Physics Communications **184**, 2761 (2013).

[8] B. A. Brown and W. A. Richter, Phys. Rev. C **74**, 034315 (2006).

[9] M. Honma, T. Otsuka, B. Brown, and T. Mizusaki, Eur. Phys. J. A **25**, 499 (2005).

[10] M. Hjorth-Jensen, T. T. Kuo, and E. Osnes, Physics reports **261**, 125 (1995).

[11] A. R. Edmonds, *Angular momentum in quantum mechanics* (Princeton University Press, 1996).

[12] S. E. Woosley and A. Heger, Reviews of Modern Physics **74**, 1015 (2002).

[13] H. A. Bethe, G. E. Brown, J. Applegate, and J. M. Lattimer, Nuclear Physics A **324**, 487 (1979).

[14] E. M. Burbidge, G. R. Burbidge, W. A. Fowler, and F. Hoyle, Reviews of Modern Physics **29**, 547 (1957).

[15] C. W. Johnson, W. E. Ormand, K. S. McElvain, and H. Shan, "Bigstick: A flexible configuration-interaction shell-model code," arXiv:1801.08432v1 [physics.comp-ph] .

[16] P. Maris, H. M. Aktulga, M. A. Caprio, U. V. Catalyurek, E. G. Ng, D. Oryspayev, H. Potter1, E. Saule, M. Sosonkina, J. P. Vary, C. Yang, and Z. Zhou, in *Journal of Physics: Conference Series*, Vol. 403 (IOP Publishing, 2012) p. 012019.

[17] G. M. Fuller, W. A. Fowler, and M. J. Newman, The Astrophysical Journal Supplemental Series **48**, 279 (1982).

[18] G. W. Misch, G. M. Fuller, and B. A. Brown, Phys. Rev. C **90**, 065808 (2014).

[19] C. W. Johnson, Physics Letters B **750**, 72 (2015).

[20] W. C. Haxton, K. M. Nollett, and K. M. Zurek, Phys. Rev. C **72**, 065501 (2005).

[21] P. Ring and P. Schuck, *The nuclear many-body problem* (Springer Science & Business Media, 2004).

[22] E. M. Szanto, A. S. de Toledo, H. V. Klapdor, M. Diebel, J. Fleckner, and U. Mosel, Phys. Rev. Lett. **42**, 622 (1979).

[23] W. Spreng, F. Azgui, H. Emling, E. Grosse, R. Kulessa, C. Michel, D. Schwalm, R. S. Simon, H. J. Wollersheim, M. Mutterer, J. P. Theobald, M. S. Moore, N. Trautmann, J. L. Egido, and P. Ring, Phys. Rev. Lett. **51**, 1522 (1983).

[24] T. Tanaka, K. Iwasawa, and F. Sakata, Phys. Rev. C **58**, 2765 (1998).

[25] R. Bengtsson, I. Hamamoto, and B. Mottelson, Physics Letters B **73**, 259 (1978).

[26] R. A. Sorensen, Nuclear Physics A **269**, 301 (1976).

[27] S. Ćwiok, J. Dudek, and Z. Szynański, Physics Letters B **76**, 263 (1978).

[28] K. Sugawara-Tanabe and K. Tanabe, Physics Letters B **207**, 243 (1988).

[29] S. Ćwiok, W. Nazarewicz, J. Dudek, and Z. Szymański, Phys. Rev. C **21**, 448 (1980).

[30] V. Velazquez, J. Hirsch, Y. Sun, and M. Guidry, Nuclear Physics A **653**, 355 (1999).

[31] J. A. Cameron, M. A. Bentley, A. M. Bruce, R. A. Cunningham, W. Gelletly, H. G. Price, J. Simpson, D. D. Warner, and A. N. James, Phys. Rev. C **49**, 1347 (1994).

[32] J. Cameron, J. Jonkman, C. Svensson, M. Gupta, G. Hackman, D. Hyde, S. Mullins, J. Rodriguez, J. Waddington, A. Galindo-Uribarri, H. Andrews, G. Ball, V. Janzen, D. Radford, D. Ward, T. Drake, M. Cromaz, J. DeGraaf, and G. Zwartz, Physics Letters B **387**, 266 (1996).

[33] C. D. O'Leary, M. A. Bentley, D. E. Appelbe, D. M. Cullen, S. Ertürk, R. A. Bark, A. Maj, and T. Saitoh, Phys. Rev. Lett. **79**, 4349 (1997).

[34] J. A. Cameron, J. L. Rodriguez, J. Jonkman, G. Hackman, S. M. Mullins, C. E. Svensson, J. C. Waddington, L. Yao, T. E. Drake, M. Cromaz, J. H. DeGraaf, G. Zwartz, H. R. Andrews, G. Ball, A. Galindo-Uribarri, V. P. Janzen, D. C. Radford, and D. Ward, Phys. Rev. C **58**, 808 (1998).

[35] S. M. Lenzi, C. A. Ur, D. R. Napoli, M. A. Nagarajan, D. Bazzacco, D. M. Brink, M. A. Cardona, G. de Angelis, M. De Poli, A. Gadea, D. Hojman, S. Lunardi, N. H. Medina, and C. R. Alvarez, Phys. Rev. C **56**, 1313 (1997).

[36] F. Brandolini, J. Sanchez-Solano, S. M. Lenzi, N. H. Medina, A. Poves, C. A. Ur, D. Bazza-cco, G. De Angelis, M. De Poli, E. Farnea, A. Gadea, D. R. Napoli, and C. Rossi-Alvarez, Phys. Rev. C **66**, 021302 (2002).

[37] K. Hara, Y. Sun, and T. Mizusaki, Phys. Rev. Lett. **83**, 1922 (1999).

[38] V. Velázquez, J. G. Hirsch, and Y. Sun, Nuclear Physics A **686**, 129 (2001).

[39] E. Caurier, J. L. Egido, G. Martínez-Pinedo, A. Poves, J. Retamosa, L. M. Robledo, and A. P. Zuker, Phys. Rev. Lett. **75**, 2466 (1995).

[40] E. Caurier, A. P. Zuker, A. Poves, and G. Martínez-Pinedo, Phys. Rev. C **50**, 225 (1994).

[41] L. Zamick, M. Fayache, and D. C. Zheng, Phys. Rev. C **53**, 188 (1996).

[42] G. Martínez-Pinedo, A. Poves, L. M. Robledo, E. Caurier, F. Nowacki, J. Retamosa, and A. Zuker, Phys. Rev. C **54**, R2150 (1996).

[43] G. Martínez-Pinedo, A. P. Zuker, A. Poves, and E. Caurier, Phys. Rev. C **55**, 187 (1997).

[44] Z.-C. Gao, M. Horoi, Y. S. Chen, Y. J. Chen, and Tuya, Phys. Rev. C **83**, 057303 (2011).

[45] F. Brandolini and C. A. Ur, Phys. Rev. C **71**, 054316 (2005).

[46] A. Juodagalvis, I. Ragnarsson, and S. Åberg, Phys. Rev. C **73**, 044327 (2006).

[47] J.-Q. Chen, J. Ping, and F. Wang, *Group representation theory for physicists*, Vol. 7 (World Scientific, 1989).

[48] I. Talmi, *Simple models of complex nuclei* (CRC Press, 1993).

[49] D. J. Rowe and J. L. Wood, *Fundamentals of nuclear models: Foundational models* (World Scientific, 2010).

[50] P. Brussard and P. Glaudemans, *Shell-model applications in nuclear spectroscopy* (North-Holland Publishing Company, Amsterdam, 1977).

[51] B. A. Brown and B. H. Wildenthal, Annual Review of Nuclear and Particle Science **38**, 29 (1988).

[52] E. Caurier, G. Martinez-Pinedo, F. Nowacki, A. Poves, and A. P. Zuker, Reviews of Modern Physics **77**, 427 (2005).

[53] M. Honma, T. Otsuka, B. A. Brown, and T. Mizusaki, Phys. Rev. C **65**, 061301 (2002).

[54] A. Poves, J. Sánchez-Solano, E. Caurier, and F. Nowacki, Nuclear Physics A **694**, 157 (2001).

[55] J. Elliott, in *Proceedings of the Royal Society of London A: Mathematical, Physical and Engineering Sciences*, Vol. 245 (The Royal Society, 1958) pp. 128–145.

[56] M. Harvey, in *Advances in nuclear physics* (Springer, 1968) pp. 67–182.

[57] P. Rochford and D. Rowe, Physics Letters B **210**, 5 (1988).

[58] J. Escher, C. Bahri, D. Troltenier, and J. Draayer, Nuclear Physics A **633**, 662 (1998).

[59] V. G. Gueorguiev, J. P. Draayer, and C. W. Johnson, Phys. Rev. C **63**, 014318 (2000).

[60] C. Bahri, J. Escher, and J. Draayer, Nuclear Physics A **592**, 171 (1995).

[61] C. Bahri, D. J. Rowe, and W. Wijesundera, Phys. Rev. C **58**, 1539 (1998).

[62] D. J. Rowe, in *The Nucleus* (Springer, 2000) pp. 379–395.

[63] C. Bahri and D. Rowe, Nuclear Physics A **662**, 125 (2000).

[64] C. W. Johnson, Phys. Rev. C **91**, 034313 (2015).

[65] O. Castaños, J. P. Draayer, and Y. Leschber, Z. Phys. A **329**, 33 (1988).

[66] E. Wigner, Phys. Rev. **51**, 106 (1937).

[67] K. Hecht and S. C. Pang, Journal of Mathematical Physics **10**, 1571 (1969).

[68] P. Vogel and W. E. Ormand, Phys. Rev. C **47**, 623 (1993).

[69] A. Poves and G. Martinez-Pinedo, Physics Letters B **430**, 203 (1998).

[70] C. W. Johnson, I. Stetcu, and J. P. Draayer, Phys. Rev. C **66**, 034312 (2002).

[71] T. Dytrych, K. D. Launey, J. P. Draayer, P. Maris, J. P. Vary, E. Saule, U. Catalyurek, M. Sosonkina, D. Langr, and M. A. Caprio, Phys. Rev. Lett. **111**, 252501 (2013).

[72] T. Oda, M. Hino, K. Muto, and M. Takahara, Atomic Data and Nuclear Data Tables **56**, 231 (1994).

[73] K. Langanke and G. Martinez-Pinedo, Nuclear Physics A **673**, 481 (2000).

[74] E. Caurier, K. Langanke, and G. Martinez-Pinedo, Nuclear Physics A **653**, 439 (1999).

[75] A. Poves and A. Zuker, Physics Reports **70**, 235 (1981).

[76] K. M. Patton, C. Lunardini, R. J. Farmer, and F. X. Timmes, The Astrophysical Journal **851**, 1 (2017).

[77] V. Mishra, N. Boukharouba, C. E. Brient, S. M. Grimes, and R. S. Pedroni, Physical Review C **49**, 750 (1994).

[78] W. M. Spinella and C. W. Johnson, Physical Review C **90**, 014315 (2014).

[79] K. Ikeda, S. Fujii, and J. I. Fujita, Physics Letters **3**, 271 (1963).

[80] Y. Lu and C. W. Johnson, Physical Review C **97**, 034330 (2018).

[81] D. J. Rowe, P. Rochford, and J. Repka, Journal of Mathematical Physics **29**, 572 (1988).

[82] J. Pruet and G. M. Fuller, The Astrophysical Journal Supplemental Series **149**, 189 (2003).

[83] K. Langanke and G. Martinez-Pinedo, Reviews of Modern Physics **75**, 819 (2003).

[84] J. Jaklic and P. Prelovsek, Physical Review B **49**, 5065 (1994).

[85] G. H. Lang, C. W. Johnson, S. E. Koonin, and W. E. Ormand, Phys. Rev. C **48**, 1518 (1993).

[86] P. B. Radha, D. J. Dean, S. E. Koonin, K. Langanke, and P. Vogel, Physical Review C **56**, 3079 (1997).

[87] D. J. Dean, K. Langanke, L. Chatterjee, P. B. Radha, and M. R. Strayer, Physical Review C **58**, 536 (1998).